Polymer properties measured by micromechanical cantilever technique

DISSERTATION

zur Erlangung des Grades

"Doktor der Naturwissenschaften"

am Fachbereich Chemie, Pharmazie und Geowissenschaften

der Johannes Gutenberg-Universität Mainz

vorgelegt von

Master-Chem. **Renhua Zhang**

Mainz，August 2007

Abstract

Surface stress changes induced by specific adsorption of molecules were investigated using a micromechanical cantilever sensor (MCS) device. 16 MCS are grouped within four separate wells. Each well can be addressed independently by different liquid enabling functionalization of MCS separately by flowing different solutions through each well and performing sensing and reference experiments simultaneously. In addition, each well contains a fixed reference mirror, which allows measuring the absolute bending of MCS. The effect of the flow rate on the MCS bending change was found to be dependent on the absolute bending value of MCS. In addition, the signal from the reference mirror can be used to follow refractive index changes upon mixing different solutions. Finite element simulation of solution exchange in wells was compared with experiment results. Both revealed that one solution can be exchanged by another one after a total volume of 200 μl has flown through. Using MCS, the adsorption of thiolated deoxyribonucleic acid (DNA) molecules and 6-mercapto-1-hexanol (MCH) on gold surfaces, and the DNA hybridization were performed. The nanomechanical response is in agreement with data reported by Fritz et al.[1] Thus, the multiwell device is readily applicable for sensing of multiple chemical and biological recognition events in a single step.

In this context controlled release and uptake of drugs are currently widely discussed. As a model system, we have used polystyrene (PS) spheres with diameters in the order of μm. The swelling behavior of individual PS spheres in toluene vapor was studied via mass loading by means of micromechanical cantilever sensors. For 4–8% cross-linked PS a mass increase of 180% in saturated toluene vapor was measured. In addition, the diameter change in saturated toluene vapor was measured and the corresponding volume increase of 200% was calculated. The mass of the swollen PS sphere decreases with increasing exposure time to ultraviolet (UV) light. The swelling response is significantly different between the first and the second exposure to toluene vapor. This is attributed to the formation of a cross-linked shell at the surface of the PS spheres. Shape persistent parts were observed for locally UV irradiated PS spheres. These PS spheres were found

to be fluorescent and cracks occur after exposure in toluene liquid. The diffusion time of dye molecules in PS spheres increases with increasing chemical cross-linking density. This concept of locally dissolving non cross-linked PS from the sphere was applied to fabricate donut structures on surfaces.

Arrays of PS spheres were fabricated using spin coating. The donut structure was produced simply after liquid solvent rinsing. The complete cross-linking of PS spheres was found after long exposure time to UV. We found that stabilizers play a major role in the formation of the donut nanostructures.

Index

Chapter 1

Introduction

Biotechnology has gained an increasing interest in recent years. It is a technology based on biological elements (tissues, cells, proteins, enzymes, antibodies, nucleic acids, etc) to make products or processes used in agriculture, food science and medicine. In particular, the application in drug production and gene testing is in great demand during last decade. To monitor or detect the biological elements and the interactions among these elements, sensing devices are required. Such sensing devices[2-4] are widely used in environment[5,6] to detect toxic substances in air or water; in food industry[7-10] to detect chemical and microbiological contaminant; and particularly, in the pharmaceutical and health care industry[11-13] to monitor drug or living cells and to study the interaction between a drug compound and a biocomponent.

There are several requirements for sensors: potable, miniature, high selectivity and high sensitivity. The commonly used sensors includes: Surface Plasma Resonance (SPR), Quartz Crystal Microbalances (QCM),[14] Surface Acoustic Wave devices (SAW),[15] etc. The sensor element can be operated in either liquid or gas environment.

Micromechanical Cantilever Sensor (MCS) is a new class of extremely sensitive sensor devices currently developed for chemical and biological detection.[1,16-22] There are several advantages of MCS over other sensing mechanisms: label free detection of molecules, high sensitivity and high reproducibility,[23] and massive parallel measurements.[24] In conventional sorption experiments, the mass change can be determined by balances with a mass sensitivity of **µg**. Apparatuses with a higher mass sensitivity like QCM and SAW show a mass sensitivity of **ng**.[14,15] But their active sensor area of **cm^2** is large.[25] While the mass sensitivity of MCS is in the order of picograms (**pg**).[26-28] MCS's active sensor area of **µm^2** facilitates the fabrication into multi-element sensor array, which is capable of massive parallel measurements.

MCS can be operated at different modes to detect molecules via mass changes or surface stress changes.[21,29-31] The two basic modes are usually referred to: Dynamic frequency mode and static bending mode.

In the **dynamic frequency** mode, MCS transduce recognition events on their receptor-coated surfaces into frequency shifts. In this way, Thundat et al. detected water[27] using cantilever coated with a thin gelatin film and Pinnaduwage et al. detected explosive vapor[32] using piezoresistive cantilever deposited with trinitrotoluene (TNT). In both work, single MCS was used as platform and a mass resolution of picogram was achieved. In my work, a piezoelectric transducer underneath the cantilever is operated at approximately the resonant frequency of the cantilever to excite vibrations. Upon attachment of the particle at the free end of the cantilever, the mass of the cantilever with attached particle changes, resulting in a shift of its resonant frequency ($f_0 \rightarrow f_1$) [Fig. 1]. In addition, the mass of the cantilever with attached particle changes owing to the absorption of the solvent in the particle, resulting in an additional shift of its resonant frequency ($f_1 \rightarrow f_2$).

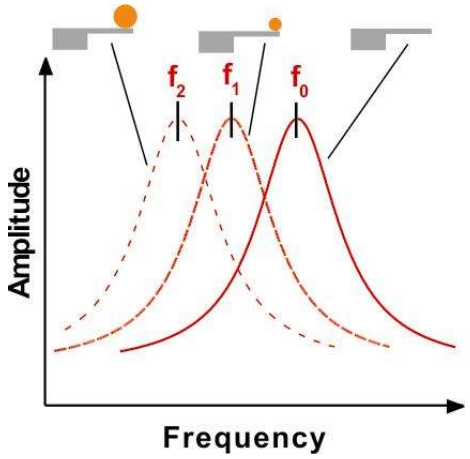

Fig. 1. Schematic drawing of dynamic mode measurement. The resonance frequency of a bare cantilever, the cantilever with attached sphere, and the cantilever with swollen particle is f_0, f_1, and f_2, respectively.

In the **static bending** mode, MCS transduce recognition events on their receptor-coated surfaces into nanomechanical deflections. Interactions among a wide range of substances, including polymers, antibodies, proteins, cells and drugs, can be studied via this mode. In this way, Fritz et al. performed hybridization of complementary

oligonucleotides using two cantilevers in an array and showed that a single base mismatch is detectable.[1] In this mode, the gravitational force induced by molecular loading is negligible. Thus, what is the origin of the MCS deflection? One origin could be a **bimetallic effect**: Here thermally induced stresses are typical for metal-coated cantilevers for which the base material (e.g., silicon, silicon dioxide, or silicon nitride) and the metal coating (e.g., gold) have different coefficients of thermal expansion. Therefore, a temperature change induces unequal expansion of the layers in a bi-material cantilever and causes concomitant bending [Fig. 2a]. The temperature sensitivity of 10^{-5} K and heat sensitivity of attojoule can be achieved in this mode.[16]

Molecular adsorption is another process which leads to the deflection of the cantilever. The deflection is attributed to the attractive force or repulsion force between the adsorbed molecules. The surface stress change of the layer which expands is defined as compressive surface stress change. The layer which contracts has a tensile surface stress change, correspondingly [Fig. 2b].

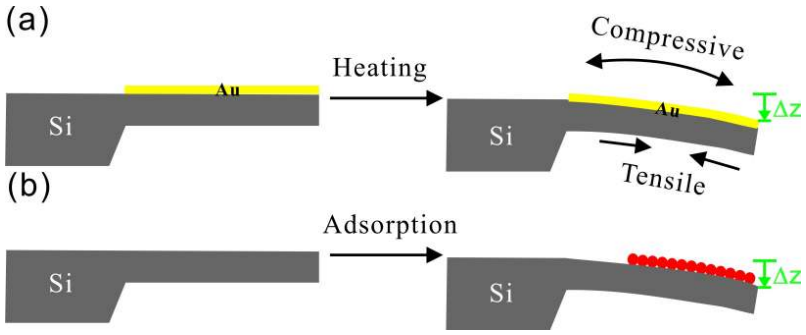

Fig. 2. Schematic drawing of static mode measurement. The cantilever bends down with a deflection $\Delta Z\downarrow$ upon (a) heating and (b) adsorption.

To transduce the recognition event into nanomechanical deflections, some MCS are coated with a layer sensitive to molecules in an analyte. These MCS are called sensing MCS. MCS deflection responses are sensitive to undesired artifacts such as thermal drift,[33,34] unspecific adsorption of molecules from the environment and slow electrochemical processes such as silicon hydration. Unspecific adsorption is induced by undesired molecules physically or chemically adsorbed on the MCS. It results in an

undesired response in frequency shift or deflection change. The undesired molecules may come from the reaction mixture (analyte solution and carrier solution, water or buffer is usually used as carrier solution to deliver the analyte molecules to the MCS) or ambient environment. It is therefore mandatory to have a **differential measurement configuration**, where the reference MCS, coated with a layer inert to the analyte of interest, compensates all interfering interactions and thermal drift. Additionally, the sensitivity may vary from one MCS to another because of variations in the physical (e.g. thickness of the MCS and the deposited layers) and biochemical (e.g. density of the bioreceptors immobilized) characteristics. These variations can arise in the fabrication and functionalization processes of MCS. Averaging the deflection response over several nominally identical MCS increase the reliability of measurements.[35] Therefore MCS arrays are fabricated and used for sensing. MCS arrays with two[36], four[37], and eight[38] rectangular cantilevers [Fig. 3] have been reported. It has been also shown that more than 1000 cantilevers can be operated to realize a nanomechanical storage device.[39]

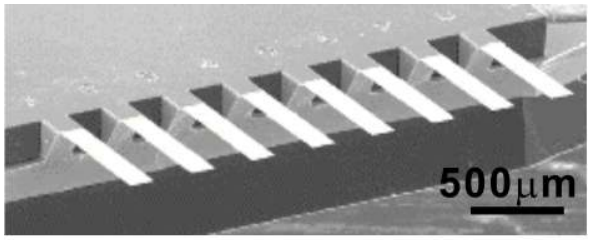

Fig. 3. Scanning electron microscope (SEM) micrograph of micromechanical cantilever sensor (MCS) array. There are eight cantilevers (white part in the graph) within one array, each of them is 500 microns long, 100 microns wide and less than 1 micron thick.[40]

Since micromechanical cantilevers are tiny, sensitive and fragile elements, special ways to functionalize individual surfaces have to be developed. In addition, for applying the static bending mode, selectively one side of the MCS must be coated with molecules. The functionalization processes and methods play a key role in the performance of MCS:

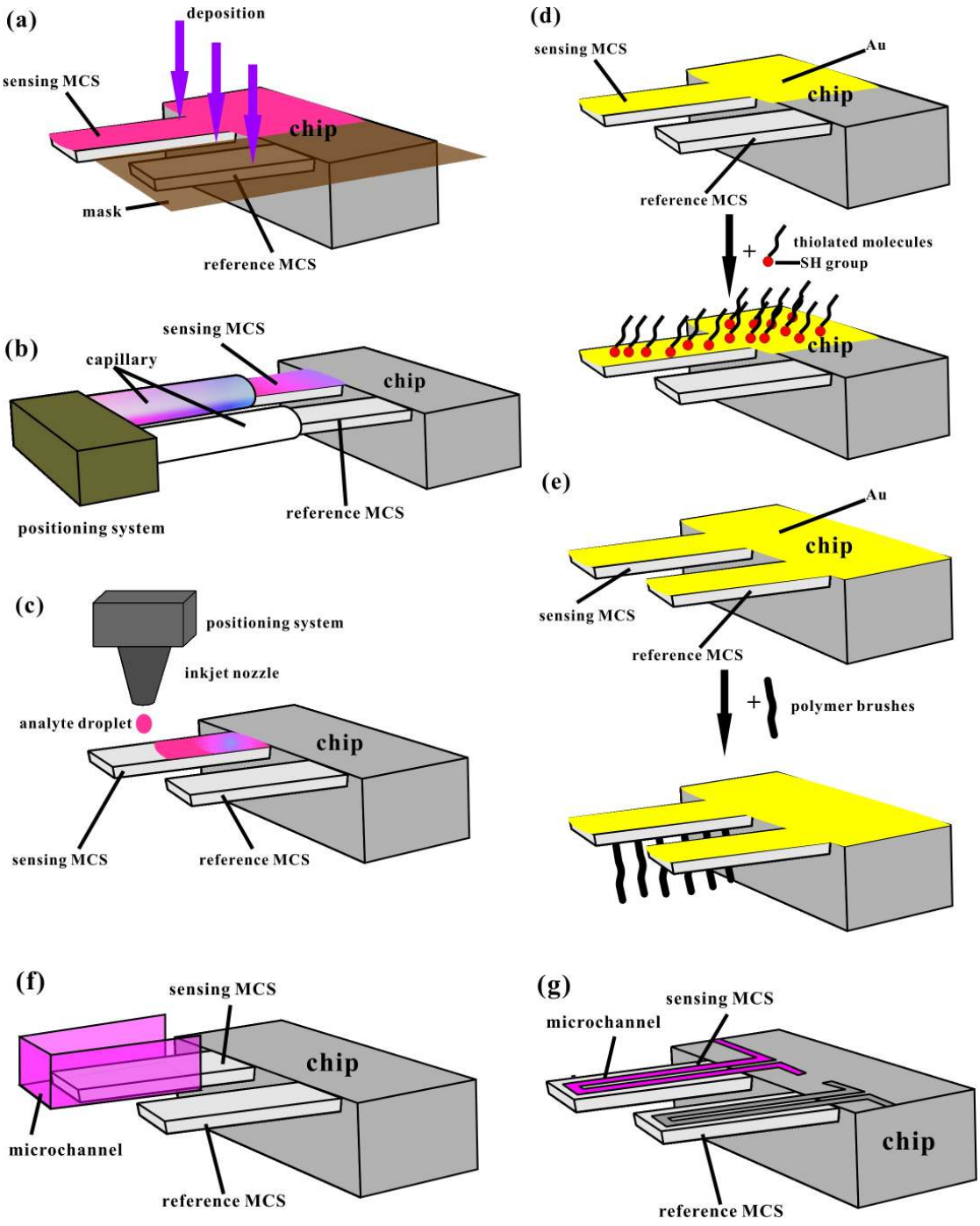

Fig. 4. Schematic drawing of different functionalization methods to differentiate reference and sensing MCS. (a) shadow masking (b) capillary (c) inkjet deposition (d) thiolated molecules immobilization (e) "grafting from" synthesis (f) external microchannel (g) etched microchannel on MCS.

The shadow masking method[41] [Fig. 4a] was used to functionalize part of the MCS array. The process is simple and metal coating, spray coating, plasma deposition can be achieved by this method. But it is tricky to perfectly shield the reference MCS by mask. The metal deposition has to be performed by metal evaporation in vacuum. The coating material is limited, liquid solutions such as DNA molecules in buffer are not feasible.

For the incubation into capillary arrays method[1] [Fig. 4b], individual MCS can be easily functionalized by incubation into individual capillary with corresponding coating solutions. But the concentration gradient in the capillary caused by the evaporation at the open aperture might result in the inhomogeneous coating layer along the MCS. Retraction of coated layer to capillary might happen when withdrawing the capillary. Since both sides of the MCS are immersed in the capillary, to achieve only one side functionalization, the other side of sensing MCS has to be inert to the coating layer.

For the inkjet deposition[42] method [Fig. 4c], the thickness of the coating layer can be controlled by adjusting the size and pitch of the droplet. Coating desired local positions is feasible simply by controlling the deposition sites using computer-driven positioning system. Individual functionalization on individual MCS can be easily achieved. But the coating layer on the MCS is inhomogeneous owing to the coffee stain effect.[43] A positioning system precisely controlled by computer is required.

Immobilization of thiolated molecules on gold coated cantilever through gold-sulfur bonding[44] is another mostly used method to functionalize the MCS surface [Fig. 4d]. The coating layer of immobilized molecules is homogeneous and robust. But the investigated molecules have to be terminated with thiol group to obtain the affinity with gold surface of the MCS. Owing to the presence of gold, the bimetallic effect is inevitable.

Bumbu et al. developed a novel technique which is based on “grafting-from” synthesis of polymer brushes[45] [Fig. 4e]. The coating layer is very stable in the analyte solutions. The density of the grafted molecules can be controlled. But this method is complicated and time consuming owing to the multi-step chemical reaction process.

Recently, The functionalization by immersing MCS into microchannels was reported by Berger et al. [Fig. 4f].[46] This method is easy, simple and a variety of materials can be used. But it has the same drawback as capillary method, which is difficult to achieve one side functionalization.

Microchannels were also developed on the MCS by Burg et al. [Fig. 4g].[47] No supplemental equipment is required in this method. But the etched microchannel on MCS requires specific fabrication technique to produce microchannel on MCS, which is costly. The density gradient of the coating layer along the MCS might occur.

Cross contamination could happen during above-mentioned functionalization methods (shadow masking, capillary, inkjet deposition, external microchannel). The coated layer on sensing MCS might flow through the chip body to the adjacent reference MCS during or after functionalization. During the following recognition events, cross contamination might happen on MCS functionalized by all seven above-mentioned methods. The molecule adsorbed on the sensing MCS might hop to the adjacent reference MCS due to environment exchange (liquid or gas flow) or disturbance. It would cause cross talk and interference in the response of neighboring MCS [Fig. 5].

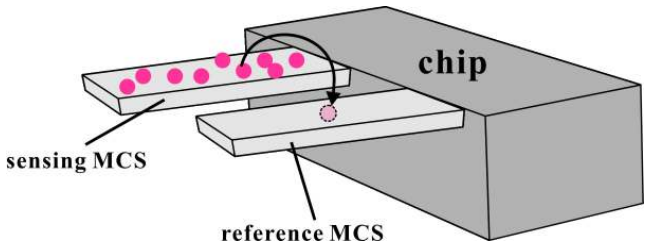

Fig. 5. Schematic drawing of cross contamination.

To improve the performance of the functionalization process and recognition events, a new MCS array layout was designed [Fig. 6]. By **dividing the MCS into separate wells**, an easy, independent and automated functionalization by fluidic flow is achieved. The risk of cross contaminations among different wells caused by molecules detaching from sensing MCS or reference coatings, diffusing to adjacent MCS is avoided anytime during the measurement.

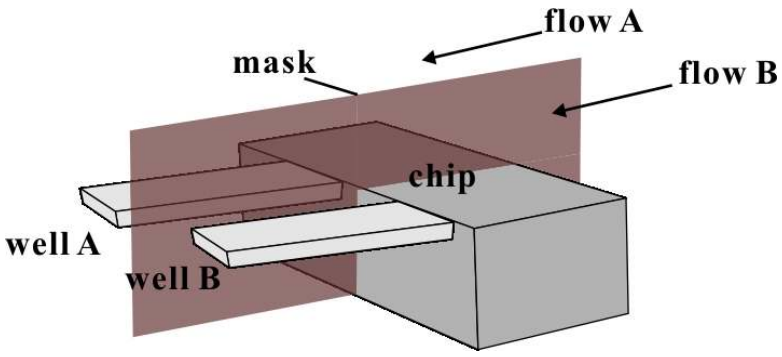

Fig. 6. A MCS array layout with two separate wells. The fluid flow is independent in each well by using a mask to prevent the mixing among different wells. The risk of cross contaminations among different wells is avoided.

The advantage of using separate wells and requirements for successful MCS measurements will be discussed in **chapter 2**. In particular the variations in mechanical properties from well to well, sample entry delay times, flow rate dependence, and mixing of solutions during sample injection are investigated. To outline an application, DNA hybridization measurements are performed.

Since most MCS measurements involve fluid flow, the effect of flow on the MCS deflection is different, depending on the curvature of MCS [Fig. 7]. Therefore the curvature and **absolute bending** (the value of ΔZ in Fig. 2, which is the deflection of the cantilever's free end relative to its straight position) of MCS is important to be addressed during the measurements.

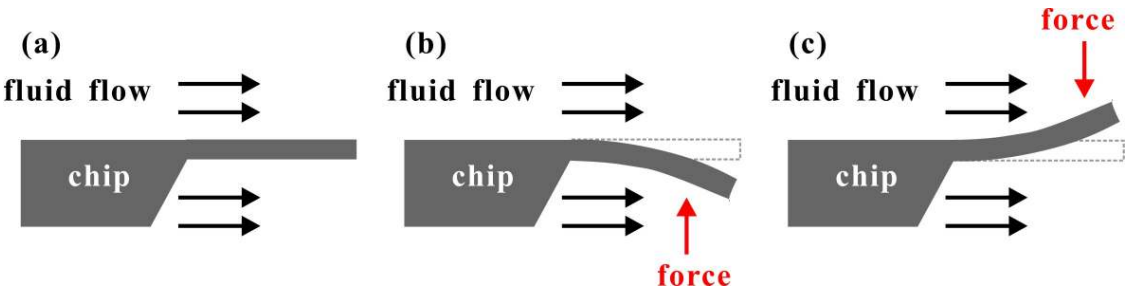

Fig. 7. The effect of fluid flow on the MCS. (a) No force is applied on the MCS when the MCS does not bend. (b) The force applied on the MCS is upward when the MCS bends down relative to its straight position as (a). (c) The force applied on the MCS is downward when the MCS bends up relative to its straight position as (a).

In order to measure the absolute bending of MCS, a **fixed reference mirror** is supplemented in each well. The presence of a reference mirror in each well allows measuring of the absolute MCS bending. In addition, the reference mirror can be used to monitor potential optical artifacts like refractive index changes due to the exchange of solutions in the wells. The calibration of optical readout of MCS systems and the study of flow rate dependence on MCS with different curvatures using reference mirror will be discussed in **chapter 2**.

As introduced in the beginning of this chapter, biotechnology has gained a great interest in the application in drug production. Lipid vesicles or liposomes were introduced as transport vesicles for drug since 1980s.[48,49] But their inherent instability and short lifetimes limit the applications in drug delivery. In the past few years polymer has been taken as a promising vesicle to transport drug due to their great stability and tunable properties.[50-53] Dendrimers, block copolymers, polyelectrolytes etc are commonly used as the transport system for drugs. Chen and Hoffman synthesized graft copolymers composed of temperature-sensitive poly-*N*-isopropyl acrylamide (PNIPAAm) side chains and pH-sensitive poly-acrylic acid (PAAc) backbones. These gels were able to respond to both temperature and pH changes. When the temperature increases at constant pH, PNIPAAm side chains precipitate, owing to the release of bound water. When the pH of the solution decreases at constant temperature, the PAAc backbone shrinks, which can be used for the release of encapsuled drug molecules.[54]

The mechanism and dynamics of encapsulation and release of drug in these systems are the key issue in the applications for therapy [Fig. 8]. Since the systems are used in human body, their material properties (enthalpy, volume, mass, interfacial tension, thermo-property, adhesion etc) are required to be characterized to achieve better performance.

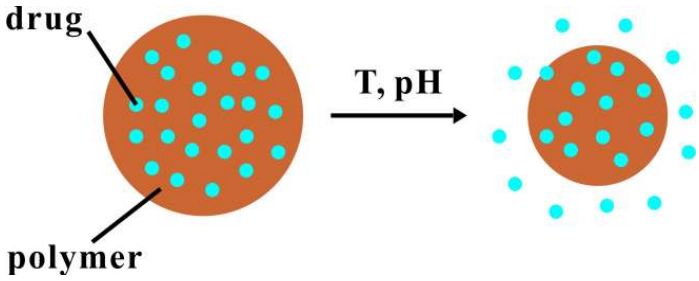

Fig. 8. Schematic illustration of drug release principle. The drug molecules inside the polymer particle are released upon stimuli such as change in temperature and PH in the environment.

In my work, I focused on solvent vapor annealing of micron-sized PS particles, which was used as a model system to study the uptake and release of solvent molecules in the polymer particle in detail [Fig. 9]. In particular, the mass uptake/loss of the polymer particles, the diffusion dynamics of the solvent molecules and the size dependence are investigated using MCS technique operated at **dynamic frequency mode**. The results will be discussed in **chapter 3**.

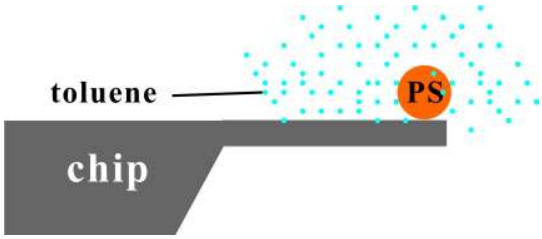

Fig. 9. Schematic illustration of toluene vapor annealing of micron-sized PS particles. The PS particle is attached on the free end of the MCS. The mass uptake/loss of the polymer particles can be studied using MCS operated at dynamic frequency mode.

Recently, irreversible annealing of locally UV light irradiated PS samples in a solvent vapor was used to fabricate microvessels [Fig. 10a].[55] The non cross-linked PS plate locally covered by mask was exposed to plasma or ultra violet (UV) light. The UV light irradiation under ambient conditions induces cross-linking and oxidation of the PS chains in the uncovered part.[56] Upon exposure to solvent, the non cross-linked PS swells and protrusions occur. Cross-linking and oxidation both alter the swelling properties of

the PS samples resulting in permanent microvessels after the solvent vapor annealing. Hence there must be a different swelling behavior of the PS before and after UV light irradiation.

The MCS technique allows to follow **swelling** of a selected PS particle. This particle can be exposed to UV light and characterized afterwards again. Hereby the **dynamics of solvent diffusion** and the **influence of cross-linking density** induced by chemical cross-linking agent or UV light can be studied. Furthermore fluorescence correlation spectroscopy (FCS) technique is performed to study the distribution of dye molecules inside the PS. All these results will be discussed in **chapter 3**.

During the UV irradiation on non-cross-linked PS particles, we found that the outer shell of a PS sphere was cross-linked. Based on this observation, a **nanosphere structuring method** was anticipated and performed. It is based on directed UV irradiation and consequent exposure to solvent [Fig. 10b]. At first a monolayer of PS spheres was formed on the quartz glass substrate using spin coating method. Then the sample was exposed to UV light (wavelength of 254 nm) for a certain time. UV irradiation was routed from the bottom of the sample. The bottom half shell was supposed to be cross-linked by the UV irradiation. After that, the sample was washed by the toluene liquid to remove the non-cross-linked PS. Finally the cross-linked PS array with **bowl-like** structure was formed. The fabricated PS structures will be presented in **chapter 4**. Hereby the role of surface modification by stabilizer in the nanostructuring of PS sphere will be discussed. The produced PS sphere arrays with donut structure can be used as nanocontainers due to their high stability and tunable properties. It has a high potential applications in biotechnology, such as confined reaction vessels.[57-60]

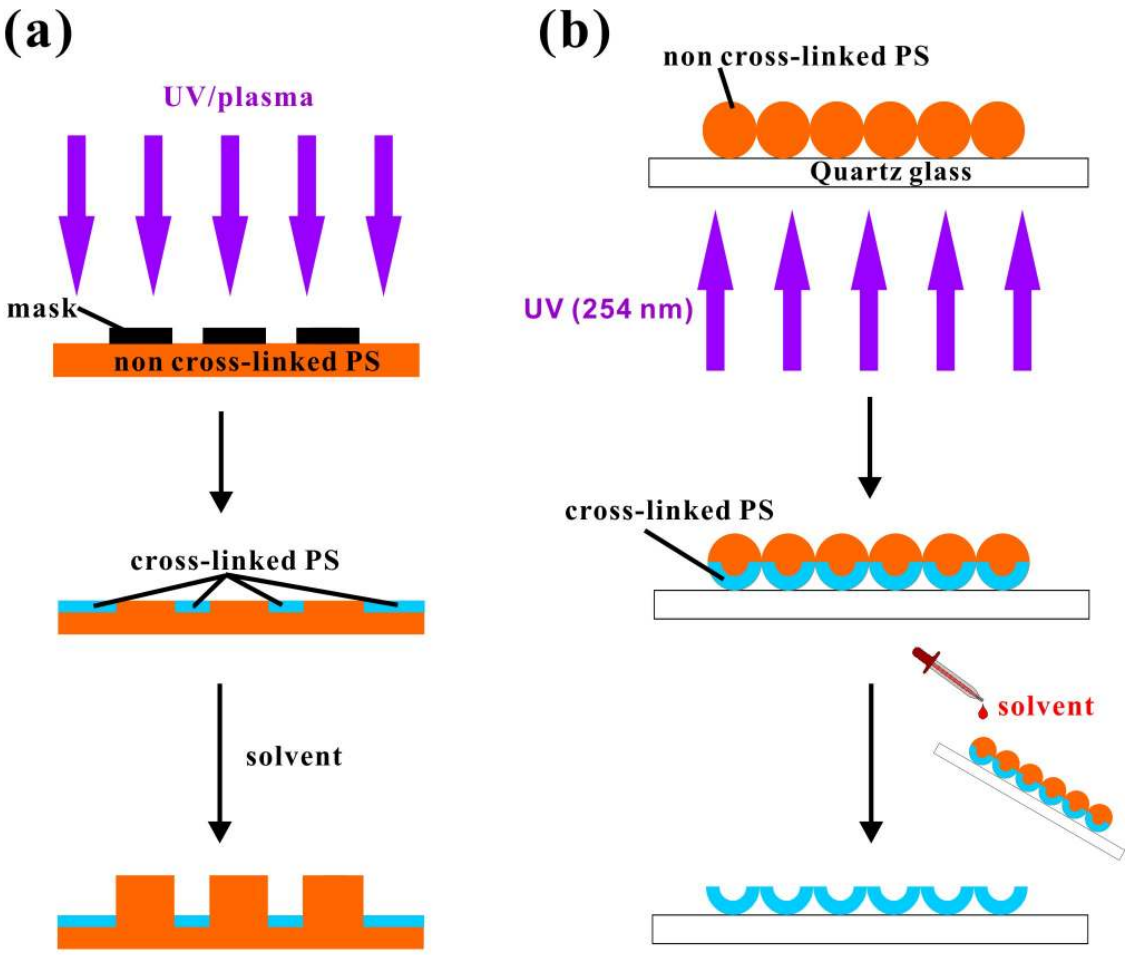

Fig. 10. Schematic drawing of the process of fabricating (a) PS array of microvessels (b) PS sphere array with donut structure.

Chapter 2

A multiwell microcantilever array sensor device for biotechnology

Sensor devices based on MCS arrays are used for chemical and biological detection. MCS transduce recognition events on their receptor-coated surface into mechanical deflections. The advantage of MCS situated in different wells is that the functionalization of surface is simplified and that standard immobilization procedures can be used. Furthermore it is capable of monitoring the deflection response of up to 16 cantilevers in parallel. In addition, a fixed mirror within each well allows to determine the absolute bending of MCS. This allows us to study hydrodynamic induced deflections in MCS. The effect of different flow rates on the cantilever deflection and mixing of the solution in the fluidic delivery system were investigated.

2.1 Calibration

The optical readout system of the MCS device is based on the beam deflection technique similar to the one used in atomic force microscopy (AFM). Therefore the measurement of cantilever deflection is related to several parameters such as the distance between cantilever and PSD, the angle of the incident laser beam and the angle of PSD.[61] Since the MCS were coated on top with a gold layer, they behave like a bimetallic actuator.[62] To verify the value of the cantilever deflection without measuring the parameters such as the distance between cantilever and PSD, the angle of PSD, we calibrated the MCS setup by measuring the absolute bending of the MCS with a white-light confocal microscope at different temperatures. A relative calibration based on heating was also reported by Yue et al.[63]

Fig. 11a shows a confocal microscope image of the gold coated side of four MCS in one well. From the image, we observe that the free end of each MCS is brighter than the

chip, which means that MCS 1 – MCS 4 are bent upward with respect to the reference mirror at room temperature. This bending is attributed to the residual stress of the deposited Ti/W/Au layers. One can see clearly that the reference mirror has the same level than the surrounding chip surface. This position is defined as zero nanometers in a profile along the free end of the MCS (indicated by a red horizontal line in Fig. 11a).

The blue spots in Fig. 11b indicate the position where the displacement of each MCS was calculated. For the four MCS of Fig. 11a we measured a displacement of the free end of 5312±1 nm (MCS1), 5425±1 nm (MCS2), 5471±1 nm (MCS3), and 5008±1 nm (MCS4) relative to the mirror level (defined as 0 nm) at room temperature of 25.2°C, respectively. The average deflection within this well was 5304±208 nm. Upon heating the chip to higher temperatures we observed, as expected, that all MCS bent away from the gold coated side towards the reference mirror. The displacement of the free end of each MCS is 1025±1 nm (MCS1), 1290±1 nm (MCS2), 1368±1 nm (MCS3), and 1212±1 nm (MCS4) relative to the mirror level at temperature of 45.5°C, respectively. The average deflection within this well was 1224±147 nm.

The vertical red dashed lines in Fig. 11a indicate the positions where the bending along the length of each MCS was measured [Fig. 11c]. Each bending of the MCS was fitted by a constant radius of curvature R with a center of circle at (y_0, z_0). The red dashed curve indicates the fitted curve. The radius of curvature for each MCS was calculated by fitting the profile with

$$(z - z_0)^2 + (y - y_0)^2 = R^2 \tag{2.1}$$

where z_0, y_0 and R are three variables with R the radius of curvature, (y_0, z_0) the center of the circle.[64] The point (y_0, 0) of transition from chip support to MCS is on the fitted circular arc and z_0=R, y_0=R are given. Because only R is the variable, the fitted curve has a more precise radius of curvature.

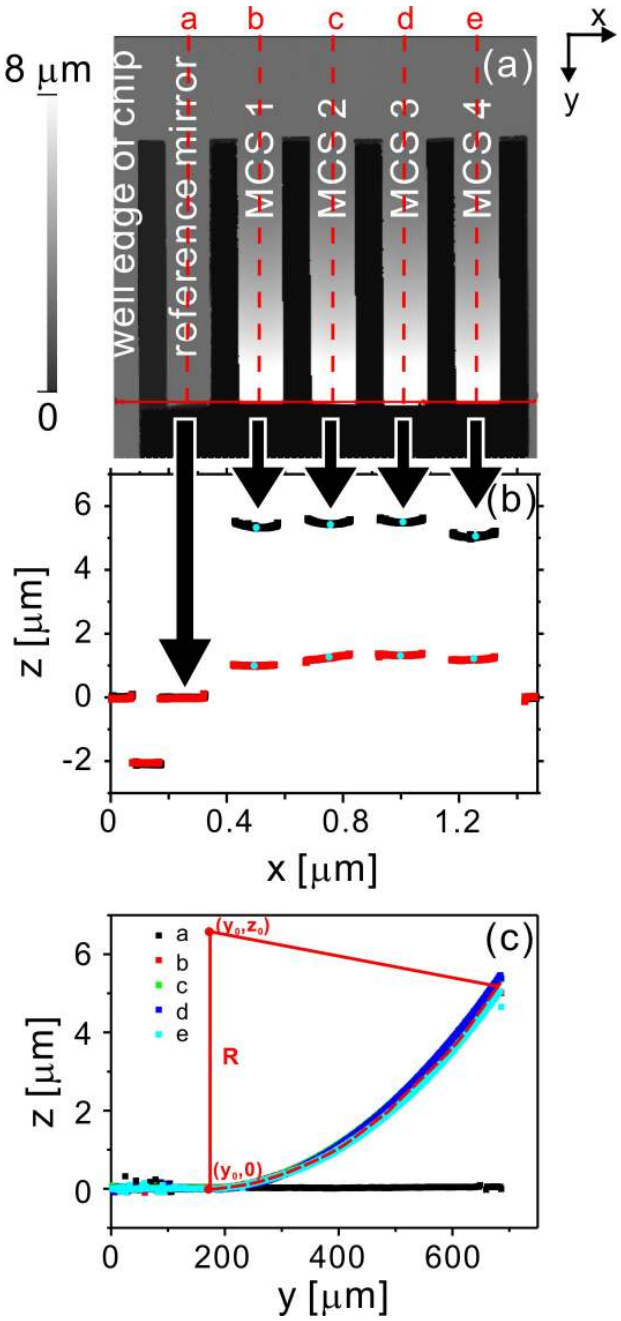

Fig. 11. (a) The shape of MCS recorded by white-light confocal microscopy at room temperature (25.2°C). (b) The profile corresponding to the bendings of the 4 MCS' ends. The black and red data correspond to the profiles at room temperature of 25.2°C and temperature of 45.5°C, respectively. (c) The profile corresponding to the bendings of the 4 MCS and reference mirror indicated by red dashed lines in (a).

The radius of curvature along the MCS length for MCS1, MCS2, MCS3 and MCS4 at room temperature of 25.2°C was calculated to be 25554±26 μm, 25275±23 μm, 24941±29 μm and 25867±55 μm, respectively. The reference mirror has an infinite radius of curvature because it is stiff. From Fig. 11b, we observed that the end of each MCS also has a curvature at room temperature. The radius of curvature of each MCS's end was measured to be 17433±8 μm, 20193±8 μm, 22363±8 μm and 14497±8 μm, respectively. It is smaller than that along the MCS length, which is contrary to the expectation. The radius of curvature of each MCS's end is expected to be larger than that along the MCS length because both edges of the MCS's end are not free, while one edge of the MCS length is free.

Since the cantilever deflection is linearly dependent on the differences in thermal expansion coefficients of silicon and gold (Eq. (2.2)), which are the two components of a gold-coated cantilever, we expect a linear dependence of cantilever deflection on the temperature change.[65]

$$\Delta z = \frac{3l^2}{\left(t_{Au}+t_{Si}\right)}\left[\frac{1+\left(t_{Au}/t_{Si}\right)^2}{3\left(1+t_{Au}/t_{Si}\right)^2+\left(1+E_{Au}t_{Au}/E_{Si}t_{Si}\right)\left(t_{Au}{}^2/t_{Si}{}^2+E_{Si}t_{Si}/E_{Au}t_{Au}\right)}\right]\left(\alpha_{Au}-\alpha_{Si}\right)\Delta T \quad (2.2)$$

where Δz is the cantilever deflection, l (500 μm) is the cantilever length, t_{Au} and t_{Si} are the thickness of gold coating and silicon substrate, respectively, E_{Au} and E_{Si} are the Young's modulus of gold coating and silicon substrate, respectively, α_{Au} and α_{Si} are the thermal expansion coefficient of gold and silicon, respectively, ΔT is the temperature change [Table 1].

	Au	Silicon
Thickness t (nm)	30±5	1000±200
Young's modulus E (GPa)	69.1±2.06[66]	166±1[65]
Thermal expansion coefficient α ($°C^{-1}$)[67]	14×10^{-6}	3×10^{-6}

Table 1. Thickness, Young's modulus and thermal expansion coefficient of gold coating and silicon substrate of the MCS.

With the values in Table 1, we calculated $\Delta z=(111.84\pm55.43)\times10^{-9}$ m/°C × ΔT using Eq. (2.2).

By fitting the average deflections of all MCS within one chip measured at 5 different temperatures (fitting by $y=a+bx$, obtained a of 10.68±0.24 nm, b of –0.207±0.0067 nm/°C), in the range 25 °C to 45 °C we found a linear dependence of bending with temperature having a slope of –207±7 nm/°C [Fig. 12]. The difference between theoretical calculation and experimental results is attributed to the Ti/W layer between the gold layer and silicon substrate, which is not considered in the theoretical calculation.

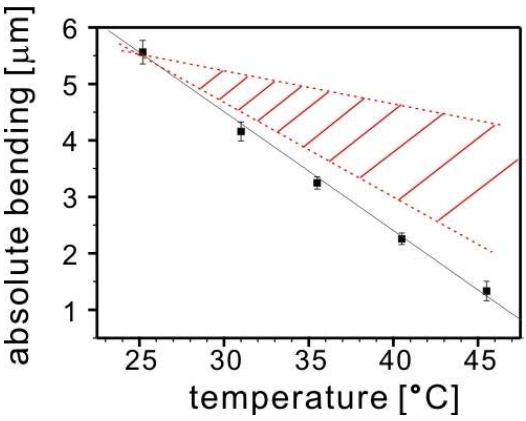

Fig. 12. The theoretical calculation (red hatched region) and experimental results (black solid line) of the average absolute bending of all Au coated MCS within one chip upon temperature change. The experimental results were measured by the white-light confocal microscopy. The slope of theoretical calculation and the linear fitting for the experimental results is –111.84±55.43 nm/°C and –207±7 nm/°C, respectively.

The MCS deflection Δz was calculated by Eq. (5.1), which is proportional to the displacement of the laser spot on the PSD. The software only records the PSD position signal (here given in arb.units), which means only the displacement of laser spot on PSD was measured. Therefore, the calibration of the system is necessary to obtain the MCS deflection value. To calibrate the optical setup, the same chip was then mounted in the device with lasers aligned on the end of reference mirrors and free ends of all MCS. The temperature of the chip was ramped from room temperature to 45.5 °C [Fig. 13]. The bending follows a linear dependence having a slope of –20.32±0.01 arb.units/°C.

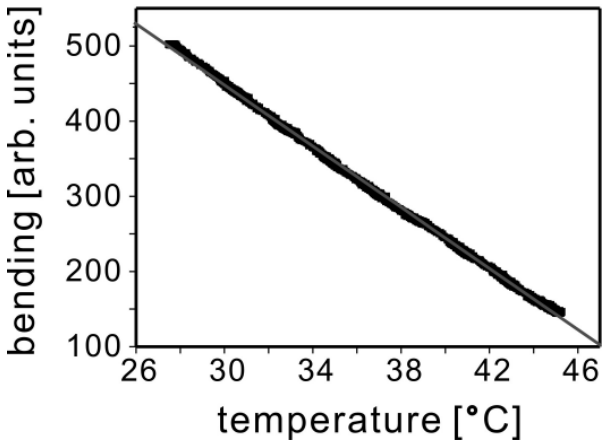

Fig. 13. The average absolute bending of all MCS within the same chip upon temperature change measured by the Veriscan3000. The slope of linear fitting is –20.32±0.01 arb.units/°C.

Together with the results from confocal microscope a conversion factor of 10.19 nm/arb.units (calculated from –207 nm/°C divided by –20.32 arb.units/°C) for the current optical setup was obtained.

2.2 Resonance frequency

Calculations of differential deflection signals only make sense if the mechanical parameters of MCS in the different wells within one chip are comparable. Therefore we determined the resonance frequencies of the sixteen MCS by recording oscillation spectra induced by thermal noise. The resonance frequency of each MCS was then obtained by fitting each spectrum with a Lorentzian curve.[68] Resonance frequencies were determined to be 5146 ± 14 Hz, 5151 ± 18 Hz, 5154 ± 15 Hz, and 5159 ± 7 Hz for MCS in well A, B, C and D, respectively. The small variation of the resonance frequencies among MCS within one chip (0.3% – 0.7%) indicates that the mechanical properties of the MCS are quite similar and are suitable for the differential deflection measurements. In addition, we observed that, frequency variations of MCS between different chips are very small within few percents [Fig. 14 and Table 2].

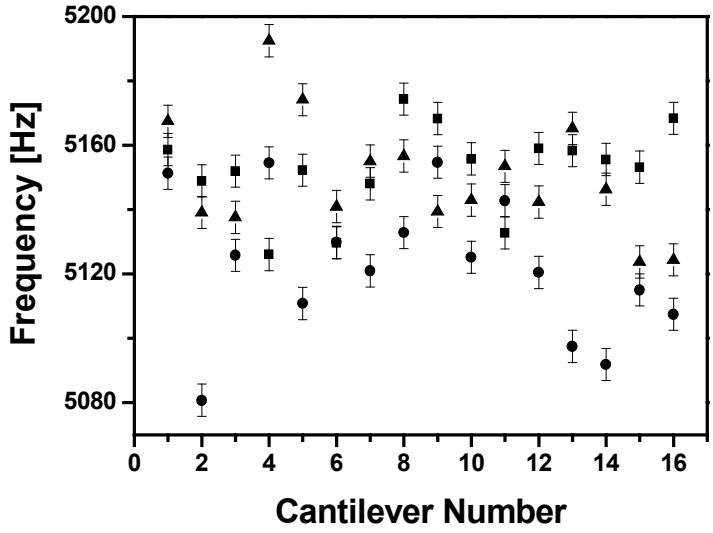

Fig. 14. Resonance frequencies of MCS obtained from thermal tune spectra. For comparison, all 16 MCS of three arbitrarily chosen chips are plotted. All resonance frequencies vary between 5080 and 5200 Hz. Squares correspond to chip 1, circles to chip 2, and triangles to chip 3, respectively.

	Average of Well A (Hz)	Average of Well B (Hz)	Average of Well C (Hz)	Average of Well D (Hz)	Average of four wells (Hz)
Chip 1	5146 ± 14	5151 ± 18	5154 ± 15	5159 ± 7	5151 ± 18 (0.35%)
Chip 2	5128 ± 34	5124 ± 10	5136 ± 16	5103 ± 10	5128 ± 34 (0.66%)
Chip 3	5159 ± 26	5157 ± 14	5145 ± 6	5140 ± 20	5153 ± 33 (0.64%)

Table 2. Average of the resonance frequency of MCS in each well and average of four wells of each chip. The variation in average value is the standard deviation among MCS. The percentage of the variation is also given for average of four wells of each chip.

2.3 Effect of different flow rates

2.3.1 Sample entry delay times

For MCS it is essential to calculate the differential deflection between functionalized and reference sensors in analyte flow in order to compensate unspecific adsorption. In our setup reference MCS are situated in different wells connected independently to the fluidic delivery system. The calculation of differential signals between wells leads to reliable data only if both wells are exposed at the same time to the same analyte flow and analyte concentration.

There is always a time delay in the MCS response after sample injection owing to the time the sample solution needs to pass through the tubing and fill the well. This depends on the flow rate and on the tubing volume mainly given by the length. Although the flow rate is the same for each well, the delay times may vary approximately 1 s due to the time delay among the injection of each well (switching the valve from “load” to “inject”). The delay times may also vary due to the different lengths of each tubing. In order to estimate delays for each well, we injected air bubbles in a water flow and monitored the PSD signal. A sudden decrease of the sum signal on the PSD indicated that an air bubble entered the well, which induces the reflected laser beams displaced out of PSD. The average delay volume was calculated to be 146 µl, 143 µl, 145 µl and 147 µl

for well A, well B, well C and well D, respectively [Fig. 15]. We observed that the bubble might be sticky for short time at the inlet of the well before it fully entered the well, which results in the different delay volume. These small differences in delay volumes are considered upon calculation of differential MCS response between different wells. In case a flow rate of 5 µl/min is used in an experiment, the delay volume results in a time offset of 36 seconds of well A relative to well B. This time offset can be subtracted from the measurement time obtained for well B.

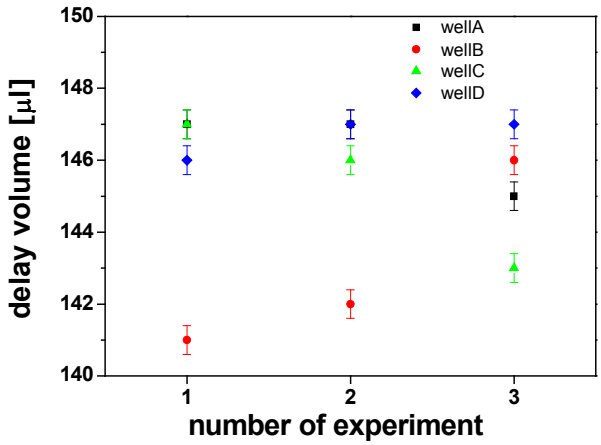

Fig. 15. Three experiments conducted to estimate the volume of delay.

2.3.2 Flow rate dependence

Typical flow rates for MCS employed in biosensing are between 5 and 100 µL/min.[69] To investigate the effect of different flow rates on the bending behavior of the MCS, we performed experiments by flowing water at different flow rates, e.g. 50, 100, 200 and 300 µL/min [Fig. 16a]. The MCS immediately responded to an increase of the flow speed by bending downwards relative to the mirror position. From these experiments the deflection jump for each flow rate change $\Delta D_{\Delta flow}$, was determined [Fig. 16b]. In Fig. 16b, the deflection jump is 80 nm for the flow increase. The deflection jump at flow decrease was calculated in the same way and 71 nm was obtained.

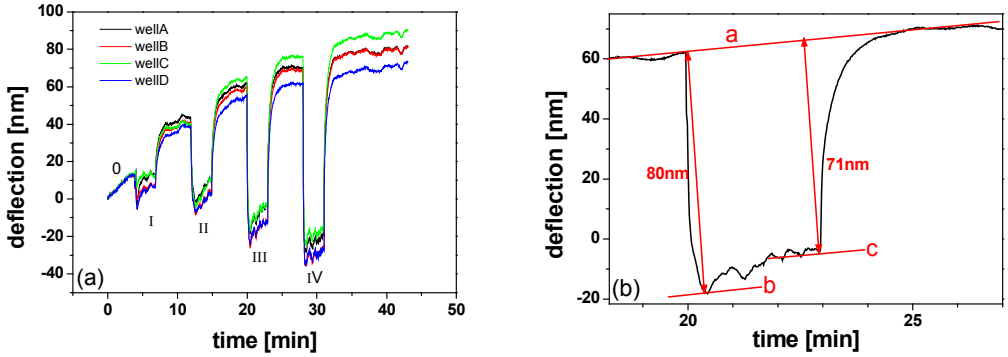

Fig. 16. (a) Bending of the MCS upon water flow at different flow rates. The traces are the average traces of 4 MCS in each well. 0 indicates no flow, I a flow of 50 µL/min, II 100 µL/min, III 200 µL/min, and IV 300 µl/min, respectively. (b) Deflection jump calculated from a. The drift was fitted by line marked with "a". The plateau of the deflection jump at flow increase was fitted by line b, which is parallel to the line a. Then the deflection jump was calculated from the starting point of flow increase to the plateau.

All the jump heights $\Delta D_{\Delta flow}$ calculated from the measurement shown in Fig. 16 were plotted as a function of flow rate [Fig. 17].

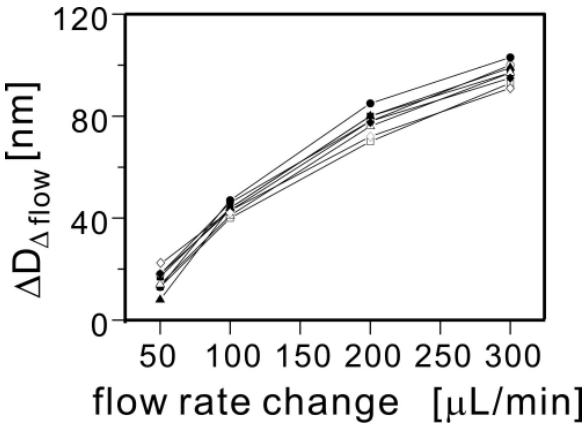

Fig. 17. Jump height $\Delta D_{\Delta flow}$ calculated from the measurement shown in Fig. 16 as a function of flow rate. Filled symbols correspond to a flow increase and open symbols to a flow decrease. Squares correspond to well A, circles to well B, triangles to well C, and diamonds to well D.

We conclude first, that $\Delta D_{\Delta flow}$ of the MCS increases with increasing flow rates. Second, that the effect of flow rate on $\Delta D_{\Delta flow}$ is reversible, because the jump height of

flow increase and that of flow decrease is quite similar. Thus the flow rate effect is attributed to forces arising from the hydrodynamic flow surrounding the MCS. Consequently, using MCS which have different layout, shape, bending or higher order of curvatures exhibits different flow rate effects, which is discussed in the following paragraph.

2.3.3 Flow rate dependence on MCS with different curvatures

The flow rate experiments were repeated with additional three chips to demonstrate the influence of the absolute bending of MCS to its bending changes. Therefore we have selected MCS chips having a different initial absolute bending at room temperature of 5733 nm, 4742 nm and 1385 nm in average for chip 1, chip 2 and chip 3, respectively [Fig. 18]. The absolute bending direction of all MCS is upwards (towards the gold side) relative to the zero level of the mirror. We found that $\Delta D_{\Delta flow}$ is larger for the MCS of the chip having larger absolute bending, i.e. $\Delta D_{\Delta flow,chip1} > \Delta D_{\Delta flow,chip2} > \Delta D_{\Delta flow,chip3}$. This dependence indicates that there is a more pronounced effect of the flow change on the MCS exhibiting a higher bending.

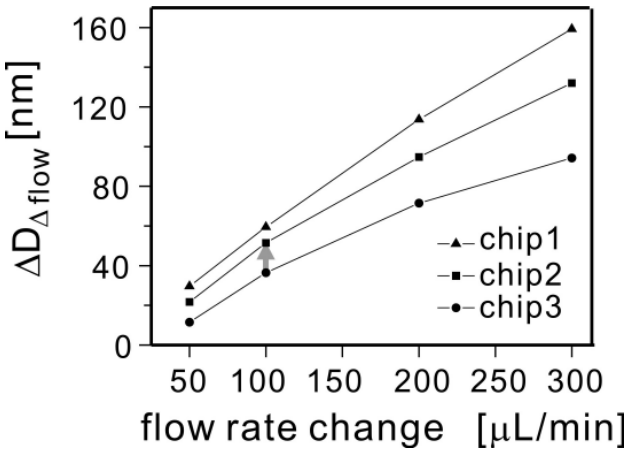

Fig. 18. Average jump height $\Delta D_{\Delta flow}$ of four wells as a function of flow rate for three different chips.

This effect may sound trivial, but it has consequences for in-flow experiments in terms of differential measurements between reference and sensing MCS. The sensing and the reference MCS are comprised usually of different surfaces. Since different surfaces can have different surface energies, a different surface stress acts on the MCS. Thus the initial bending of MCS is already different prior to the sensing experiment. One example is when MCS are coated by a gold layer for thiol immobilization of molecules and reference MCS stay uncoated. The Au coating process is known to result in a bending of MCS.[70] In this case a change in the flow speed would induce a "parasitic" differential deflection. Consequently, MCS experiments should always be performed or compared which were recorded at a constant flow rate.

Of course, since the measurement of the MCS bending is fundamental and it is the quantity to be measured upon exposure to an analyte, the influence of the absolute bending in an experiment must be considered even at constant flow. Upon binding of molecules to a MCS surface, bending of several micrometers were reported.[71] To illustrate the influence of hydrodynamic flow induced response on MCS, an initial absolute bending of the MCS of approx. 1400 nm is assumed (the initial absolute bending of chip 3 is taken as an example). In addition, we assume that the binding of molecules leads to a bending change of 3300 nm (for example, the difference of initial absolute bending between chip 2 and chip 3). The difference in hydrodynamic flow induced bending would be in the order of 15 nm (see gray arrow in Fig. 18) or around 0.5 % (15 nm divided by 3300 nm), which can be considered as negligible. However, the above measurements and considerations demonstrate that measurements of the absolute bending of MCS lead to a more detailed understanding of its sensing mechanisms and can improve the reliability of the obtained experiment.

2.4 Mixing of solutions during sample injection

When dealing with adsorption kinetics, it is important to know not only the delay between sample injection and introduction into the measurement chamber, but also the mixing behavior of the analyte and carrier fluid inside the entire fluidic system.

As a model of analyte/carrier fluid, we used deionized (DI) water and bovine serum albumin (BSA) solution (5mg/ml, BSA in water), which is known with high refractive index. The refractive index of pure water and BSA solution is 1.3325[72] and 1.34-1.5 at 25°C, respectively.[73-75] To increase the effect of refractive index changes on the displacement of the reflected laser beams, we tilted the cartridge hosting the MCS array. To be sensitive to changes in refractive index only, all laser spots were focused on the rigid chip surface (instead of the free end of the cantilever). Thus, recorded deflection signals do not correspond to a real deflection. Therefore we referred to this signal as position offset. In the beginning, the wells were filled with DI water at a constant flow rate of 10 μL/min. Under this condition, the position offset is attributed to a BSA concentration of 0. Thereafter a BSA water mixture in well B and D is introduced and the position offset is monitored [Fig. 19]. The flow rate was kept at 10 μL/min. At t = 21 min BSA was injected in well B and D. The arrow shows at t = 36 min BSA reaching the cell and at t = 64 min BSA completely flowing out of the cell. Three regions can be distinguished: a first interval t_1 (3 min) where the BSA solution mixed with carrier fluid flowing in the cell, a second interval t_2 (13 min) where only the analyte BSA solution is present in the cell, and a third interval t_3 (11 min) where the analyte solution is washed away by the water carrier fluid.

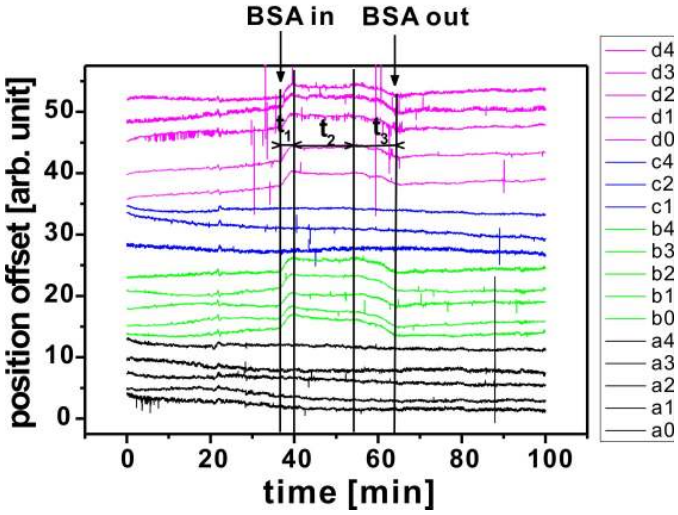

Fig. 19. Position on PSD signal of BSA mixing with carrier fluid water.

In Fig. 19 we observed that when BSA reaching the cell, the position offset increased, owing to an increase in refractive index upon switching from water to the BSA solution. This phenomenon is in agreement with the theoretical expectation [Fig. 20].

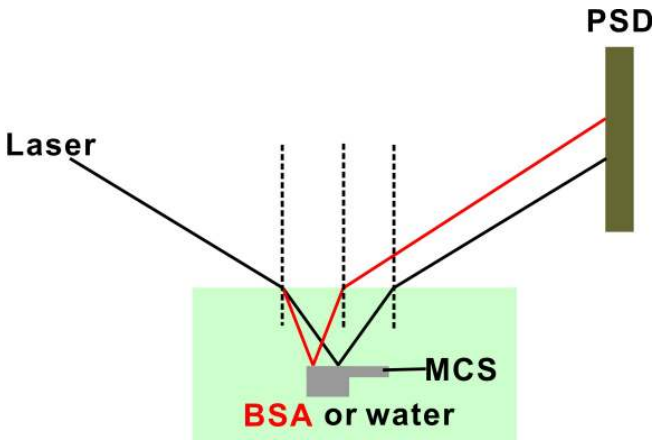

Fig. 20. The schematic drawing of the laser path in the solution. The red line and black line corresponds to the laser path in BSA solution and water, respectively. The refractive index of pure water and BSA solution is 1.3325 and 1.34-1.5 at 25°C, respectively.

The injection of the BSA water solution resulted in a transition time of 3 minutes, corresponding to a volume exchange of 30 μL in well B and D. After that, the position offset reached a constant value, which is attributed to a constant concentration of the BSA water mixture (13 minutes or a flow volume of 130 μL). Then the BSA water mixture was exchanged by DI water again. The position offset signal returned to the initial value after 11 minutes (corresponding to 110 μL volume exchange). In a control experiment, the flow of water alone in well A and C produced no change in position on PSD signal.

To better understand the mixing dynamics, we focused on the measurement chambers, which consisting of an inlet, outlet, and the chip well with the four MCS and the reference mirror as depicted in Fig. 21a. Finite element method (FEM) simulations (done by S. Lorenzoni in University of Genoa) revealed the flow profile within a well [Fig. 21b]. The profile shows that the flow is fast in the middle of the well and slow at the walls of the well.

The time dependence of the BSA concentration calculated at the free end of the MCS was compared to position offset signal in our refractive index measurement [Fig. 21c]. The simulation results show good agreement with our experimental observation. The transition time t_1, t_2 and t_3 were calculated for experimental result and simulation result [Table 3]. For the experiment result, t_1 was defined by the region with position offset increasing from 0.8 to 2.0, where the position offset has an abrupt slope. The t_2 was defined by the region with position offset fluctuating between 2.0 and 1.8, where the position offset has a plateau. The t_3 was defined by the region with position offset decreasing abruptly from 1.85 to 0.8. After that the position offset fluctuates between 0.8 and 0.4. For the simulation result, t_1 was defined by the region with normalized concentration increasing from 0 to 0.9. The t_2 was defined by the region with normalized concentration increasing from 0.9 to 1.0 and decreasing from 1.0 to 0.9. The t_3 was defined by the region with normalized concentration decreasing abruptly from 0.9 to 0. We observed that t_3 is larger than t_1, the reason is that the volume of mixed solution in the tail part is more than the that in the head part, which is due to the more mixing time for the tail part of the solution when flowing through the detected position. The simulation result shows no plateau in the t_2 region, which means that there is no stationary

concentration in the solution in ideal case and all the solution is mixed. The result of the simulation and the experiment indicates that the signal recorded from the reference mirror within one cell can be used to monitor the concentration changes owing to mixing effects in each well.

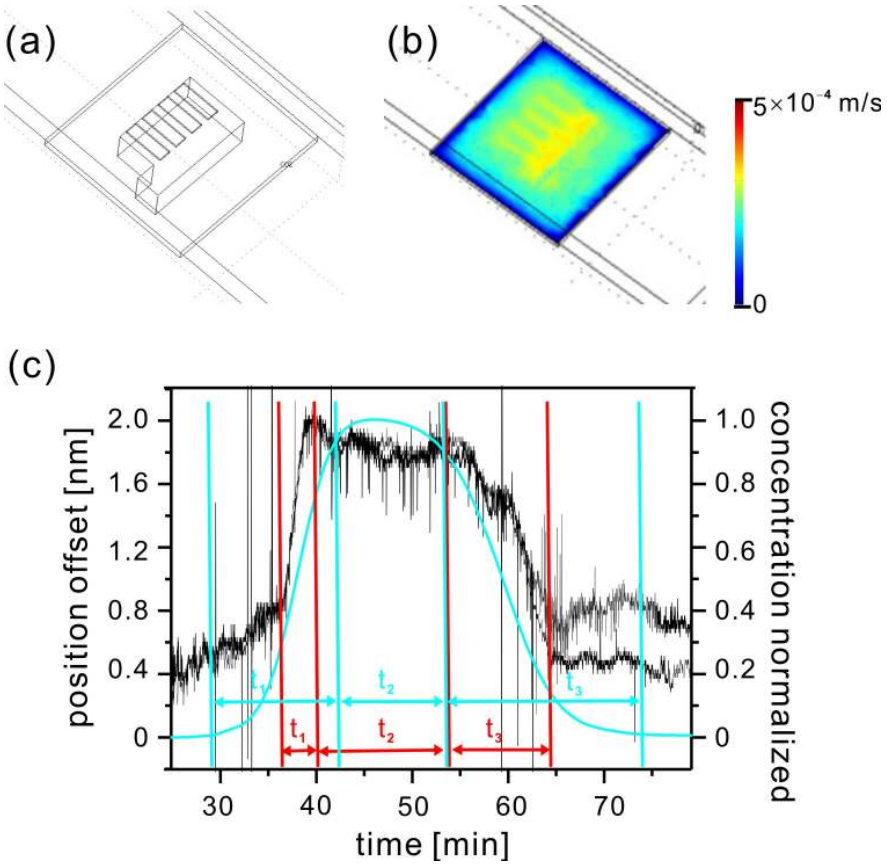

Fig. 21. (a) View of one of the four identical flow-through measurement chambers. (b) Stationary velocity field of the flow through chamber obtained by finite element method (FEM) simulation. The color corresponds to the flow velocity and its scale ranges from 0 - 5 $\times 10^{-4}$ m/s. (c) Two exemplary position offset signals upon exchange of water with BSA water solution (black curves). The blue solid curve represents the simulated concentration dependence for the same experiment. The blue and red arrows correspond to the regions defined for simulation result and experimental result, respectively.

	t_1 (min)	t_2 (min)	t_3 (min)
experiment	3	13	11
simulation	14	11	20

Table 3. Transition time t_1, t_2 and t_3 calculated from Fig. 21a for experimental result and simulation result.

2.5 DNA hybridization experiment

To evaluate the performance of the Veriscan system, we conducted a standard DNA hybridization experiment.[76-78] It consists of three steps: probe immbolization, thiol blocking and hybridization [Fig. 22]. In the first step a single-stranded DNA (5'-HS-$(CH_2)_6$-GGCCATCGTTGAAGATGCCTCTGCC-3', Sigma-Genosys, USA) was used as probe molecules. To break the disulfide bonds present in the probe molecules, a reducing agent TCEP· HCl (Tris 2-carboxyethyl phosphine, Pierce, Rockford, USA) was used, which is explained in the sample preparation section in chapter 5.1.1. Immobilization buffer (KH_2PO_4 1M, pH 3.8, prepared in the physiology lab of Genoa University in Italy) was used to stabilize the probe molecules and deliver them to the MCS as a carrier fluid. In the second step, the thiol solution MCH (6-mercapto-1-hexanol, SH-$(CH_2)_5$-CH_2OH, Mw: 134.24 g/mol, Fluka, Buchs, Switzerland) was used to enhance the recognition of the following hybridization and prevent the unspecific adsorption (explained in detail in the following section). In the third step, target molecules (5'-GGCAGAGGCATCTTCAACGATGGCC-3', Sigma-Genosys, USA) with the base pair sequences complementary to that of the probe molecules were used to hybridize with the immobilized probe molecules. The non-complementary molecules (5'-GATTAGAGTCCCGCAATTAATCATT-3', Sigma-Genosys, USA), which do not hybridize with the probe molecules, were also used as a reference to compensate the unspecific adsorption on the MCS. In this step the hybridization buffer (NaCl 150 mM, Na_2HPO_4 20 mM, EDTA 0.1 mM, pH 7.4, prepared in the physiology lab of Genoa University in Italy) was used to stabilize the target molecules and deliver them to the MCS as a carrier fluid.

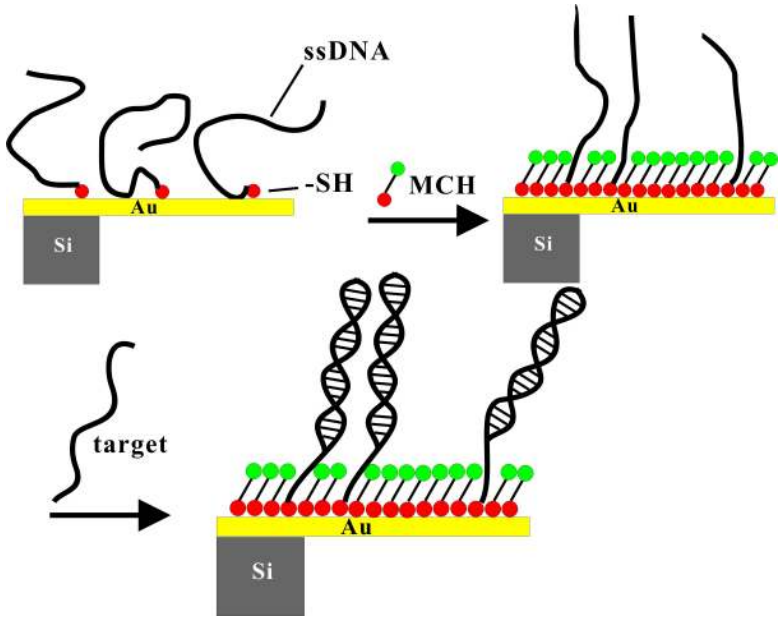

Fig. 22. Schematic drawing of probe (ss DNA) immobilization, MCH adsorption and DNA hybridization.

2.5.1 Probe immobilization experiment

To evaluate the performance of the sensor array to the specific interactions, we conducted a probe immobilization experiment using a thiolated DNA molecules [Fig. 23]. After the cantilevers were stabilized in the carrier fluid of immobilization buffer, 200 µL sample solution was injected in the flow stream. The flow rate was kept at 2 µL/min. The curves shown in the graph have already been drift subtracted. At t = 33 min sample solution was injected in well A and D. The arrow shows probe molecules reaching the cantilever at t = 93 min and flowing out of the cell at t = 193 min. The absolute bendings of the cantilevers at the beginning of the experiment are 3850 nm and 3430 nm up relative to the reference mirror for well A and well D, respectively. The flow of probe solution in the fluid cell was kept at constant flow rate for 2 hours. After the flow of sample solution, carrier fluid was delivered again to wash the unbound probe molecules. When probe molecules reach the cantilevers in the cell, the deflection starts to decrease significantly. The negative and decreasing deflection denote that the cantilever bends down. It is attributed to a compressive surface stress change[79-82] induced by an adsorption

layer on the cantilever. A compressive stress means that the surface of the cantilever is expanding relative to the cantilever substrate (Si), which will cause the cantilever to bend away from the expanding surface layer (Au + adsorption layer). It is attributed to the intermolecular repulsive force in the adsorption layer. The adsorption is known following the Langmuir adsorption isotherm model:

$$\theta \propto 1 - e^{-kt} \tag{2.3}$$

where θ the surface coverage, k the reaction rate, t the time.[79]

The surface coverage θ is a ratio of the number of adsorbed molecules to the total number of available binding sites.

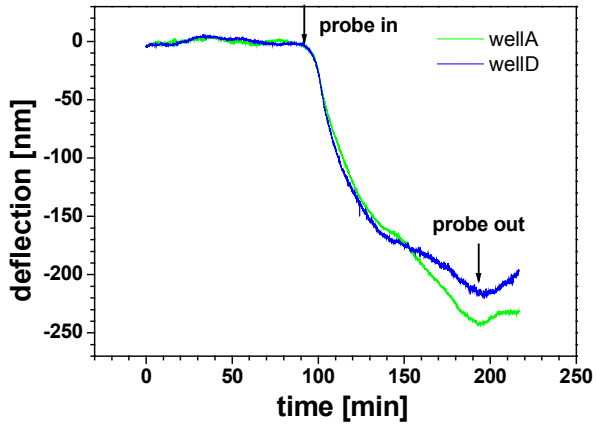

Fig. 23. Deflection of the cantilever for thiolated DNA probe molecules (50 μM) adsorption. Immobilization buffer was delivered as a carrier fluid.

The maximum deflection obtained for probe immobilization of well A and well D is 242 nm and 216 nm, respectively. At the beginning of the adsorption, the decreases of deflection are very similar for both wells. After immobilization buffer resumes flowing in the cell, the deflection increases around 10 nm, which means some unspecific bonded molecules are washed away from the cantilevers. The MCS deflections of 40 nm and 200 nm induced by ss DNA probe immobilization were also reported by Alvarez et al. and Lechuga et al., respectively.[83,84] The difference in the MCS deflections among these reports was attributed to the different geometry (length and thickness) and properties

(Young's modulus and poisson's ratio) of the MCS that were used, which result in the different surface stress change, as depicted in Eq. (5.2).

2.5.2 Thiol adsorption experiment

To investigate the cantilever response upon different molecules adsorption, we conducted thiol adsorption experiments using 6-mercapto-1-hexanol (MCH) [Fig. 24] in addition to the probe molecules. The chip used was different from the one that used in the above described probe experiment and there were no probe molecules immobilized on the MCS. The Au coated MCS were immersed in water at a constant flow rate of 5 µL/min until an equilibrium in the drift of the bending was reached. Then, without stopping the flow, 200 µL MCH solution at the concentration of 1 mM were injected in well B and D followed by water again to remove unbound MCH molecules from the MCS surfaces. The initial absolute bending of Au coated MCS, due to residual stresses, is a few µm upward relative to the reference mirrors (i.e. towards the gold side). Upon MCH exposure of the MCS in well B and D the deflection decreases significantly by around 600 nm towards the reference mirrors.

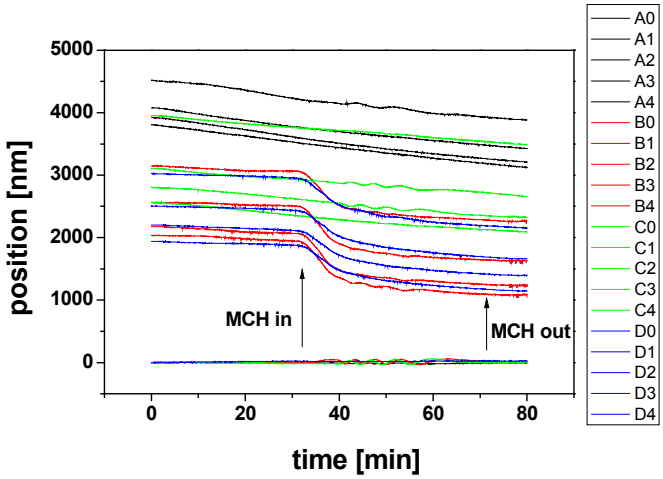

Fig. 24. Position signals of all MCS for MCH (1mM) adsorption. Deionized water was delivered as a carrier fluid. The flow rate was kept at 5 µL/min. At t = 8 min MCH was injected in well B and D. The arrow shows at t = 31 min MCH reaching the MCS and at t = 71 min MCH flowing out of the cell.

To compare the signals which were recorded in the different wells, the average deflection signals in each well were calculated. Then the signals recorded from reference wells A and C were subtracted from the signals recorded for well B and D [Fig. 25].

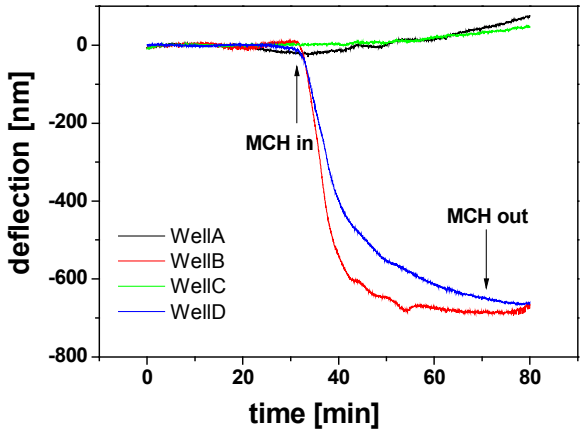

Fig. 25. Average deflection of four wells calculated from Fig. 24. The curves shown in the graph have already been drift subtracted.

Hereby the initial deflection was defined to be zero for all wells. The deflection changes indicate an increase of the compressive stress of the gold coated side[79-81] induced by the self assembled monolayer on the MCS. A compressive stress means that the gold side of the MCS is expanding relative to Si. The maximum deflection of well B and well D are 688±5 nm, 662±5 nm, respectively. This indicates that the coverage of MCS surfaces by MCH molecules is similar for both wells. The slight different maximum deflection and kinetics in deflection are attributed to the different thickness and surface roughness of the MCS, respectively. The deflection induced by MCH adsorption was found to be dependent on the gold surface with different deposition rates.[70] After water rinsing through the cell, the deflection signals show a slight variation, within 10 nm, which indicates that immobilized MCH molecules mainly contribute to the observed bending. The control experiments were performed by water flow in well A and well C. The deflection changes in these two reference wells were observed to be < 80 nm. The deflection of 200 nm and 1000 nm induced by MCH adsorption was also reported by Mertens et al.[70,85]

Compared to the results of probe immobilization (deflection around 200 nm), the deflection is much larger for the MCH adsorption (more than 600 nm). The reason is that the concentration of MCH (1mM) is much higher than that of probe solution (50 μM). There are more MCH molecules occupying the MCS surface, which results in the more steric repulsive force. The difference in surface stress increases with increasing repulsive force, which results in the larger deflection [Fig. 26].

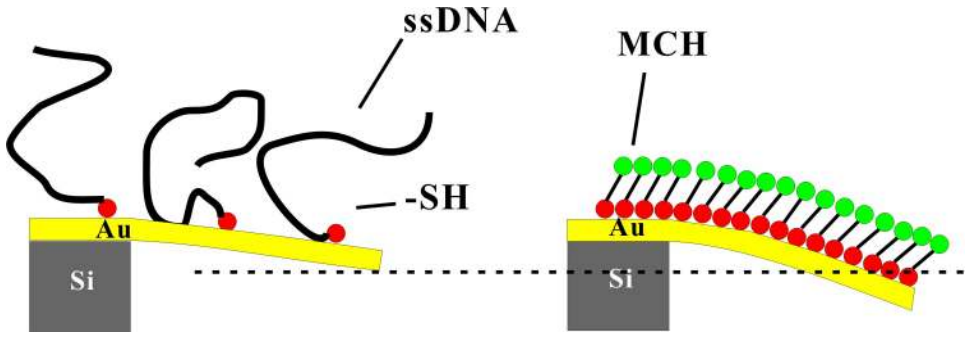

Fig. 26. Schematic drawing of MCS deflection induced by ss DNA or MCH adsorption. The MCH adsorption induces larger deflection than ss DNA adsorption.

2.5.3 Hybridization experiment

The DNA hybridization was conducted on an array where the probe and MCH molecules were already immobilized [Fig. 27]. Hybridization buffer was delivered as a carrier fluid. The flow rate was alternated between 6 µl/min and 120 µl/min twice in the beginning to check whether the flow rate has an influence on the MCS deflection. Complementary (500 nM) and non-complementary (500 nM) target solutions were injected at t=48.5 min in well C and well B, respectively. The non-complementary target was used to compensate the undesired signal from unspecific adsorption on the MCS. After target injection, fast flow rate of 120 µl/min was used for 1 minute to reduce the delivery time of sample solution from the injection loop to fluid cell (which is the sample entry delay time described in chapter 2.3.1) and then with slow flow rate of 6 µl/min to recognize the hybridization process between probe molecules and target molecules. At t=85 min fast flow rate of 120 µl/min was used again to completely wash away the target solution. The results of differential signal (red) shows that there is a pronounced deflection due to the hybridization. The deflection is attributed to electrostatic repulsive forces between negatively charged phosphate groups in DNA double helix strands and steric repulsive forces among DNA double strands.[18,86] Before target injection, we observed that the drift in deflection for well B and C is different, which is attributed to the different hydrodynamic flow induced bending due to different initial bending and different slow electrochemical processes such as silicon hydration.

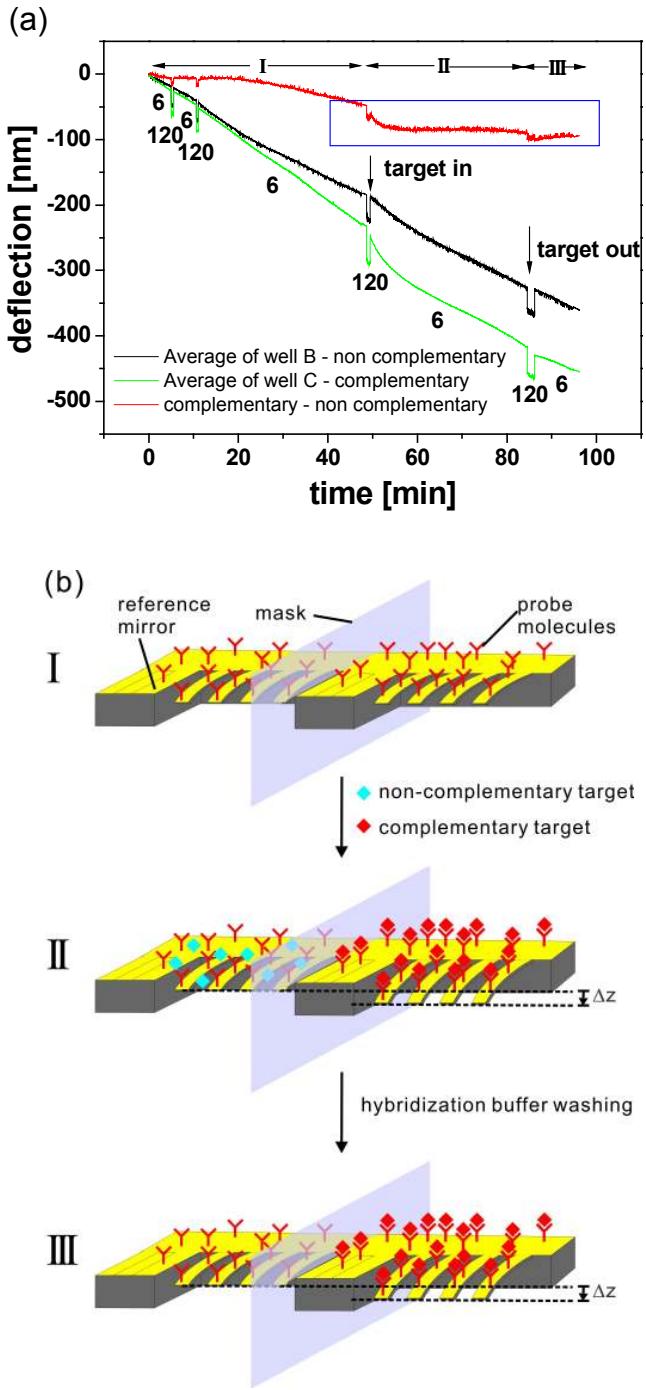

Fig. 27. (a) Deflection signals of the MCS for hybridization. The black and green curves shown in the graph are original average deflection curves without drift subtracted. The red curve is the differential curve. (b) Schematic drawing of states I, II and III indicated in (a). The deflection Δz is induced by the hybridization of complementary target molecules with probe molecules.

The inset (the blue rectangular region) in Fig. 27a was magnified in Fig. 28. We see that after target injection, there is a significant jump within the first 1 minute due to fast flow. When the flow returned to the slow flow rate, the deflection did not return to the value when the fast flow rate started. It is attributed to the effect of different flow rates on the MCS with different curvatures (described in chapter 2.3.3). It may also include the contribution of hybridization of some target molecules with the probe. Then the deflection starts to increase and after 3 minutes, it reaches the maximum value. The gap between two horizontal guidelines is 15 nm, which is attributed to the DNA hybridization. The MCS deflection of 5-20 nm induced by hybridization was also reported by McKendry et al.,[18] Fritz et al.[1] and Wu et al.[86]

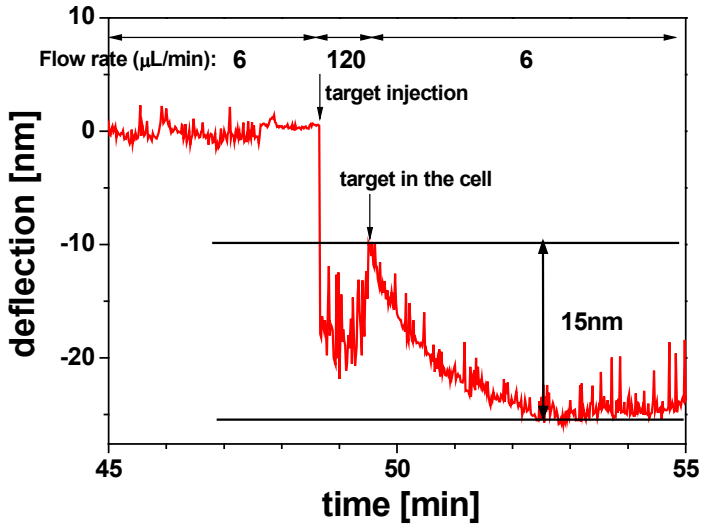

Fig. 28. Magnification of the blue region in Fig. 27a. The linear drift before target injection was already subtracted. The gap between two horizontal lines indicates the deflection induced by the DNA hybridization. The flow rate was 6 μL/min before target injection. Fast flow rate of 120 μL/min was used for 1 min at t = 48.5 min. Then the flow rate was switched to 6 μL/min again.

2.5.4 Deflection dependence on different thiol concentrations

To investigate the cantilever deflection response upon the adsorption of molecules with different concentrations, MCH solutions with different concentrations were used. The flow rate was 3 μL/min in all the experiments. The maximum MCS deflections upon adsorption of MCH with different concentrations are summarized [Fig. 29].

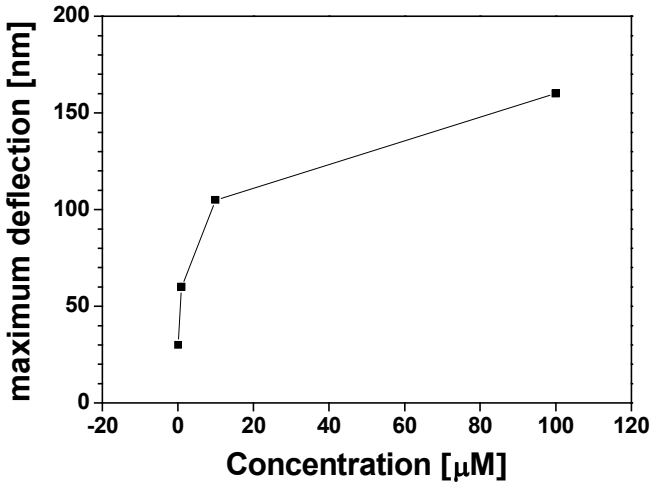

Fig. 29. Maximum deflection as a function of concentration for MCH adsorption experiments.

The results indicate that the maximum deflection increases with increasing concentration of MCH. The reason is that the surface coverages of MCS by adsorbed molecules are not saturated in all experiments. The duration of MCH flowing in the wells is only 1 hour. Since the adsorption rate is low for solutions at low concentrations, 1 hour is not enough for the molecules to fully cover the MCS surface, which can be deduced by Eq. (2.3) (the solution with low concentration exhibits the low adsorption rate k. To obtain the same surface coverage θ, t is longer for lower k). We expect that with solutions flowing for enough time, the maximum deflection would be the same for all the MCH concentrations [Fig. 30].

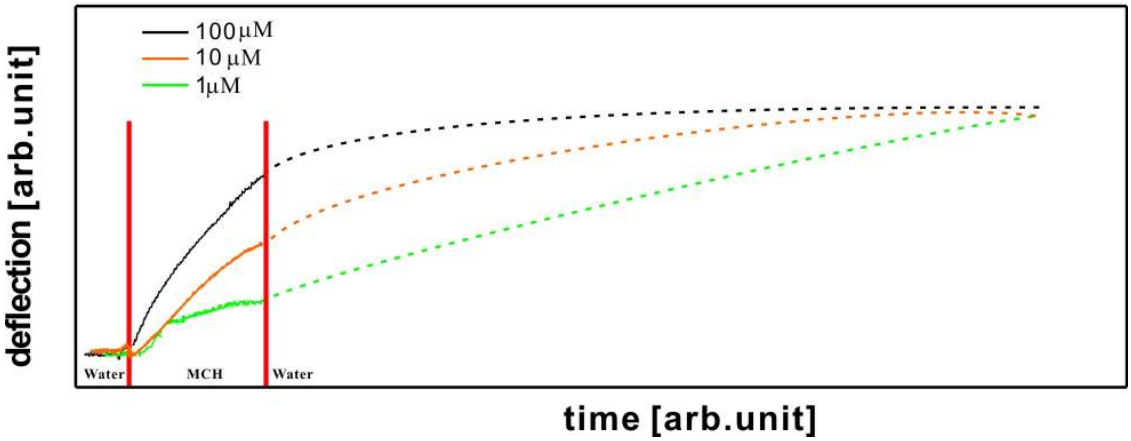

Fig. 30. Schematic drawing of deflection curves of MCS induced by MCH adsorption with different MCH concentrations. The red lines indicate the region when MCH was delivered in the cell. The solid curves are the experimental results and the dashed curves show the tendency if MCH continues to flow in the cell.

Chapter 3

Investigation of swelling of cross-linked polystyrene spheres in toluene vapor

As motivated in chapter 1, the solvent vapor annealing of micron-sized PS particles was used as a model system to study the uptake and release of solvent molecules in detail. The recognition of uptake and release of solvent molecules can be transduced into frequency shifts.

In this chapter the results of the swelling of cross-linked PS spheres in toluene vapor are presented. In particular, the mass uptake/loss and volume expansion/shrinkage of the polymer particles, the diffusion dynamics of the solvent molecules, the size dependence and the influence of UV light irradiation are investigated using MCS operated in the dynamic frequency mode. The influence of UV light irradiation on particle swelling is also investigated by confocal microscopy.

For an end-loaded MCS the mass change can be calculated by Eq. (3.1)

$$\Delta m = \frac{K}{4\pi^2}\left(\frac{1}{f_p{}^2} - \frac{1}{f_0{}^2}\right) \tag{3.1}$$

where K is the spring constant, f_p is the resonance frequency of the MCS including the sphere, and f_0 is that one of the bare cantilever. To avoid an individual calibration of K for each MCS, the relative mass increase (RMI) of the sphere is calculated by Eq. (3.2)

$$RMI = \frac{\Delta m_t}{\Delta m_i} = \frac{\left(\frac{1}{f_t^2} - \frac{1}{f_0{}^2}\right)}{\left(\frac{1}{f_i^2} - \frac{1}{f_0{}^2}\right)} \tag{3.2}$$

where Δm_t the mass of the sphere in saturated toluene in N_2 carrier gas, Δm_i the original mass of the sphere before swelling, and f_t and f_i the corresponding resonance frequencies of the MCS.

3.1 Investigation of swelling of PS particle in toluene vapor using MCS

3.1.1 Mass uptake/loss of cross-linked PS particle in toluene vapor

The resonance frequency of MCS with an attached PS sphere varies as a result of swelling upon exposure to toluene vapor [Fig. 31]. In the beginning of each experiment the fluid cell was exposed to pure N_2 gas at a flow of 2 l /h for 5 min and a constant frequency of 333.8 kHz±10 Hz was observed. From the frequency shift to the unloaded MCS (352.8 kHz±10 Hz) a mass of 2191.9±2.3 pg for the PS sphere was calculated using Eq. (3.1). At t=5 min the cell was flooded with saturated toluene vapor. Instantly the resonance frequency of the MCS decreased to the frequency of 322±200 Hz within 10 s. After 70 s, a constant frequency of 321 kHz±200 Hz was obtained. This value corresponds to a mass of 3896±28 pg, i.e., a relative mass increase (RMI) of 1704±28 pg or 179%±1%, owing to the swelling of the PS sphere in toluene. After 15 min the saturated toluene vapor was replaced with pure N_2, resulting in a resonance frequency increase. In the beginning, a rapid decrease of RMI (180%-120% in 2 s) was observed, which is followed by a slow decrease (120%-109% in 10 min), both owing to the deswelling of the PS sphere in toluene. To check the reproducibility, the exposure to saturated toluene vapor was repeated. We recorded a similar RMI of 179%±1% for the second and third swelling processes. The deswelling was reproduced, too. After the third cycle we recorded the shift of the frequency in the N_2 flow for 24 h. The resonance frequency returned close to its starting value of 333.6 kHz corresponding to a RMI of 102%. However, in all experiments we found that the mass always remained higher compared to that of the PS sphere before the first exposure to toluene saturated vapor. From this we conclude that a small fraction of toluene is remaining in the PS for a longer time.

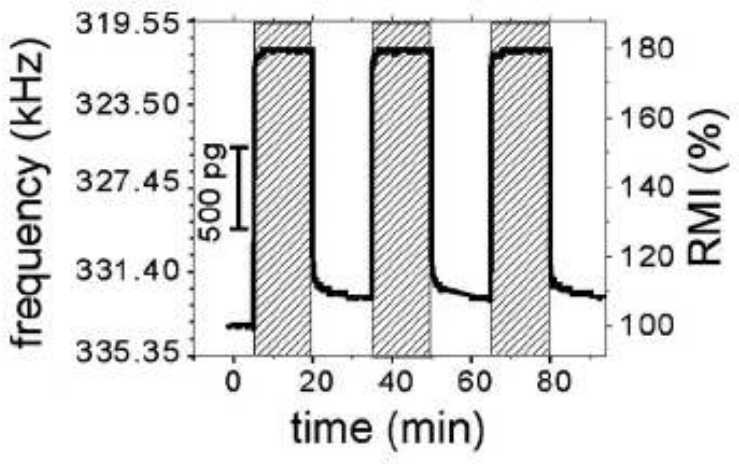

Fig. 31. Frequency response and relative mass increase (RMI) of the MCS end-loaded with a PS sphere (diameter of 16±1 μm) upon exposure to N_2 and saturated toluene in N_2 gas flow (hatched areas). The spring constant of the bare MCS was 91.9 N/m calculated using Eq. (5.4). The frequency data were recorded every 0.3 s.

The mass change of PS is calculated for each cycle by Eq. (3.1) and the swelling part of each cycle was fitted by Eq. (3.3):

$$\Delta m = a + b \times e^{-k(t-c)} \tag{3.3}$$

where Δm the mass change, a, b and c the three fitting parameters with the unit of pg, pg and s, respectively, k the diffusion related coefficient with the unit of s^{-1}, t the time [Fig. 32].

The parameter a and c is the Δm at saturation of swelling and the time that swelling starts, respectively. Therefore these two parameters can be fixed while only b and k were variables. For first cycle, second cycle and third cycle, we obtained k is 0.068±0.002 s^{-1}, 0.054±0.002 s^{-1} and 0.054±0.002 s^{-1}, respectively. The k of first cycle is larger than that of second cycle and third cycle, which means the diffusion of toluene molecules into the PS particle is faster for the first cycle. It is possibly due to the residual toluene molecules after first cycle, which slightly hinder the diffusion of toluene molecules in the second and third cycle.

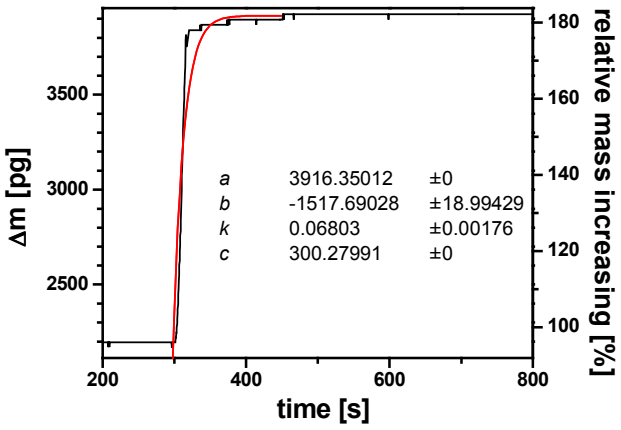

Fig. 32. Mass change and relative mass increase (RMI) of the first cycle in Fig. 31. The red curve is the fitting curve using Eq. (3.3).

The resonance frequency change of the MCS without an end-loaded PS sphere upon exposure to toluene vapor is around 80 Hz [Fig. 33]. Compared to the frequency change of >10 kHz for MCS with end-loaded PS sphere, this small frequency shift is attributed to damping by the exchange of environment. The corresponding mass change is 8 pg if we assume that the spring constant does not change. But this mass change has no meaning, because there is no specific mass loading on the free end of the MCS.

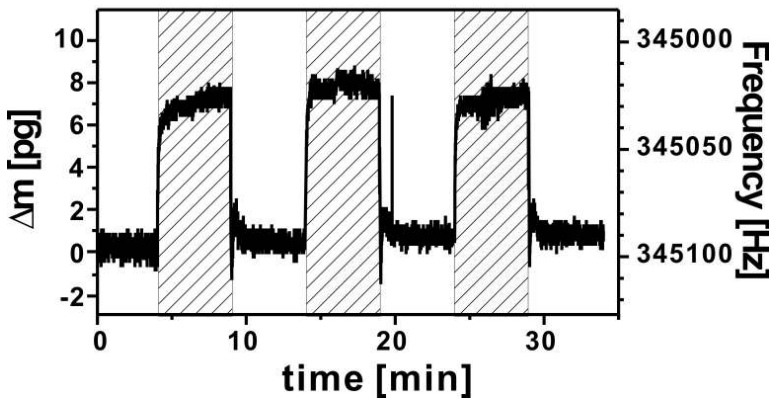

Fig. 33. Frequency response and mass change Δm of a bare MCS upon exposure to N_2 and saturated toluene in N_2 gas flow (hatched areas). The spring constant and resonance frequency of the bare MCS was 86 N/m and 345102±10 Hz, respectively. The sharp peak at t=20 min was the noise signal due to the transient impact of the external environment.

3.1.2 Volume change of cross-linked PS particle in toluene vapor

During swelling, the mechanical properties of PS sphere may change, such as the hardness and density. To investigate the density change of PS sphere during swelling, the volume change must be measured in addition to the mass change. To measure the change in volume during swelling, the diameter of a selected PS sphere was measured in N_2 [Fig. 34a], saturated toluene vapor [Fig. 34b] and N_2 again [Fig. 34c] using a home built optical setup, which is described in more detail in chapter 5.1.2. In the beginning, the fluid cell was exposed to pure N_2 gas for 1 minute. In N_2 we determined a diameter of 32.1±1.0 μm, which corresponds to a volume of 17310±1669 μm^3 [Fig. 35]. The distance between two blue lines on the left part or that on the right part define the error of the diameter calculation, which is determined to be 6 pixels, namely 1.01 μm. The volume of this PS sphere varies upon exposure to toluene vapor [Fig. 36]. At t=1 min the cell was flooded with saturated toluene vapor. Instantly the volume of the PS sphere increased. After 15s, a constant diameter of 38.7±0.7 μm was obtained, which corresponds to a volume of 30333±2413 μm^3 and a relative volume increase (RVI) of 175.2%±13.9%. The swelling part was also fitted by Eq. (3.3) and k of 0.044±0.004 s^{-1} was obtained. It is different from the k value of mass measurement (0.05-0.06 s^{-1}). It is attributed to the less data points during swelling for volume measurement, which results in the non-perfect fitting. At t=6 min the saturated toluene vapor was replaced with pure N_2, resulting in a volume decrease. In the beginning, a rapid decrease of RVI (175% to 120% in 4 s) was observed, which is followed by a slow decrease (120% to 100% in 20 s). The RVI returned to its starting value 100%±9.6% in 20 s. The large error in the measurement is attributed to the poor resolution of the images. Ideally, the smallest error in the image would be 643 nm (calculated by 540 nm/2/0.42, where 540 nm the average wavelength of the white light, 0.42 the numerical aperture of the objective). In our experiment, the error is slightly larger than the ideal value, which is attributed to the difficulty in the adjustment of the focal plane on the equator of the particle and the poor contrast in the image.

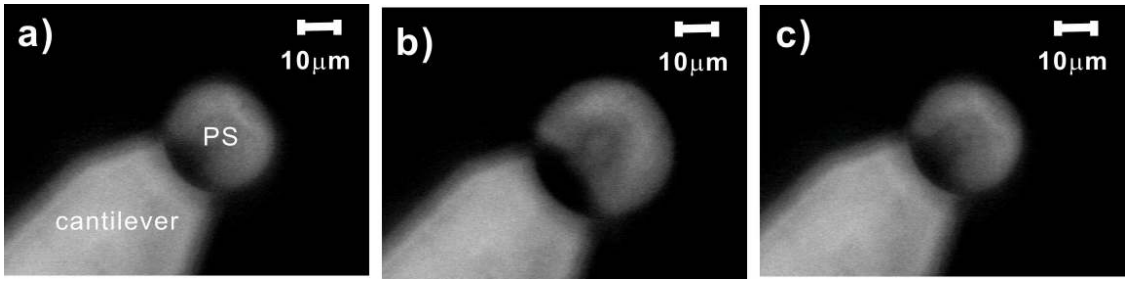

Fig. 34. Optical image of a PS sphere (a) in N_2 (b) in saturated toluene vapor and (c) in N_2 again. The resolution of the image is 640×480 pixel. One pixel in the image corresponds to 169 nm.

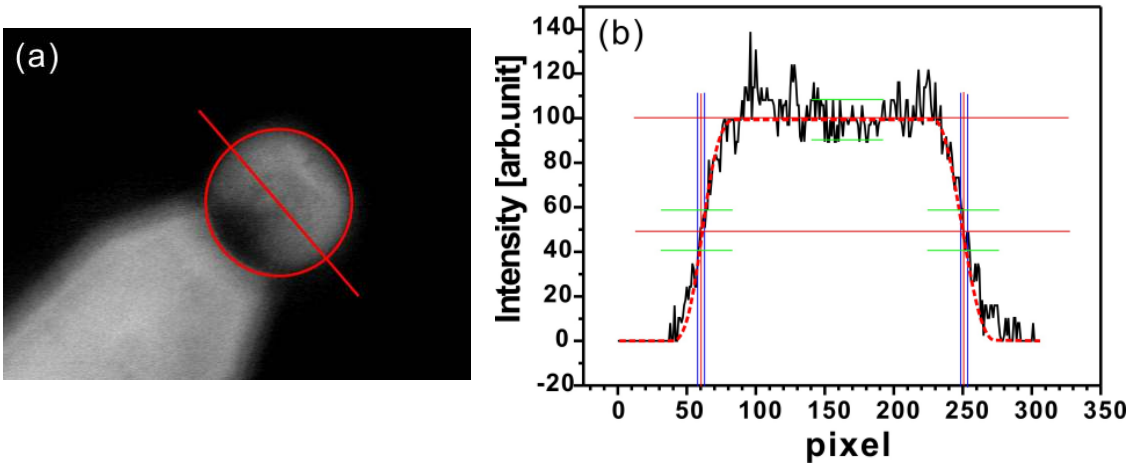

Fig. 35. Illustration of the calculation of PS diameter. (a) A red circle was fitted to the outline of the PS particle with a red line through the center of the circle. (b) The profile of the intensity along the red line in (a). Two red horizontal lines at intensity of 100 and 50 define the maximum and half maximum intensity, respectively. Two red vertical lines define the width at half maximum intensity, which is the PS diameter (190 pixels). Two green horizontal lines at intensity of 110 and 90 define the error of the intensity. The dashed red curve is the smooth of the intensity profile. The intersections of green lines (at intensity of 60 and 40) with smooth curve define the error of the diameter in pixel, which is indicated by vertical blue lines. By the calibration of 0.169 nm/pixel, the PS diameter is calculated to be 32.1±1.0 μm.

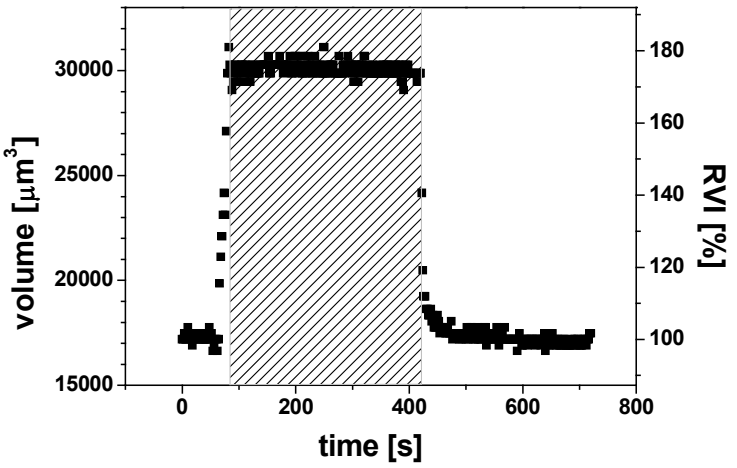

Fig. 36. Volume and relative volume increase (RVI) of the MCS end-loaded with a PS sphere (diameter of 32.1±1.0 μm) upon exposure to N_2 and saturated toluene in N_2 gas flow (hatched areas). One image was recorded every 2 s. The corresponding time interval between each calculated volume data was 2 s.

3.1.3 Mass and volume change of cross-linked PS particle in toluene vapor

To investigate the density change during PS swelling, the change in mass and volume were measured simultaneously [Fig. 37]. In the beginning, the fluid cell was exposed to pure N_2 gas for 5 minute. The optical measurement started at t=4 min. In N_2 the mass density of PS is assumed to be 1.05 g/cm^3, which is given in the datasheet provided together with the samples by the Duke Scientific Corporation. At t=5 min the cell was flooded with saturated toluene vapor. Instantly the mass and volume of the PS sphere increased. After 15s, a constant relative mass increase (RMI) of 198±3% was obtained. While the relative volume increase (RVI) was 203±33% and fluctuated between 170%±33% and 230%±33%. The mass density of 0.98 g/cm^3 is calculated (RMI of 198% divided by RVI of 203%, the quotient multiplies 1.05 g/cm^3). Since the density of toluene is 0.87 g/cm^3, we expect that the mass density of the swollen PS sphere is between 0.87 and 1.05 g/cm^3. The calculated density is in agreement with our expectation. At t=15 min the saturated toluene vapor was replaced with pure N_2, resulting in a mass and volume

decrease. After 5 minutes, RMI returned to 110% while RVI returned to its starting value 100%±30% and fluctuated between 90%±30% and 110%±30%. The fitted *k* using Eq. (3.3) for the swelling curve of mass and volume is 0.051±0.002 s^{-1} and 0.049±0.012 s^{-1}, respectively.

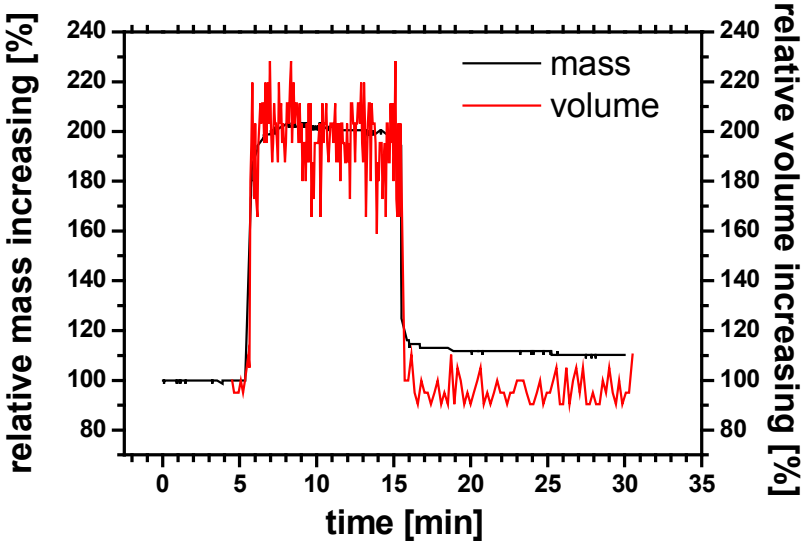

Fig. 37. Relative mass/volume increase of the MCS end-loaded with a PS sphere (diameter of 10.8±1.0 µm) upon exposure to N_2 and saturated toluene in N_2 gas flow. The data were recorded every 0.3 s for mass measurement and 2 s for volume measurement.

3.1.4 Size dependent effects

To check potential size dependent effects, we investigated PS spheres with different diameters of 7±1, 10±1, and 16±1 µm. For these PS spheres, we found RMIs at the saturation states of 179%±1%, 188%±3%, and 178%±1%, respectively. From this we conclude that the RMI is independent from the size of the spheres and that the PS spheres swell homogeneously. The small discrepancy for the PS spheres with diameter around 10 µm is attributed to differences in cross-link densities (4-8 mol %), even though selected from the same batch.

3.1.5 UV cross-linking effects

Photoirradiation in the presence of oxygen can induce degradation[87] of PS, which on the microscopic level is characterized by macromolecular chain splitting, creation of low mass fragments, production of free radicals, oxidation, and cross-linking.[56] Consequently, macroscopic properties of the polymer, such as mechanical strength, color, electrical conductivity, and swelling are affected. Control of the latter would allow tailoring the amount of encapsulation and release of substances. Therefore, we exposed a selected PS sphere (diameter of 13±1 μm) to ultraviolet (UV) light. Initially the chemically cross-linked PS sphere was irradiated for different exposure times from all sides by UV light under ambient conditions to induce additional cross-linking. The UV source, a pencil-style lamp (wavelength of 254 nm, LOT-Oriel GmbH, Darmstadt, Germany), was placed at a distance of 0.5 cm to the PS sphere resulting in a radiant intensity of 2.1 mW/cm^2. After each UV irradiation step, the sphere was exposed to saturated toluene vapor and after that to N_2 to measure the RMI. The PS sphere exhibits a significant change in response to the saturated toluene vapor. The RMI for the saturated swollen sphere decreases with increasing exposure time to UV light [Fig. 38].

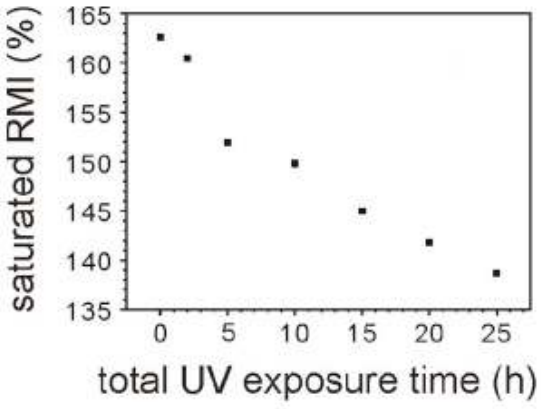

Fig. 38. Relative mass increase at saturation of swelling depending on the total UV exposure time.

For an UV exposure time of 10 h, the swelling-deswelling cycles were repeated twice [Fig. 39]. The RMI at the saturation state is the same for both cycles (148%±1.6%). However, the swelling takes approximately six times longer in the first cycle compared to

all subsequent ones. Two cycles are also fitted by Eq. (3.3). We obtained that k of the first and second cycle is 0.0037±0.00002 s^{-1} and 0.022±0.001 s^{-1}, respectively.

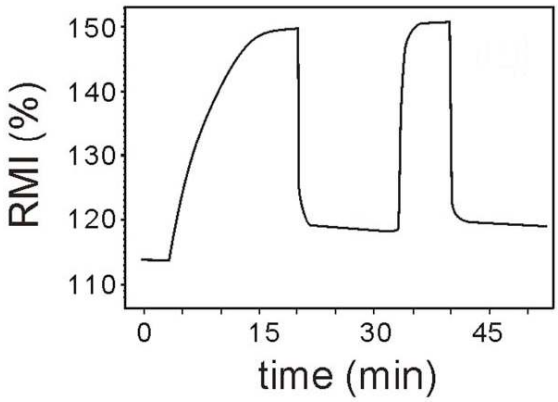

Fig. 39. First and second cycle of the swelling and deswelling behaviors after exposure to UV for 10 h.

The k of the first cycle is smaller than that of the second cycle, which means the diffusion of toluene molecules into the PS particle is slower for the first cycle than the second cycle. A possible reason is that during UV exposure, the sphere is cross-linked and/or oxidized resulting in a less swellable shell through which the toluene molecules must penetrate [Fig. 40]. During swelling of the PS sphere upon the first exposure to saturated toluene vapor this shell is disrupted irreversibly. In the second swelling cycle this leads to the observed faster swelling process. But the k of second cycle (0.02 s^{-1}) is smaller than the value in chapter 3.1.1 (0.05-0.06 s^{-1}), which is attributed to the increasing cross-linking induced by UV irradiation.

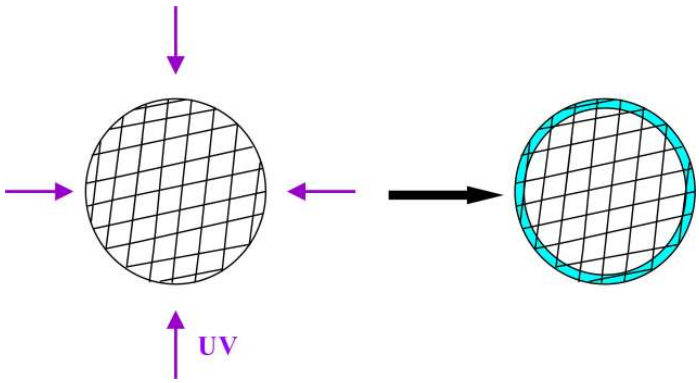

Fig. 40. Schematic drawing of cross-linked PS sphere and hard PS shell (blue) induced by UV exposure. The UV exposure was conducted from top, bottom, left side and right side sequently for the same time.

To confirm this hypothesis, we exposed a non-cross-linked sphere (diameter of 11 μm, Bangs Laboratory, Fishers, IN) to UV light only from the top side for 11 h and imaged the PS sphere after exposure to saturated toluene vapor [Fig. 41a]. An open egg-type structure was observed: The shape of the PS sphere at its top side, which was exposed to UV light, is shape persistent [Fig. 41a I]. Vis-à-vis a PS puddle formed by the flow of PS out from the sphere [Fig. 41a II]. For reference, a non-UV treated PS was exposed to saturated toluene vapor only. In this case no shape persistent structure could be observed [Fig. 41b]. The PS becomes liquid like and spreads over the cantilever.

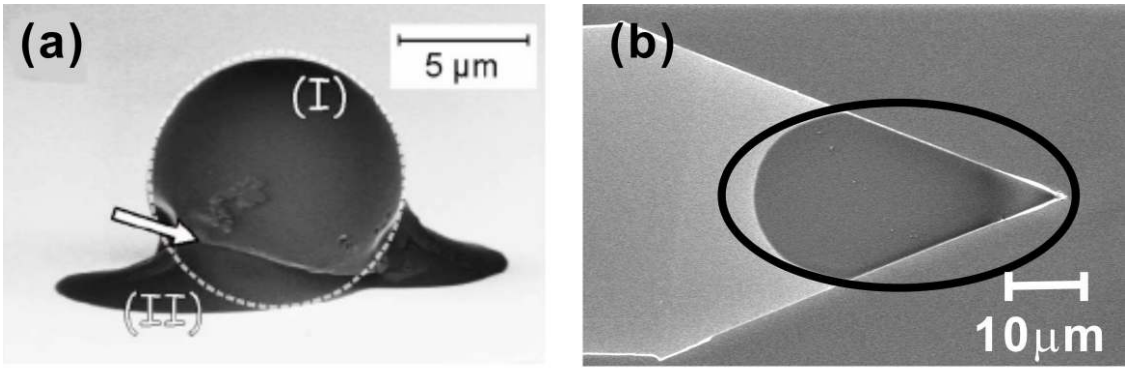

Fig. 41. Scanning electron micrograph of (a) a PS sphere after 11 h of UV light and 15 min of saturated toluene vapor exposure. The circle indicates the original shape of the sphere. The arrow indicates the boundary of the hard shell to non-cross-linked PS. (b) a non-cross-linked PS sphere on the cantilever after exposure to toluene for 10 minutes. The black circle shows the PS becomes liquid like after toluene exposure.

This observation directly confirms that the outer shell indeed was cross-linked by the UV light. Based on this observation, we explored a new method to fabricate PS nanoarrays, which will be described in the following **chapter 4**.

3. 2 Investigation of swelling of PS with different cross-linking densities using confocal microscopy

Study of swelling of PS particle by MCS technique only provides the information of mass uptake of PS particle and diffusion dynamics of toluene molecules in the PS particle. But there is also other information interesting to be known. For example, how does the surface of PS particle look before and after UV irradiation? How would absorbed molecules distribute in the PS particle? The answers can be provided by confocal laser scanning microscopy (CLSM). In addition, fluorescence correlation spectroscopy (FCS) can be used to measure the diffusion dynamics of dye molecules in the PS particle, which reveals the interesting information of PS during swelling.

3.2.1 Chemical cross-linking effects

To investigate the influence of chemical cross-linking density on the diffusion behavior of small dye molecules in the PS sphere, two PS spheres with chemical cross-linking density of 4-8% and 20% were exposed to toluene liquid. FCS was performed and diffusion coefficients of the dye molecules were calculated. Perylene dye (PDI) was used as a tracer. First we measured the fluorescence intensity distribution around the PS sphere, which is proportional to the PDI concentration. For the 4-8% chemically cross-linked PS sphere, the average fluorescence intensity inside the sphere was similar to that outside the sphere [Fig. 42a]. This indicates that dye molecules diffuse inside the PS sphere. The fluorescence intensity on the surface of the sphere was larger than that inside the sphere. It indicates that part of the dye molecules tend to stay at the surface. The diffusion time τ_D of dye molecules was measured to be 25±1.3 μs outside the PS particle and 490±25 μs inside the particle. Since the diffusion coefficient is inversely proportional to the diffusion time (Eq. 5.12), the diffusion coefficient inside the sphere is calculated to be 20 smaller than that outside the particle. For the 20% chemically cross-linked PS sphere [Fig. 42b], the fluorescence intensity inside the sphere was much smaller than that outside the

sphere. Furthermore, no correlation was observed inside the PS sphere. This indicates that the dye molecules practically do not enter the sphere in this case.

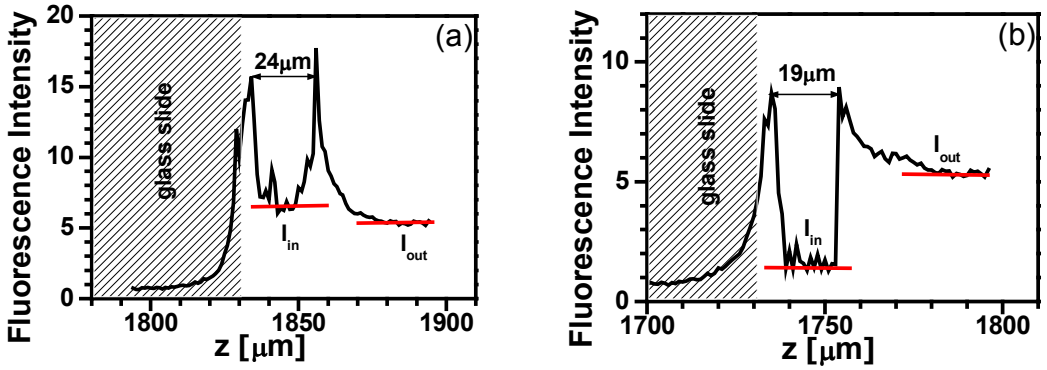

Fig. 42. Fluorescence intensity (arbitrary units) in PS sphere (a) diameter of 24 µm, 4-8% chemically cross-linked (b) diameter of 19 µm, 20% chemically cross-linked. I_{in} and I_{out} stand for the fluorescence intensity inside the sphere and outside the sphere (i.e. in toluene liquid), respectively. Grey shadow indicates the glass slide, where PS sphere was placed. Z is the scan direction of the objective. The red lines are the plateau of the I_{in} and I_{out}.

3.2.2 UV cross-linking effects using fluorescence imaging

To study the influence of UV light irradiation on the PS particle, chemically cross-linked and additional UV cross-linked PS particles were imaged by CLSM. At first we exposed a 4-8% chemically cross-linked PS sphere to toluene liquid. The sphere did not show any fluorescence and they could only be observed in transmission or reflection mode. Then fluorescence images were obtained by using perylene dye in toluene liquid as a tracer [Fig. 43a]. The dye molecules were detected inside the PS sphere, which confirms the diffusion of PDI molecules inside the PS sphere. The highest intensity is obtained around the PS-toluene interface. It indicates that part of the dye molecules tend to stay at the surface of the PS sphere, which is possibly attributed to the oxidized shell at the surface of the PS sphere. It is consistent with the conclusion from chapter 3.2.1.

Next, 4-8% chemically cross-linked PS spheres were exposed to UV light from top for 5h. After UV irradiation, fluorescence image shows that PS sphere is fluorescent in

toluene without dye molecules as a tracer [Fig. 43b]. It indicates that UV irradiation creates fluorescent species in the PS sphere. The image also shows that cracks (dark ribbons in the sphere) were formed on the surface of the PS sphere. It confirms that UV exposure induces the additional cross-linked and/or oxidized shell on the PS sphere, which can be broken by the swelling of the internal part of the PS sphere upon exposure to toluene. The width and length of the cracks are not consistent, which is attributed to the randomly broken surfaces.

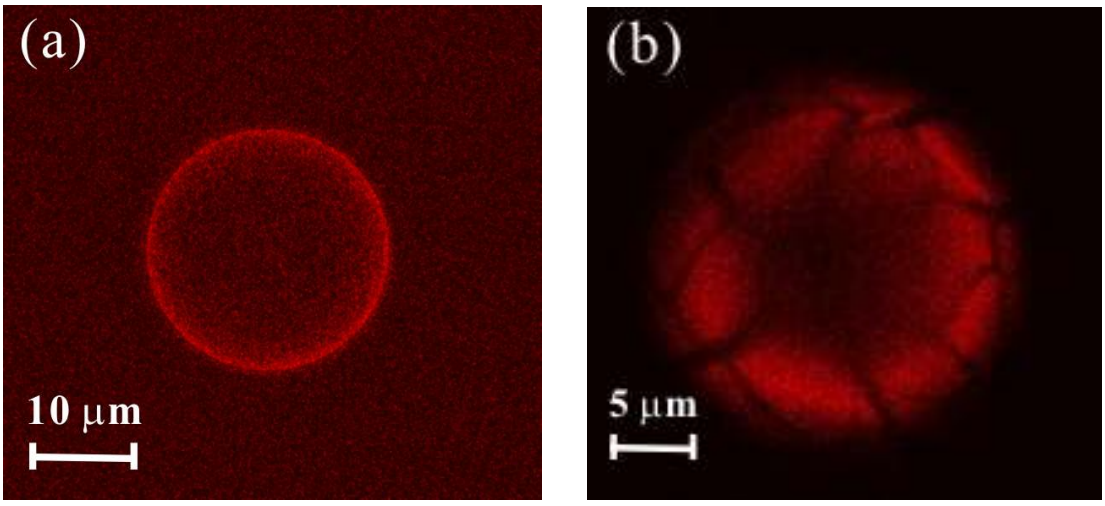

Fig. 43. CLSM images of PS sphere in toluene. (a) diameter of 24 μm, 4%-8% chemically cross-linked. Perylene dye (PDI) was used as a tracer. (b) diameter of 20 μm, 4%-8% chemically cross-linked, additional cross-linked by UV light from top for 5h. There is no tracer in this case.

3.2.3 UV cross-linking effects using fluorescence correlation technique

To quantitatively study the influence of UV light irradiation on the PS particle, the diffusion time of terylene dye molecules in chemically cross-linked and additional UV cross-linked PS particle was measured by FCS [Fig. 44]. Here we used terylene dye molecules as a tracer (maximal absorption wavelength λ_{max} larger than 650nm) because PS exhibits similar fluorescence as perylene dye after UV irradiation (absorption

wavelength similar to that of the perylene dye of 300-510 nm), as shown in Fig. 43b. The normalized auto-correlation function $[G(\tau)-1]/[G(0)-1]$ was plotted in Fig. 44. At first we exposed a 4-8% chemically cross-linked PS sphere to toluene liquid. The diffusion time τ_{D1} of dye molecules in pure toluene was measured to be 36±1.8 μs. The diffusion time τ_{D2} of dye molecules in the center of the chemically 4-8% cross-linked PS particle is measured to be 1810±90 μs. In addition 4-8% chemically cross-linked PS spheres were exposed to UV light for 2h. The diffusion time τ_{D3} of dye molecules in the center of the PS particle is measured to be 1900±95 μs. This indicates that additional cross-linking and/or oxidizing only happen on the shell on the PS sphere and irradiation induced by UV has no influence on the diffusion of dye molecules inside the particle. We expect that with longer UV irradiation, the cross-linked and/or oxidized shell will be thicker (i.e. increasing cross-linking density of PS sphere).

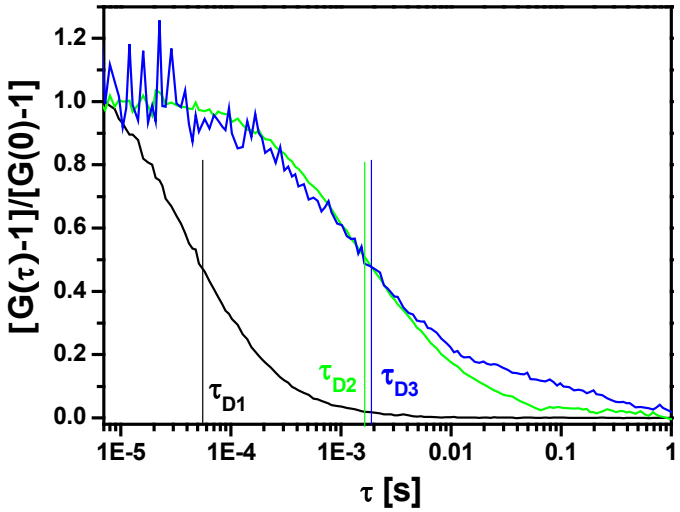

Fig. 44. Normalized correlation curves of diffusing terylene dye in pure toluene (black curve), in chemically 4-8% cross-linked PS particle (green curve), and in the PS particle with further 2 hours exposure to UV (blue curve). Three vertical lines indicate the respective diffusion times τ_{D1} of 36±1.8 μs, τ_{D2} of 1810±91 μs and τ_{D3} of 1900±95 μs.

Chapter 4

Fabrication of PS sphere array with donut structure

From the experiment of PS swelling, we observed that the non cross-linked PS sphere could be locally cross-linked by the UV light [Fig. 41a]. Based on this observation, fabrication of PS sphere arrays with bowl-like structure was anticipated and performed [Fig. 10b].

Spin coating method was used to coat a single layer of PS spheres on the substrate.[88,89] The parameters used in spin coating are listed in Table 4:

Diameter (μm)	Concentration (weight % solids)	Spinning velocity (rpm)	Spinning time (min)
0.5	10	700	3
1	10	1000	3
2	10	300	5

Table 4. Parameters used in spin coating to fabricate a monolayer of PS spheres.

The forces driving the particles gathering into two-dimensional (2D) array are mainly the hydrodynamic force due to water influx and lateral capillary force. The faster spinning velocity was used for PS spheres with diameter of 1 μm than for that of 0.5 μm. The possible reason is that for the larger particle, the higher friction force is required to roll the particle into close packed formation. Therefore the faster spinning velocity is used to produce the higher friction force. While the spinning velocity is lower for the PS spheres with diameter of 2 μm. This is attributed to the larger particle having higher mass. Because all the three solutions have the same weight percentage of particles, the higher

the mass, the less the particle numbers. Therefore the coverage density of spheres on the substrate is lower for the larger particles. To form a close packed monolayer, the larger particles need to migrate long distance to gather together with the help of water influx. Using slower spinning velocity, the water evaporates slower, which provides more contribution to the assembling of the spheres. As a consequence, the spinning time is longer to achieve complete evaporation of water using slow spinning time.

The fabricated film might rupture using too fast spinning velocity, which is caused by high hydrodynamic friction force of water influx during fast evaporation.[90] While using too slow spinning velocity, the film might comprise multilayers, which is attributed to low friction and centrifugal force to spread the aggregation of the spheres.

The centimeter-sized monolayer PS arrays obtained from PS particles exhibit iridescent coloring when the sample was slowly tilted under the bright light. The boundaries between differently oriented domains and the defects in the film were observed [Fig. 45].

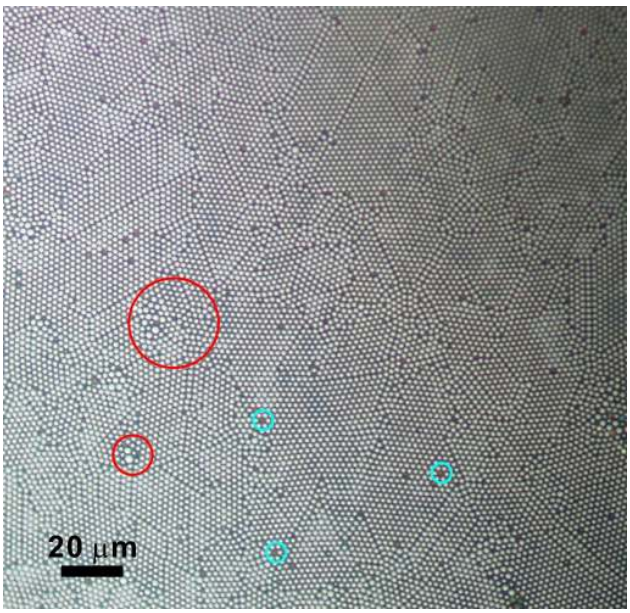

Fig. 45. Differential interference contrast (DIC) images of close-packed PS particles with diameter of 2 μm (200×200 μm^2). The blue circles indicate the defects and the red circles indicate the particles of different sizes which result in the differently oriented domains.

4.1 Monolayer of PS spheres

PS particles with diameter of 1 μm were spin coated to form a monolayer on the quartz glass substrate [Fig. 46a]. In this monolayer, some small particles (in the red circle) were observed, which is attributed to the non perfect monodispersity of the commercial solution. Most of the particles are close packed with hexagonal configuration, but some defects (in the blue circle) were also observed. It is attributed to the locally fast evaporation of water, which leads to the rupturing of the film during the spin coating. The array of PS particles with diameter of 500 nm was produced in the same way as mentioned above [Fig. 46b] and most of the particles were perfectly close packed with a hexagonal configuration.

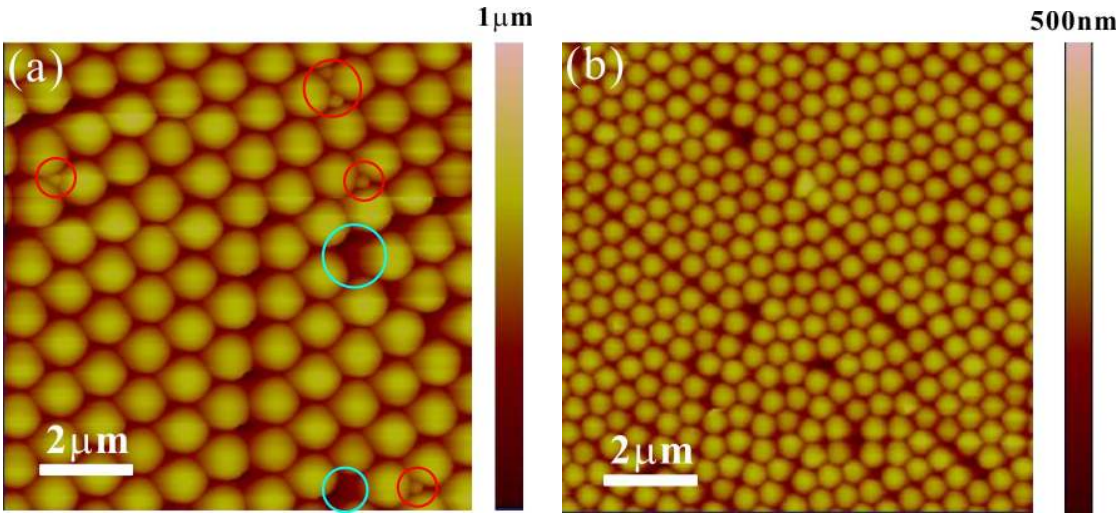

Fig. 46. AFM height images of the array of PS particles (10×10 μm^2). (a) diameter of 1 μm and Z range of 1 μm. (b) diameter of 500 nm and Z range of 500 nm.

4.2 Arrays of PS spheres with donut structure

4.2.1 The effect of UV irradiation on PS films

To verify the cross-linking effect on PS by UV irradiation, the UV absorption measurements were performed on a PS film [Fig. 47a]. The film was produced by dissolving PS (Mw: 97619.90 g/mol) in toluene and a drop of this solution was spin coated to form a homogeneous layer with the thickness of 120 nm. The spin coated PS film exhibits UV absorption at wavelength of 254 nm.[91] The absorbance at wavelength of 254 nm was plotted versus accumulative UV exposure time [Fig. 47b]. The curve shows that for longer UV exposure time, the absorbance of the film is increased. The dependence is not linear. After 5h exposure, the absorbance reaches a plateau. The results verify that UV light is absorbed by PS and the absorbance reaches the saturation after 5h exposure.

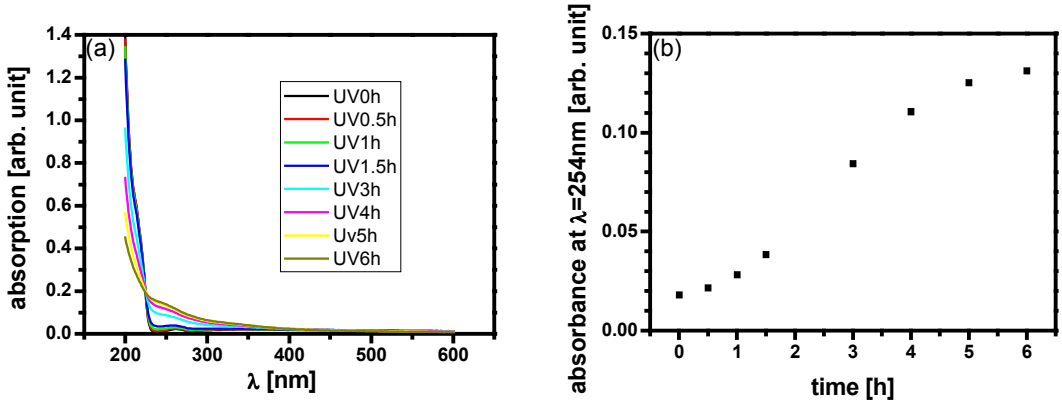

Fig. 47. (a) UV absorption spectra of the PS film. After each UV exposure time, the absorbance of UV on the PS film was measured. (b) The absorbance at wavelength of 254 nm versus accumulative UV exposure time.

4.2.2 Arrays of PS spheres upon UV and toluene treatment

PS particles with diameter of 2 μm were spin coated to form a monolayer on the quartz glass substrate. Then the sample was irradiated by the UV light (wavelength of 254 nm, intensity of 0.658 mW/mm^2) from **bottom** for 1h. After that, it was exposed to toluene liquid. A bowl-like structure with dent in the middle was observed [Fig. 48a]. The calculation of half width *w* at half maximum height was illustrated in Fig. 48a. The wall width *w*/2 of each structure was calculated. The average *w*/2 is 355±82 nm, which is approximately one third of the radius of the original sphere.

To investigate whether the direction of UV irradiation has an effect on the fabrication of donut structure, arrays of PS spheres with diameter of 2 μm was exposed to UV from **top** for 20 min and then toluene liquid was performed. The structure with dent in the middle of each sphere was also formed [Fig. 48b]. It indicates that the direction of UV exposure does not play a role on the structure that formed. The average *w*/2 is calculated to be 271±39 nm.

To check whether UV irradiation plays a role on the fabricated structure, arrays of PS was directly washed by toluene liquid without UV exposure [Fig. 48c]. The donut structure was also observed. This indicates that UV irradiation from bottom for 1h or from top for 20 minutes has no influence in the fabrication of such structure. The average *w*/2 is calculated to be 326±38 nm. The collapse of the structure at the right boundary on the substrate was observed (red circles). It is attributed to the toluene liquid wash, while the structure far from the boundary is supported each other by adjacent ones.

The wall widths *w*/2 of three samples are similar (355±82, 271±39, 326±38 nm), which verifies that UV irradiation for short time has no influence in the fabricated structure.

The home synthesized PS spheres (diameter of 1 μm, synthesized by Maria D' Acunzi in my group) without UV irradiation were completely dissolved after toluene treatment. Donut structure was not observed in this case.

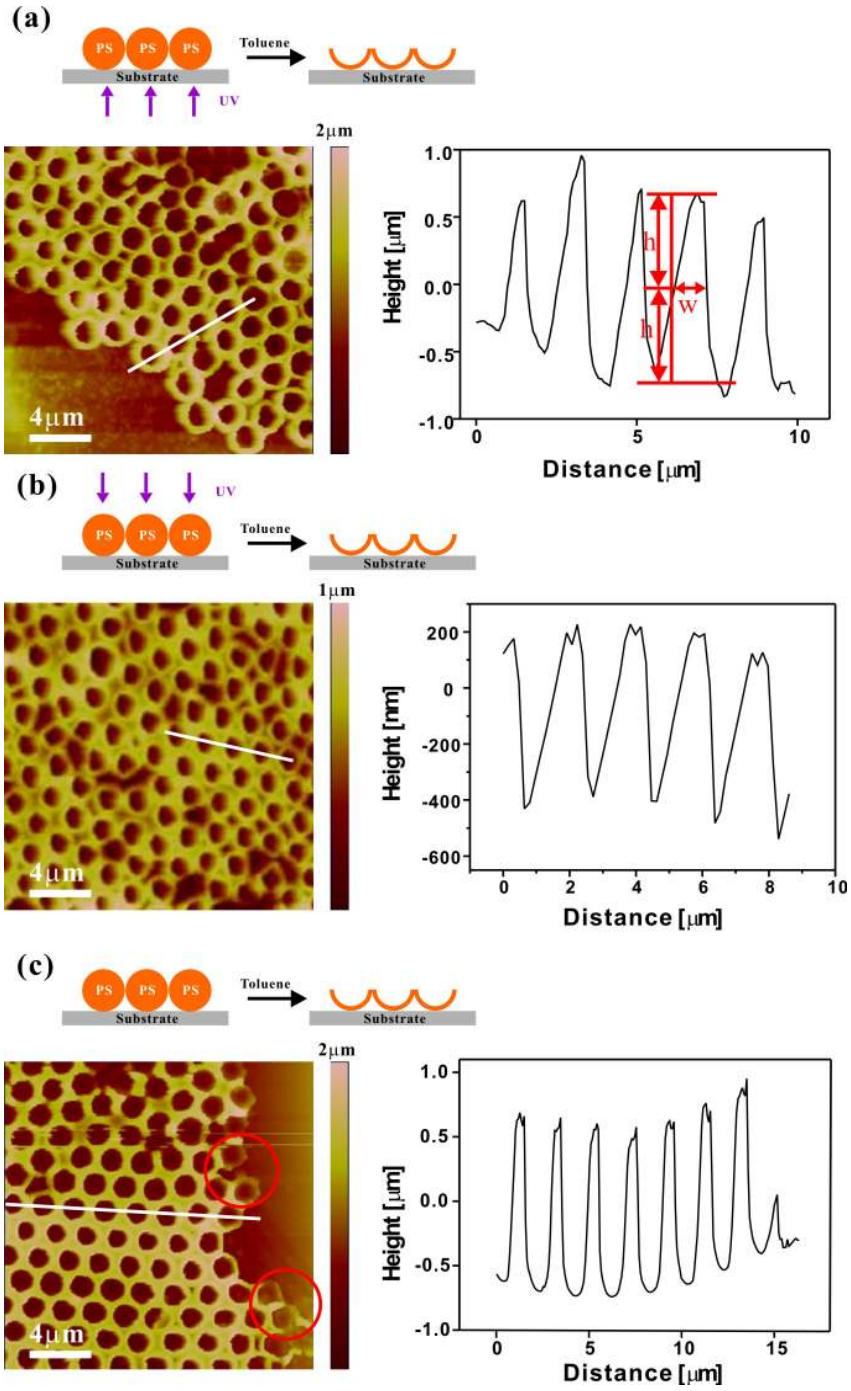

Fig. 48. (Left) Schematic drawing of the experimental procedure and corresponding AFM height images of PS particles with diameter of 2 μm after UV and toluene treatment (20×20 μm^2). (a) UV from **bottom** for 1h and then toluene liquid (b) UV from **top** for 20 min and then toluene liquid (c) toluene liquid without UV irradiation (Right) Cross section analysis along the white line in the corresponding left AFM image.

4.2.3 The effect of UV irradiation time on arrays of PS spheres

Since the above measurements were performed with UV exposure no longer than 1h, it may not be sufficient to cross-link PS. Therefore arrays of PS spheres with diameter of 1 μm was exposed to UV from bottom for 5h. Then it was washed by toluene liquid. The results show that the PS spheres remain spherical shape even after toluene treatment [Fig. 49a]. It means that the entire PS spheres were completely cross-linked by UV irradiation. The three red horizontal lines in the cross section analysis (indicated by blue line) represent three positions. The lowest line indicates the height of the substrate. The line in the middle indicates the height of the junctures of the contiguous PS spheres. The highest line indicates the height of the top of the PS spheres. The distance between the lowest line and middle line (550 nm) is larger than that between the middle line and the highest line (400 nm) and the distance between the substrate and the top of the spheres (950 nm) is 50 nm smaller than the diameter of the sphere (1 μm), which means the top hemisphere (which is not directly exposed to UV) slightly melts after toluene treatment [Fig. 50]. There are gaps between contiguous PS spheres (cross section analysis indicated by green line in Fig. 49), which is attributed to the shrink of the swollen PS sphere after drying in air [Fig. 50]. To verify the effect of long time UV irradiation on PS spheres with different diameters, arrays of PS spheres with diameter of 2 μm was exposed to UV from bottom for 12h. Then it was washed by toluene liquid. The results also verify that PS spheres were completely cross-linked by UV irradiation [Fig. 49b]. The slightly melting of the top hemisphere and gaps between contiguous PS spheres were also observed.

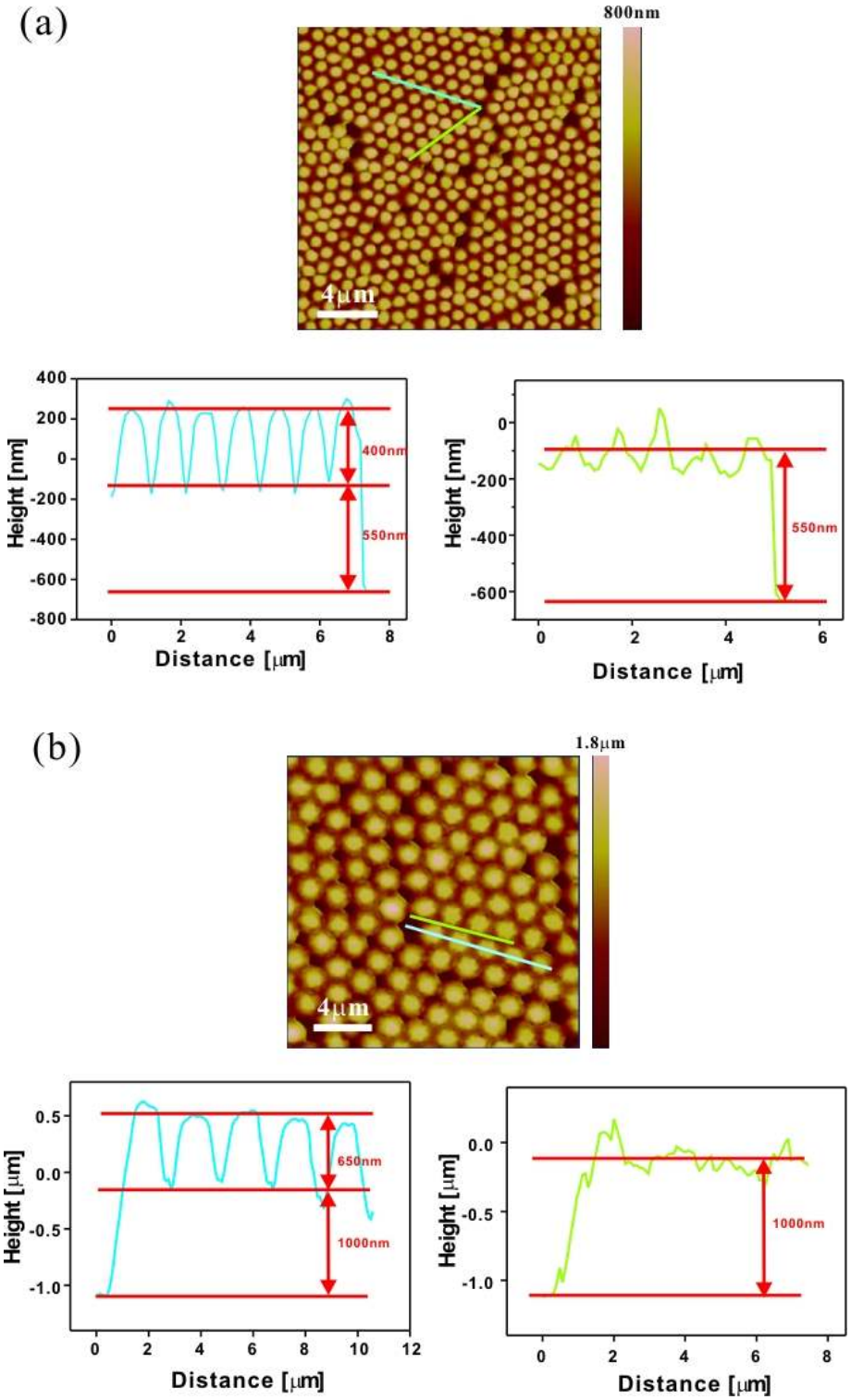

Fig. 49. AFM height image of PS particles (20×20 μm^2) and cross section analysis along the blue and green lines in the top AFM image, respectively. (a) diameter of 1 μm and Z range of 800 nm (b) diameter of 2 μm and Z range of 1.8 μm.

Fig. 50. Schematic drawing of toluene treatment of PS spheres cross-linked by UV for long time.

But why did we observe the donut structure when the UV irradiation is not long enough or absent? The possible reason is that there are some poly (styrene sulfonate) (PSS) or poly (acrylic acid) (PAA) chains on the outshell of PS sphere, which are used as stabilizer during the synthesis and physically adsorbed on the PS spheres. After toluene treatment, non completely cross-linked PS spheres were dissolved and washed away. Only the PSS or PAA, which is attached on the substrate and not soluble in toluene, remains on the substrate [Fig. 51].

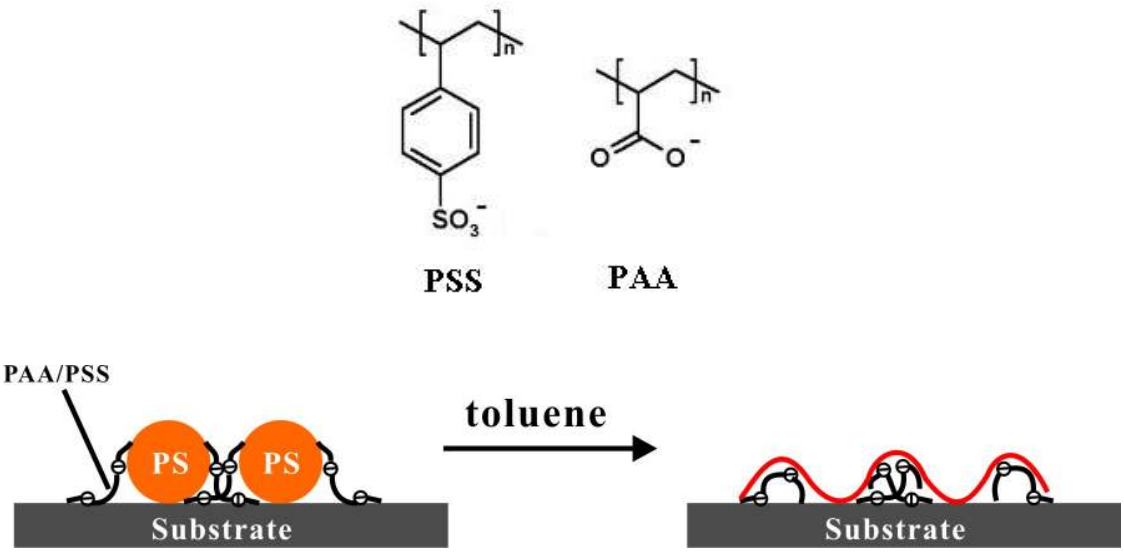

Fig. 51. (Top) Chemical structures of poly (styrene sulfonate) (PSS) and poly (acrylic acid) (PAA). (Bottom) The mechanism of fabrication of PS arrays with donut structure. The red curve is the guide topography of the structure.

Chapter 5

Materials and Methods

In this chapter several methods used in my experiments are introduced: Micromechanical Cantilever Sensor (MCS), Atomic Force Microscopy (AFM), Fluorescence Correlation Spectroscopy (FCS) and white light confocal microscopy. The samples used in the experiments are described in detail. In addition, the sample preparation procedures are summarized.

5.1 Micromechanical cantilever sensor (MCS)

In this section two commercial systems based on MCS are introduced: Veriscan 3000^{TM} and Scentris^{TM}. The Veriscan is developed to perform static bending measurements (results in chapter 2) and the Scentris facilitates the dynamic frequency measurements (results in chapter 3).

5.1.1 Veriscan 3000^{TM}

Veriscan is a sensor system based on MCS. It transduces the recognition of interactions on molecular level into nanomechanical deflections.

The MCS array used in these experiments comprises sixteen identical rectangular silicon micromechanical cantilevers and four reference mirrors grouped into four separate wells [Fig. 52]. The MCS are fabricated from single crystal silicon and are 500 μm long, 150 μm wide, and 1 μm thick (Silex Microsystems, Bruttovagen, Sweden). The upper side of each MCS is coated with a 5 nm Ti/W adhesion layer and 30 nm Au layer. The MCS in each well have a pitch of 250 μm, respectively. The supporting chip is 22 mm long, 5 mm wide and 500 μm thick.

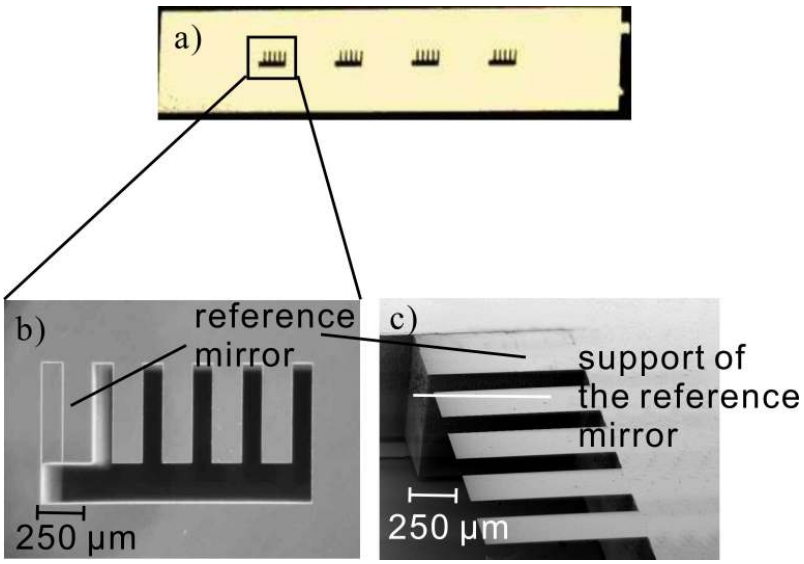

Fig. 52. (a) Optical picture of a MCS array with four wells. (b) Top view and (c) Side view of the scanning electron microscope (SEM) micrograph of a well with four cantilevers and one reference mirror.

The different wells allow an easy, independent and automated functionalization by fluidic flow (detail in chapter 1) without the risk of cross contaminations among different wells. The reference mirror in each well can be used to measure the absolute MCS bending by calculating the difference in the output signals of MCS and reference mirror on position sensitive detector (PSD) [Fig. 53].

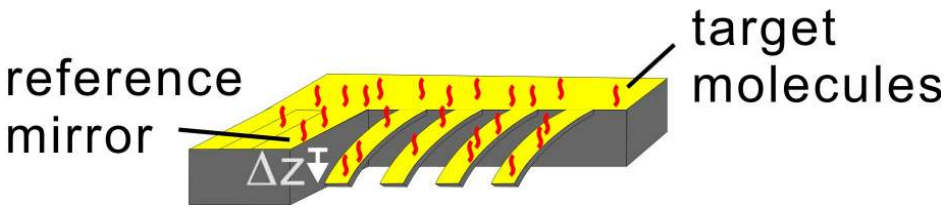

Fig. 53. A schematic drawing of MCS bending induced by the interactions of probe molecules with the sensor coating of MCS. ΔZ is the value of absolute bending between the reference mirror and the MCs within the well. A positive deflection corresponds to an upward bending.

MCS deflections are monitored using a new device (Veriscan3000 by Protiveris Inc. Rockville, MD, USA) that utilizes an optical beam deflection readout employing a linear array of Vertical Cavity Surface Emitting Lasers (VCSELs, wavelength of 760 nm) and

an array of microfocusing lenses [Fig. 54]. The laser spots focused on the cantilever free ends are reflected by the gold surface to a linear PSD. The laser power can be adjusted individually for each VCSEL to obtain a sufficient intensity signal at the PSD. It is necessary for obtaining the output signal from PSD without noise and interference caused by other lights. The PSD ($20\times20mm^2$ sensing area) position can be adjusted in X-Y with two micrometer screws to achieve an alignment relative to the reflected laser spots. With this design, MCS bending can be measured down to 0.1 nm. The interference on the PSD from the external light can be minimized by housing the whole setup in a closed chamber.

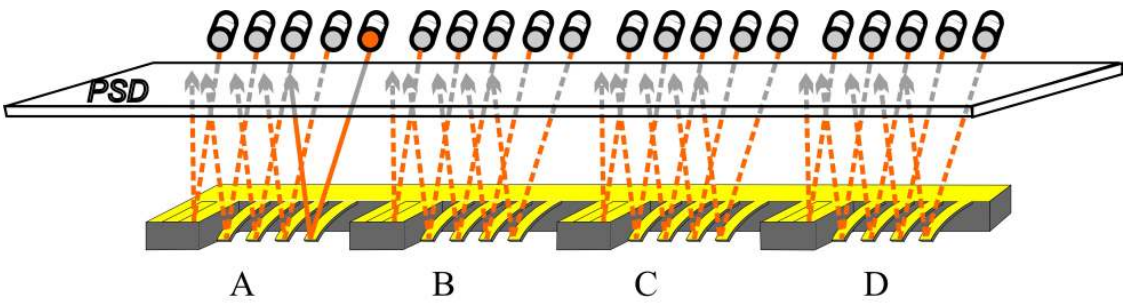

Fig. 54. A schematic drawing of the optical laser beam deflection readout system of the MCS array. Shown are the 4 MCS and the fixed mirror within the 4 wells, respectively. The lasers are time multiplexed and the 5th laser in well A is highlighted exemplarily which means it is switched on.

The MCS deflection Δz is given by Eq. (5.1)

$$\Delta z = \frac{L^2 D}{4yx} \tag{5.1}$$

where L the cantilever length (500 µm), D the displacement of laser spot on PSD, y the distance between MCS and PSD (110.8 mm), x the distance between the position of focused laser on MCS and fixed end of MCS (410 µm). The Veriscan system monitors D during the measurement [Fig. 55].

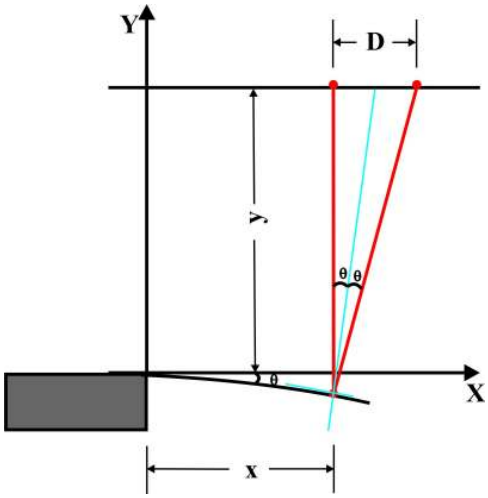

Fig. 55. A sketch of the optical laser beam deflection principle of Veriscan. The red line indicates the laser path.

The cantilever bending is in response to an interaction between molecules in the environment and the cantilever surface (usually either Si or Au). The interactions between probe molecules immobilized onto one side of the cantilever and target molecules present in the environment also result in the cantilever bending. For a rectangular cantilever of length L and thickness t, the deflection Δz can be related to the differential surface stress change between the upper and lower cantilever side ($\Delta\sigma_{up}$-$\Delta\sigma_{down}$) via the approximate relation[92]:

$$\Delta z \cong \frac{3(1-\nu)}{E}\frac{L^2}{t^2}\left(\Delta\sigma_{up} - \Delta\sigma_{down}\right) \tag{5.2}$$

where E and ν are mechanical parameters of the cantilever material, respectively Young's modulus and Poisson's ratio. The above equation is valid only when the surface stress changes uniformly along the length of the cantilever and the absorbed films or coatings are very thin compared with the cantilever thickness.

To deliver the carrier fluid and different sample solutions to the MCS array syringe pump fluidic system are used. Each well is connected to one syringe, respectively which can then be operated in parallel. The system consists of four valves for the carrier fluid, four syringes, four sample valve loops, four injection valves for sample solution and one

cartridge containing the fluid cell with the four wells. When the MCS array is mounted in the fluid cell [Fig. 56a], each well is isolated by a Teflon gasket under the chip and a Teflon mask on top of the chip to prevent the leakage. This enables the introduction of different carrier fluids and sample solutions into the different wells, thus allowing the parallel analysis of various recognition assays. The volume of each well in the fluid cell is 3 µL. The whole cartridge containing the flow-through cell can be heated up to 70 °C.

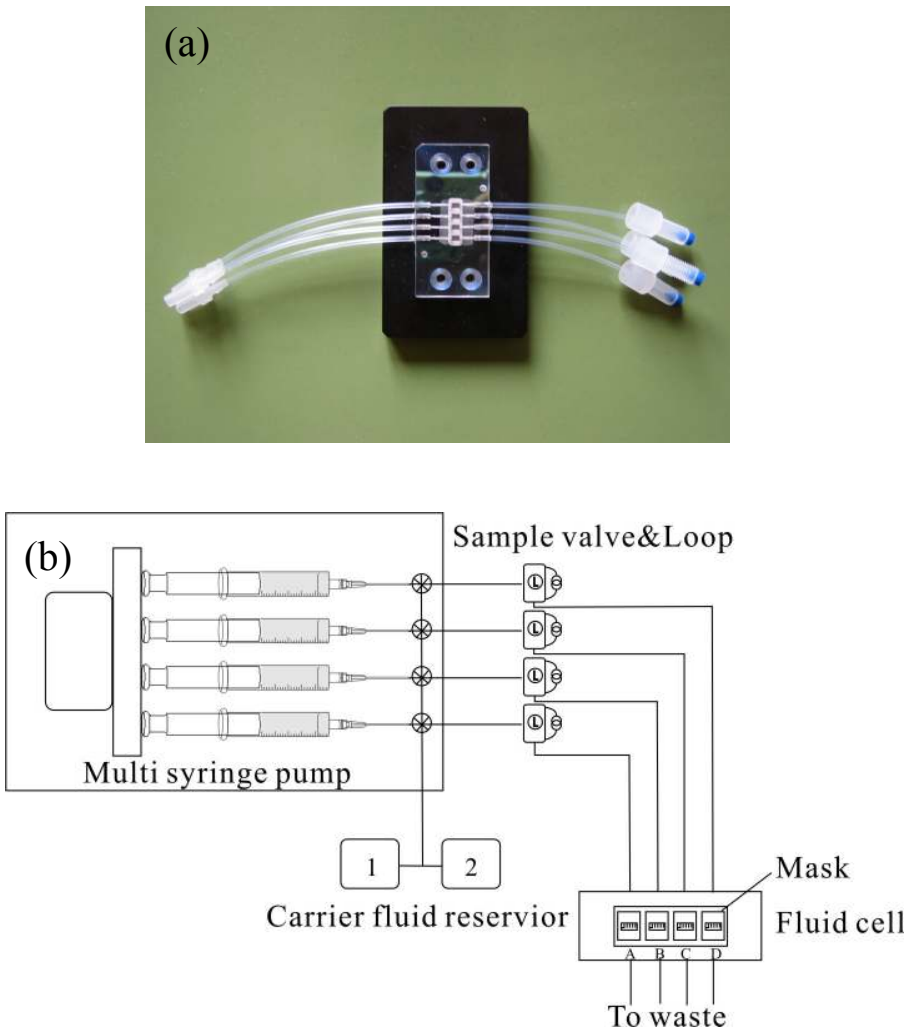

Fig. 56. (a) Optical picture of fluid cell with connecting tubings. (b) A schematic drawing of the fluidic delivery system for the MCS array.

A manual valve allows the interchange between two carrier fluids for each of the four fluidic channels [Fig. 56b]. The reservoirs of the syringes have a volume of 2.5 mL. All the syringes are driven by a single stepper motor controlled via software in order to aspirate and dispense carrier fluid to the four wells simultaneously and at the same speed in the range of 0.5-200 μL/min. Between each syringe and the corresponding well there is a standard sample injection loop made of polyethylether ketone (PEEK). The volume of the sample loop can be selected in a range between 20 to 2000 μL. The loop is connected to a six-port injection valve which is used to interchange the flow stream. With the injection valve at "load" position, sample solution can be loaded into the loop without flowing to the fluid cell and disturbing the carrier fluid flow. After switching the injection valve to "inject" position, the carrier fluid flows through the loaded loop and sample solution is delivered to the fluid cell. Other than the injection loops, all tubing is fluorinated ethylene propylene (FEP).

Samples and sample preparation

DNA molecules were used as a model system for bio-sensing experiment. The specific interaction between two complementary DNA strands, which is called hybridization [Fig. 57], induces the cantilever bending. A double-stranded (ds) DNA having double helix structure is formed through the hybridization of two ss DNA that have complementary base sequences. Each DNA strand has a phosphate group in one end and a hydroxyl group in the other end. The end with a phosphate group is named 5' end because the phosphate group is bonded to the fifth carbon of the sugar ring. The end with a hydroxyl group is named 3' end because the hydroxyl group is bonded to the third carbon of the sugar ring. One of the single-stranded DNA has a spacer with thiol group ($HS\text{-}(CH_2)_6\text{-}$) at the 5' end, which is used to bond to the gold surface of the cantilever through the sulfur gold bond.

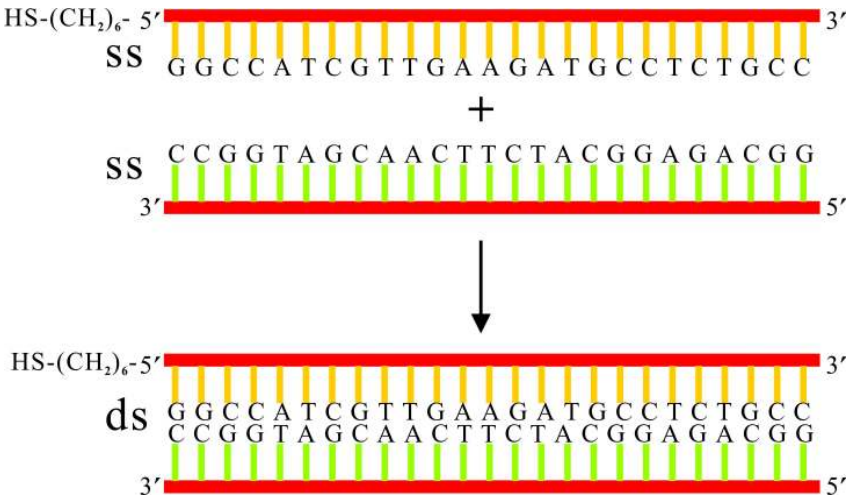

Fig. 57. Schematic drawing of DNA hybridization.

Prior to use each MCS chip was cleaned by highly reactive Ozone generated with a UV lamp (PSD-UV, Novascan Technologies, Inc., IA) for 20 minutes.[93] It operates using a UV light emitting grid (mercury vapor lamp) with the power of 100-120 W. The UV light excites organic molecules and produces highly reactive ozone gas from oxygen that is present within cleaning chamber. The reactive ozone interacts at the molecule level with surface contaminations causing them to degrade. After placing in the fluid cell, the frequency of each cantilever was measured by thermal tuning. The carrier solution was degassed by a vacuum pump to remove the dissolved gas in the solution prior to use. Because the gas in the solution forms the bubbles during the fluid delivery to MCS. The bubbles tend to stay on the MCS, which results in the reflected laser out of PSD and hinders the analyte molecule adsorbed to the MCS. Degassed carrier solution was pumped through the fluid cell until a stable baseline was obtained. Cantilever deflection was measured before, during, and after injection of 200 μL of sample solutions into the flowing stream.

The general DNA hybridization experiments consist of three steps: probe immobilization, thiol blocking and hybridization.

In the immobilization step, ss DNA probes with thiol group (-SH) at the end can be attached to the gold-coated cantilever surface through a sulfur-gold linkage.[44] Such molecules consist of a sulfur group that covalently binds to the Au, and an alkyl spacer with a functional head group. But the thiol group is easily oxidized to form disulfide bond

(S-S), which loses the possibility to bond to gold. In order to ensure the self-assembly of thiolated DNA probes on the gold layer, reducing agent TCEP was added in DNA probe solution for 10 minutes to break the disulfide bond. TCEP reduces disulfide bonds as effectively as dithiothreitol (DTT). But unlike DTT and other thiol containing reducing agents, TCEP does not contain thiols, so it does not have to be removed from solutions.

After the probe molecules were immobilized on the MCS, the main chains of these probe molecules are lying down on the cantilever surface due to the low coverage density in the immobilization step.[94] Because MCH molecules (length of 1.2 nm) are much shorter than probe molecules (length of 10 nm), they can penetrate the probe molecules and settle down on the unoccupied sites, which block the sites for additional adsorption on the cantilever. During this process, the probe molecules were compressed to a standing up phase, which enhances the following hybridization between the probe molecules and the target molecules. It also avoids the following unspecific adsorption of target molecules on gold surface.

5.1.2 Scentris^{TM}

Scentris is a versatile system based on MCS. It transduces the recognition of interactions on molecular level into frequency shifts or nanomechanical deflections.

In our experiments, silicon cantilevers (OMCL-AC160TS, Olympus, Japan) were used with a length of 160 μm, a width of 50 μm, and a thickness of 4.6 μm [Fig. 58].

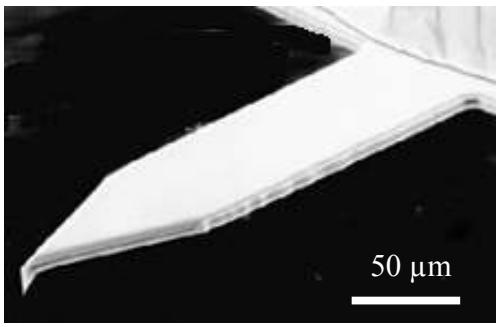

Fig. 58. Scanning electron microscope (SEM) micrograph of a silicon cantilever.[95]

The sharp tip at the end of the cantilever, usually used for imaging of the sample, is not required in our experiments of MCS. The theoretical resonance frequency f_0 of the cantilever is 342 kHz. It is calculated by Eq. (5.3)

$$f_0 = \frac{t}{4\pi l^2}\sqrt{\frac{E}{0.24\rho}} \approx \frac{t}{2\pi l^2}\sqrt{\frac{E}{\rho}} \tag{5.3}$$

with the length l of 132.5 μm (considered as a rectangular cantilever), thickness t of 4.6 μm, material density ρ of 2330 kg/m^3 and the elastic modulus E of 1.5×10^{11} Nm^{-2}.

Nominal spring constant and resonance frequency of the cantilevers are 42 N/m and 300 kHz, respectively. The measured values of the resonance frequency f_0 for the cantilevers we used are in the range of 200-400 kHz. Such large variations are due to the variations in the cantilever geometry.

The spring constant K of the cantilever is calculated by Eq. (5.4)

$$K = 2\pi^3 l^3 w\sqrt{\frac{\rho^3}{E}} f_0{}^3 \tag{5.4}$$

With a measured resonance frequency f_0 in the range of 200-400 Hz and the width w of 50 μm, calculated K is in the range of 16.7-133.9 N/m.

The advantage of using this kind of cantilevers with high frequency on the order of hundred kHz is higher the resonance frequency, larger the frequency shift owing to mass change.

Scentris^{TM} (Veeco, Santa Barbara, CA) is a commercial sensor system based on MCS. In our work, the MCS were operated at dynamic mode to detect the mass changes via frequency shifts. In this way, adsorbed molecules were sensed by measuring the change in the resonance frequency of an oscillating cantilever. The cantilever deflection was determined by the beam deflection principle used in Scanning Probe Microscopy (SPM): a collimated light beam (light emitting diode LED) is focused through a glass window onto the cantilever free end from where it is routed to a position sensitive photodetector (PSD) [Fig. 59a].

The cantilever chip is mounted on a piezoelectric actuator, which is driven by a frequency generator to detect the resonance frequency of the cantilever. The fluid cell [Fig. 59b] contains a ceramic holder and a wire clip to mount and fix the cantilever. The fluid cell also provides inlet and outlet ports to allow exposure of a variety of liquids or

gases to the MCS. The volume of the cell is 30 μL (with cantilever chip inside) – 80 μL (without cantilever chip inside).

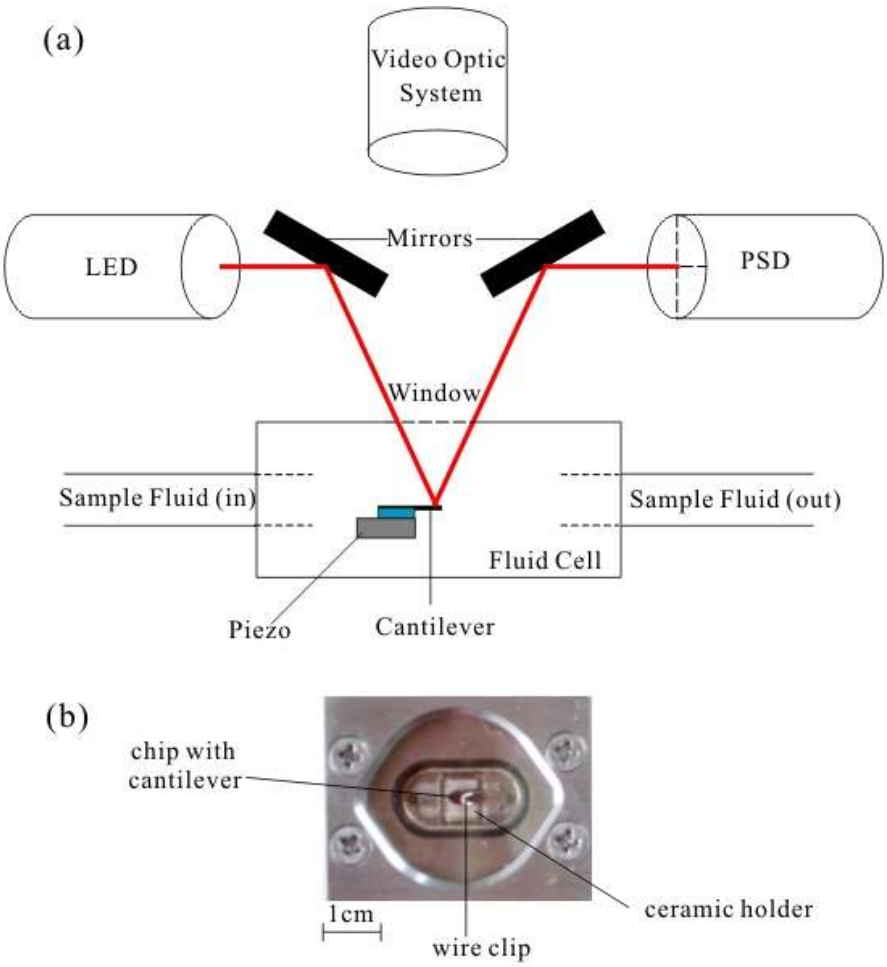

Fig. 59. (a) Schematic drawing of optical path of Scentris™. (b) Top view of the fluid cell of Scentris.

The light source consists of eight light beams from eight superluminous diodes. It can be used for sensing a cantilever array, which contains eight cantilevers on a single chip. In our experiment, we only use one cantilever for each experiment. One light beam is switched on and focused on the cantilever correspondingly.

A video optic system was used for alignment of the light beam to the cantilever. It creates a real-time view that can be observed at any time on the computer monitor. To record the real images of the sample at high magnification, we constructed a 20×

objective (working distance of 20 mm, numerical aperture of 0.42, Plan APO series, Motic, China) connected with a zoom tube (OPTEM zoom 70XL, Qioptiq Imaging Solutions, USA) of magnification from 0.75 × to 5.25 ×. A digital camera (Evolution MP 5.1, Media Cybernetics, MD, USA) with a fast recording rate down to 0.2 s/frame is connected to the objective. An external light source (KL2500 LCD, Schott, Germany) is applied to the optical system to provide sufficient light intensity.

To measure the resonance frequency of a cantilever, a homemade program based on LABVIEW^{TM} was used. The measured resonance frequency peak of a cantilever is shown in Fig. 60. Start frequency, intervals per sweep and frequency increment are three parameters, which can be defined by the user. The frequency range is given by the product of intervals per sweep and frequency increment. In Fig. 60, the frequency range is 20000 Hz given by the product of 100 (intervals per sweep) and 200 Hz (frequency increment). After setting the value of start frequency (315000 Hz) and frequency range (20000 Hz), the end frequency (335000 Hz) is shown in the panel. The resonance frequency (332200 Hz) in the range between 315000 Hz and 335000 Hz is the frequency with maximum amplitude.

The frequency increment gives the frequency resolution of the measurement. In Fig. 60, the frequency resolution is 200 Hz.

The resonance frequency of the cantilever can be recorded continuously at the rate ranging from 0.003 second per data point to 30 seconds per data point with this sensor system. The data-recording rate is inversely proportional to the parameter of intervals per sweep. With intervals per sweep set to 100 the resonance frequency can be determined every 0.3 s.

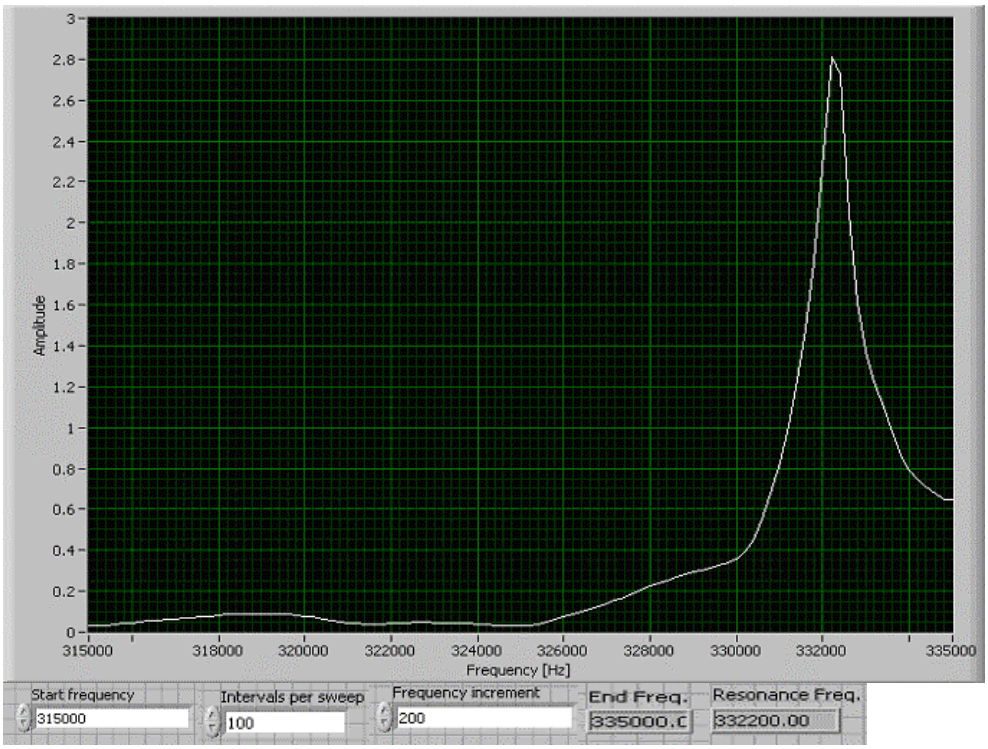

Fig. 60. Resonance frequency peak of a cantilever.

To measure the mass change of a polystyrene sphere upon swelling-deswelling we connected a gas exchange apparatus to the fluid cell (FC) of the MCS setup. The gas flow was controlled with a gas flow meter (FM) (0.5-5 l/h, DK46, KROHNE, Germany), two 3-way valves and a wash bottle containing toluene liquid (99.97%, Fisher Scientific, UK) [Fig. 61]. Nitrogen gas N_2 (99.9997%) served as a carrier gas. It was passed through the gas flow meter, teflon tubings (Outer diameter 1/16 inch, inner diameter 1 mm, Duratec, Germany), wash bottle (selectively) and finally into the fluid cell. The 3-way valves allow switching the gas flow between two different gas compositions. In this work we applied a N_2 flow through path (p1) to control humidity or to remove residue solvent molecules surrounding the cantilever. A saturated solvent gas flow (N_2 + toluene) can also be applied by passing N_2 through path p2. At room temperature (22 °C) we estimated a saturation concentration of 32000 ppm for toluene in N_2. It is calculated by

$$saturation\ concentration(ppm) = \frac{vapor\ pressure(mmHg)}{760(mmHg)} \times 10^6 \qquad (5.\ 5)$$

The vapor pressure p (bar) is calculated by Antoine equation[96,97]:

$$\log_{10} p = A - \frac{B}{C + T} \qquad (5.6)$$

where T the absolute temperature, A, B, and C Antoine coefficients that vary from substance to substance[98,99].

For toluene liquid at room temperature of 295 K, the value of A, B and C is 4.23679, 1426.44 and -45.957. Therefore the vapor pressure p is 0.0322927 bar calculated by Eq. (5.6). With 1 bar = 750 mmHg, the saturation concentration of toluene is 31869 ppm calculated by Eq. (5.5).

For a flow rate of 2 l/h, the vapor in the fluid cell and the headspace in the tubing (total volume: 150 µl) was diluted three times within 1 s. It is calculated below:

$$\frac{150 \times 10^{-6} l}{2\, l/h} = 7.5 \times 10^{-5} h = 0.27 s$$

It means that the total volume of 150 µl is flushed once in 0.27 s. Within 1 s, the total volume was diluted three times.

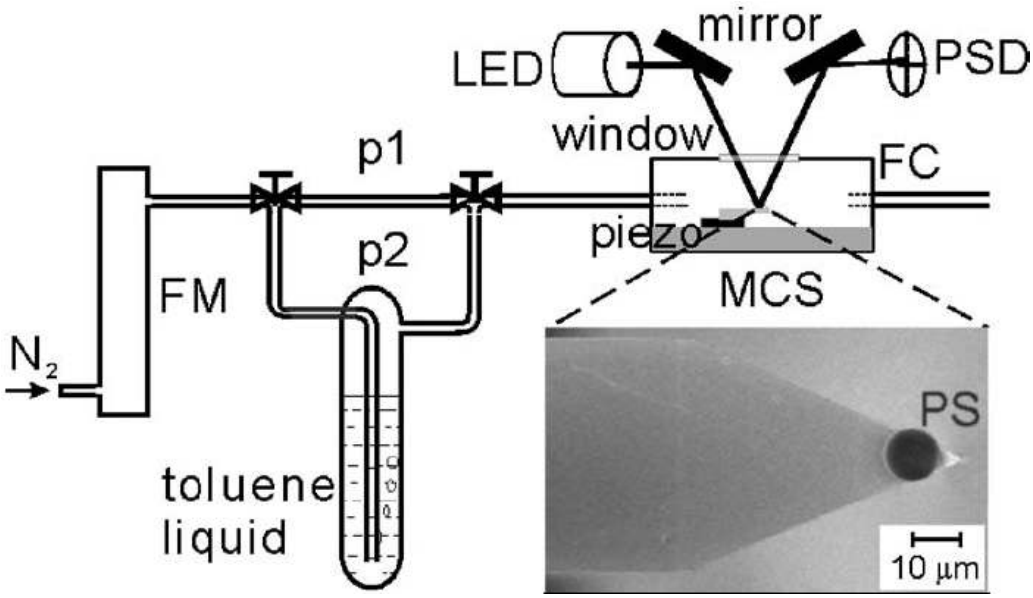

Fig. 61. Schematic drawing of the gas flow apparatus connected to a Scentris MCS setup. The scanning electron micrograph shows a PS sphere with diameter of 11µm sintered on the apex of a cantilever.

Samples and sample preparation

Dry powder, chemically cross-linked PS spheres (4-8 mol % divinylbenzene, density = 1.05 g/cm^3; Duke Scientific Corporation, Palo Alto, CA) with diameters ranging from 1 to 50 μm were used in this experiment.

To attach the polystyrene sphere to the end of the cantilever, two methods have been applied: Gluing and sintering.

In conventional experiments, gluing method is used to provide the chemical and mechanical stability of the sphere on the cantilever. But the glue drop has an additional mass and can not be removed after preparation. Therefore the sintering method was used in our experiments. First of all the PS spheres were poured on a glass slide (length of 76 mm, width of 26mm, thickness of 1 mm, Menzel, Braunschweig, Germangy) with a spatula and distributed evenly by knocking the backside of the slide slightly with a finger. The microspheres adhere on the glass even if the slide was put upside down, due to the capillary force. The chip with the cantilever was fixed on a micromanipulator arm (three dimensional oil-hydraulic manipulator MMO–203, Narishige Group, Japan), which allows approaching a single sphere with high precision. The cantilever was moved to the PS spheres and then one sphere was picked up from the glass slide. The capillary force between the sphere and the cantilever kept the sphere fixed during the withdrawal of the cantilever from the glass slide. The cantilever with attached PS sphere was then put into an oven (Furnace 47900, Thermolyne, Dubuque IA). It was heated up to 100±2 °C within 10 minutes and kept at 100±2 °C for 2 hours (general glass transition temperature of polystyrene: 100 °C).[100,101] Finally a sintering of the particle onto the cantilever could be established [Fig. 62].

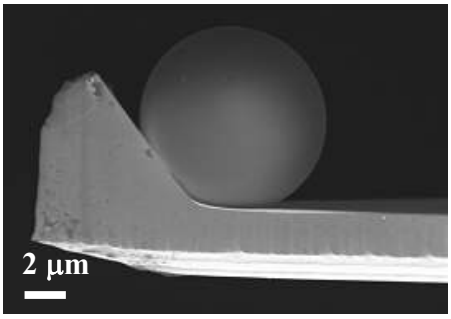

Fig. 62. The scanning electron micrograph shows a PS sphere with diameter of 11 μm sintered on the apex of a cantilever.

5.2 Atomic force microscopy

Optical microscope is usually used to obtain a magnified image of an object by focusing photons on the sample surface. It can easily generate 2D magnified images of an object's surface with a magnification as great as 1000×. Although it is a powerful tool for imaging, the images obtained are typically in the plane horizontal to the surface of the object. The vertical dimensions of an object's surface such as the height and depth of the surface features can not be achieved using normal optical microscope. The confocal microscope, which is a special optical microscope that creates a three-dimensional (3D) image, has a relatively low spatial resolution (several hundred nm, limited by the diffraction) compared with AFM. While other microscopes such as scanning electron microscopy (SEM), electromagnetic radiation is required to create a 3D image. Having an advantage of non-radiation, atomic force microscope (AFM) is a mechanical imaging technique using a sharpened probe that can measure the 3D topography as well as physical properties of a sample.

In our work, the 3D structure of PS nanoparticle arrays fabricated by solvent annealing was investigated using AFM.

A general atomic force microscope (AFM) consists of laser, a cantilever with tip, the scanner, position sensitive photodetector (PSD), the feedback loop and the computer [Fig. 63]. A laser beam is focused on the end of the cantilever and reflected to PSD. In this configuration, a piezoceramic scanner carries the cantilever over the sample. The scanner includes two cylinders, one assigned for lateral X-Y motion and the other for vertical z-motion. The cantilever deflection due to tip-sample interactions is monitored by the reflected laser spot on PSD. The feedback loop is assigned to maintain a constant deflection of the cantilever while scanning. The computer is used for setting the scanning parameters such as scan size, scan speed, feedback control response and visualizing images captured with the microscope. It controls the movement of the cantilever over the sample. Measurements of lateral dimensions can be performed with the resolution of angstrom and measurements of vertical dimensions can even achieve the resolution of subangstrom. The maximal measuring area, which is commonly covered by piezoceramic scanners, is about 100 μm×100 μm (Dimension 3100^{TM}, Veeco Instruments, Santa

Barbara, CA). Surface corrugations up to 5 µm in height can be profiled. Samples are placed on a movable X-Y stage, which is employed for positioning surface regions of interest under the cantilever.

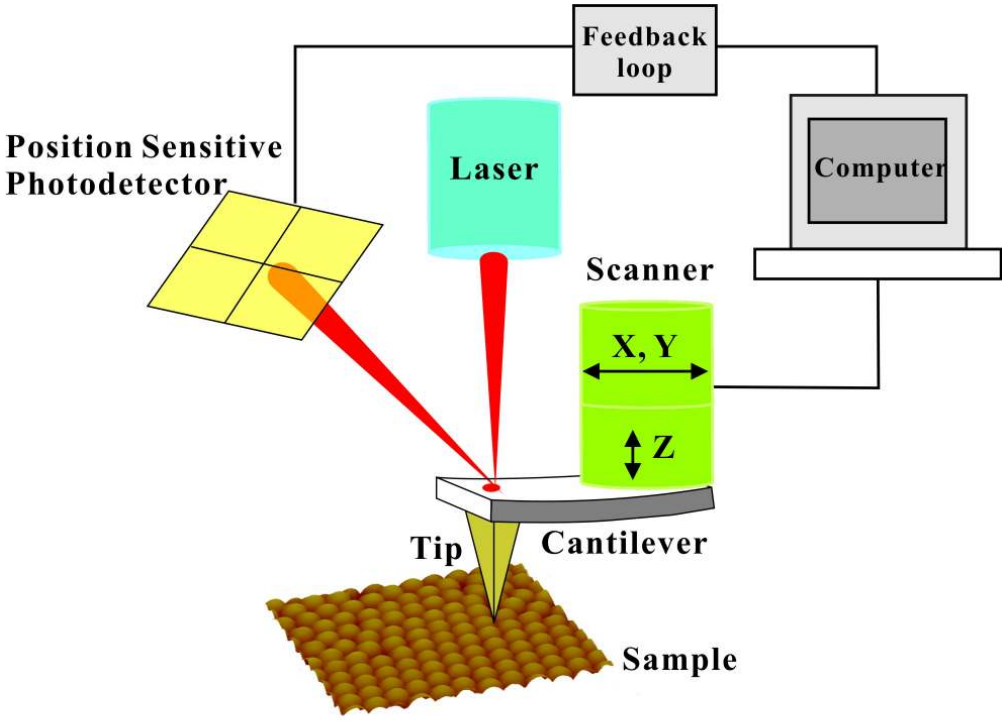

Fig. 63. Schematic drawing of the setup of atomic force microscopy (AFM).

The size of the sample can be in the range of several mm to several cm. The cantilever is operated in tapping mode. In this mode, the tip comes into contact with the sample once in every cycle of its oscillatory motion at the resonant frequency of the cantilever. During scanning in tapping mode, the tip comes only into intermittent contact with the sample surface. Therefore, soft samples can be measured while the tip-sample interaction force did not lead to the damage of this sample. As the probe lightly taps the surface, the amplitude of oscillation is reduced and the AFM uses this change in amplitude in order to track the surface topography. The digital feedback loop then adjusts the tip-sample separation to maintain a constant oscillation amplitude and force on the sample. The variations in the tip-sample separation are converted into a height image with bright (dark) contrast assigned to high (low) surface locations. In addition to its

oscillation amplitude, the cantilever motion can be characterized by its phase relative to a driving oscillator. The phase signal changes when the cantilever encounters regions of different composition. When the probe encounters the soft or viscous region, the adhesion between probe and the sample is more pronounced, which results in the retardance of the response signal relative to the drive signal. Phase shifts are indicated as bright and dark regions assigned to large (small) phase shifts in phase images, comparable to the way of height changes indicated in height images. Phase imaging has been found to be particularly useful to map the various components of composite materials. It can also be used to measure adhesion, surface hardness and elasticity.

Samples and sample preparation

Non-cross-linked PS particles in suspension (10 wt.% solids) with diameter of 1.98, 0.99 μm (Bangs Laboratories, Fishers, IN) and 0.5 μm (Duke Scientific Corporation, Palo Alto, CA) were used. The density of these PS particles is 1.05 g/cm^3.

The substrate was cleaned by RCA method to remove the organic contaminants and the PS particles were self-assembled on the substrate by spin coating.

RCA method

This standard method is used to clean the substrate surface. After the cleaning, a hydrophilic surface of the substrate is produced. It is conducted in the following steps:

1) Ultraclean water (Millipore, ρ=18.2 MW·cm), ammonium hydroxide and hydrogen peroxide (vol 5:1:1) are mixed in a quartz beaker. The quartz glass substrates are put inside the mixture and the beaker is heated up in a water bath. After the temperature has reached 80°C inside the solution, the system is kept 10 minutes at this temperature. After 10 minutes the system is cooled down.

2) When the temperature reaches about 50°C, the mixture is diluted by pouring ultrapure water into the beaker to the rim. Half of it is spilled. The solution is again half diluted in the same way. This step is repeated eight times. The substrate is kept all the time under water to avoid the contamination from the ambient environment.

3) The beaker is emptied completely and filled with ultrapure water to the rim. This step is repeated twice.
4) The beaker is again half filled with water and put in an ultrasonic bath for 5 minutes. Then it is rinsed with water again once. The substrates are always kept in the water before use.

Spin coating

A droplet of PS solution (PS spheres in de-ionized water used for nanostructuring experiment and PS dissolved in toluene used for UV absorption experiment) with volume of 2-5 μl is deposited onto the quartz glass substrate by the pipette. When the substrate starts to rotate, the solution spreads over the substrate surface. Due to the spinning, the solvent evaporates and finally only a residual PS film remains. The thickness and homogeneity of the residual film mainly depend on the spinning velocity ω and the concentration of the polymer solution c. The spinning time is adjusted until all the solvent evaporates.

5.3 Fluorescence Correlation Spectroscopy

Fluorescence correlation spectroscopy (FCS) is one of the techniques that facilitates high-resolution spatial and temporal analysis of extremely low concentrated molecules (in naonomolar range). The main principle is a correlation analysis of fluctuation of the fluorescence intensity. The fluorescence intensity is emitted by the fluorophore, which is a component of dye molecules present in the solution. When a particle diffuses in the focused spot in the solution, chemical or photophysical reactions or conformational changes may alter the emission characteristics of the fluorophore. It gives rise to additional fluctuations of the excited fluorescence intensity, which is detected by the detector. The fluctuation signal is higher with lower number of molecules. Therefore, to record the signals of these single molecules in the solution, it is necessary that the detection volume is correspondingly low. In fact, an extremely small measuring volume, smaller than femto (10^{-15}) liter, is produced. Compared with other fluorescence techniques, the parameter in FCS is not the emission intensity itself, but also spontaneous intensity of fluctuations caused by the minute deviations of the small system from thermal equilibrium. In general, all physical parameters that give rise to fluctuations in the fluorescence signal are accessible by FCS. For example, rather straightforward to determine local concentrations, diffusion coefficients of fluorescent labeled biomolecules can be determined. The diffusion coefficient is an important parameter to characterize the chemical property of the material.

In my work, the diffusion coefficient and distribution of dye molecules in the cross-linked PS spheres can be determined and observed using fluorescence imaging.

In confocal FCS (Carl Zeiss, Jena, Germany) a parallel laser beam (HeNe laser, wavelength of 543 nm) is reflected by a dichroic mirror and focused on a focal point through a microscope lens of high aperture [Fig. 64]. The volume of the focal point is less than 10^{-15} liter. This focal point forms the open measuring volume in the highly diluted solution in which the molecule diffuses in and out. A dye molecule present in the solution emits up to 20 million photons when it is in focus. The fluorescence light excited by the radiation of the laser beam is collected by the same objective and passes through the dichroic mirror. The pinhole blocks any fluorescence light not originating from the

focal region. Afterwards, the light is focused on a single photon detector. Although the route of the molecule through the focal point is random, the mean diffusion time and the size of the molecule can be calculated. It is based on a temporal correlation of the signal of many single molecules.

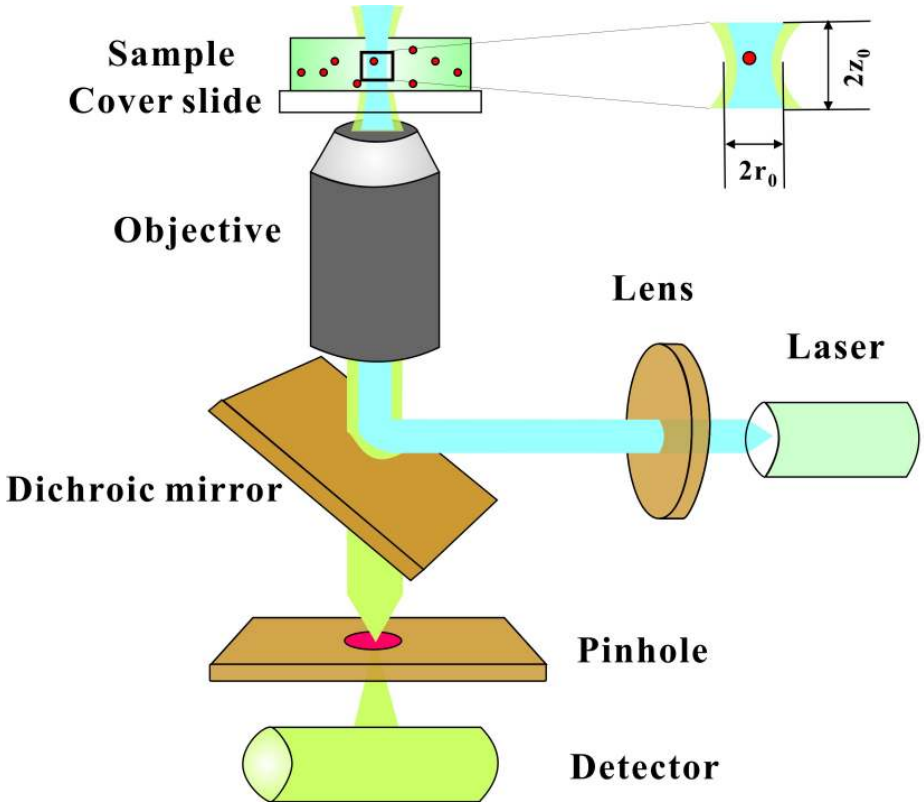

Fig. 64. Principle of fluorescence correlation spectroscopy. A laser beam (blue beam in the figure) passing through the lens is reflected by a dichroic mirror and focused on a focal point through objective. The focal point is the measuring volume which has a diameter of 0.34 µm (2 r_0) and height of 2 µm (2 z_0). The fluorescence light (green beam in the figure) excited by the radiation of the laser beam is passed through the objective, dichroic mirror and collected on the detector by a pinhole.

The measured fluorescence intensity is defined as a mean intensity plus fluctuations

$$I(t) = \langle I \rangle + \delta I(t) \tag{5.7}$$

where $\langle I \rangle$ is the mean intensity and $\delta I(t)$ is the fluctuations.

The auto-correlation function is given by Eq. (5.8)

$$G(\tau) = \langle I(t) I(t+\tau) \rangle \tag{5.8}$$

where τ is the correlation time.

Taking into account Eq. (5.7) and with $\langle \delta I(t) \rangle = 0$, the auto-correlation function can be described as Eq. (5.9)

$$G(\tau) = \langle \delta I(t) \delta I(t+\tau) \rangle + \langle I \rangle^2 \tag{5.9}$$

The normalized auto-correlation function is given by Eq. (5.10)

$$G(\tau) = 1 + \frac{\langle \delta I(t) \delta I(t+\tau) \rangle}{\langle I \rangle^2} \tag{5.10}$$

For an ellipsoid-shaped detection volume with Gaussian intensity distribution, the auto-correlation function is:

$$G(\tau) = 1 + \frac{1}{N} \frac{1}{\left(1 + \frac{\tau}{\tau_D}\right)} \frac{1}{\sqrt{1 + \frac{\tau}{S^2 \tau_D}}} \tag{5.11}$$

where N is the average number of molecules in the detection volume, τ_D is the characteristic diffusion time and $S = z_0 / r_0$.

The diffusion time required by a molecule to cross the measuring volume is determined from the inversion point of the auto-correlation curve [Fig. 65].

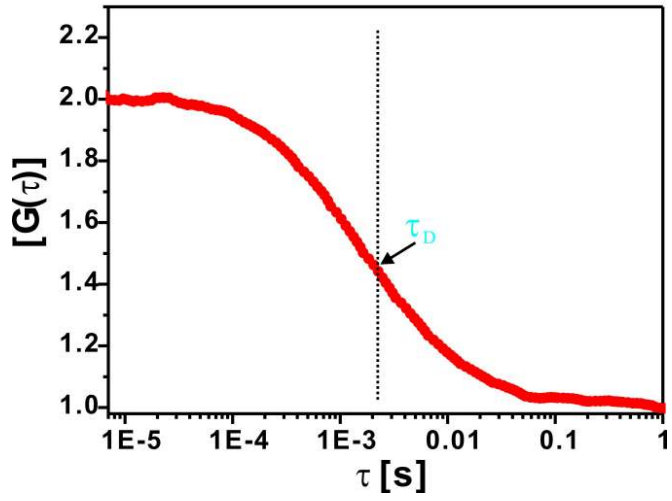

Fig. 65. The auto-correlation curve of a FCS measurement. The diffusion time τ_D is 1.8 ms.

The diffusion coefficient D can be calculated by Eq. (5.12)

$$D = \frac{r_0^{\,2}}{4\tau_D} \tag{5.12}$$

where r_0 is the radius of measuring volume and τ_D is the diffusing time of the molecules through the measuring volume.

Samples and sample preparation

The PS spheres were distributed on a glass slide (diameter of 25 mm, thickness of 0.13-0.16 mm, Menzel, Braunschweig, Germany). Then the sample was placed above the microscope [Fig. 66]. Toluene liquid was added to the sample as a solvent.

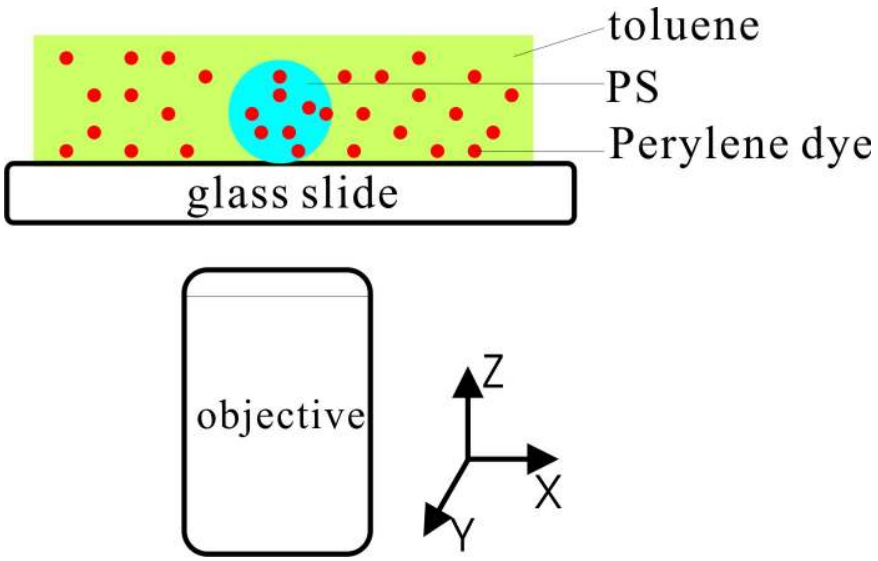

Fig. 66. Schematic drawing of PS sphere placed on glass slide above the objective of FCS. Z is the scan direction of the objective.

5.4 White light confocal microscopy

Confocal microscopy is an imaging technique used in the field of biology and material science to study morphology and surface roughness of the materials. Compared with conventional optical microscopy, confocal microscopy has a better contrast and better depth resolution in a few nm, which can construct three-dimensional images. Compared with AFM technique, imaging using confocal microscopy is fast (less than 10 minutes for one image while AFM takes more than 10 minutes) and non-contact of the specimen. The light source used in the setup is white light, so called the white light confocal microscopy.

In our work, the topography of MCS array of Veriscan was characterized using white light confocal microscopy to calibrate the optical readout of Veriscan.

The NanoFocus®µSurf® (µSurf®, NanoFocus AG, Oberhausen, Germany) measurement principle [Fig. 67], as a 3D video measurement system, is based on the white light confocal technique.

It consists of a compact confocal measurement head which is mounted on a stable stand and is driven in the vertical direction (z-axis) by a motor. The sample is placed on a movable x-y stage under the measurement head. The confocal unit is moved stepwise in the z-direction and scans various height levels of the surface. The surface to be measured is illuminated through the microscope by an external xenon light source. Only those light beams, which are focused on the sample surface, can be detected by the detector. All unfocused light beams, i.e. all that are not focused at the same height of sample surface, are blocked by a detector pinhole. In such a way, a single point can be measured. Surface areas which are at the same height level are mapped on the charge-coupled device (CCD) chip. These height level records can then be integrated to form a 2 or 3 dimensional image. The magnification of the objective we used is 20×. The corresponding maximum measurement area is 46 mm^2 and the vertical resolution is 5 nm.

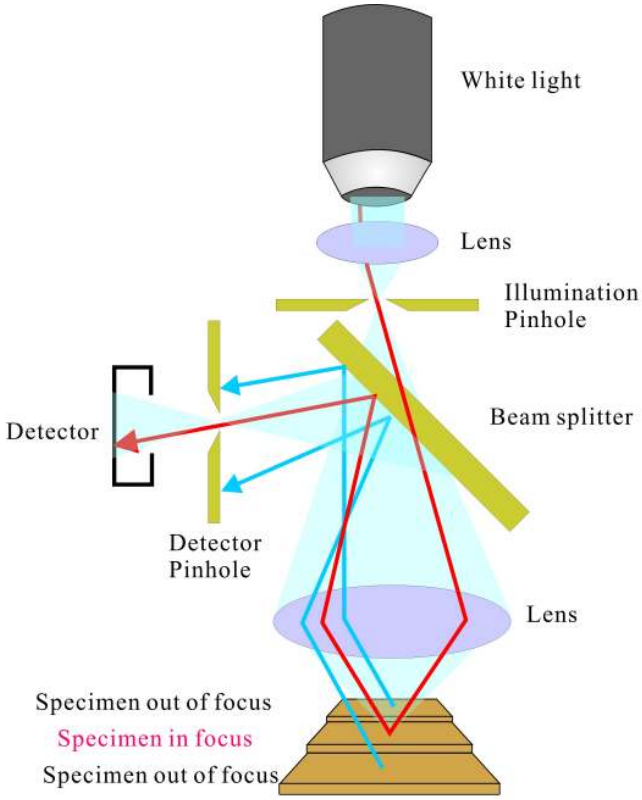

Fig. 67. Basic principle of white light confocal microscope. Light emitted from the white light source passes through the lens, illumination pinhole, the beam splitter and finally is focused on the speciment by the lens. The reflected light passes through the lens and hits on the beam splitter. After reflected from the beam splitter, the light is collected on the detector by a detector pinhole. Only the light reflected from the focus plane (red beam) reaches the detector, other lights from the speciment out of focus (blue beam) are blocked by the detector pinhole.

Samples and sample preparation

The MCS array of Veriscan was placed on a heating stage composed of aluminum. It is connected by a heater and a digital thermometer (GTH 175/MO, Greisinger electronic, Regenstauf, Germany). Then they were placed on the sample stage of Nanofocus. The heating rate can be adjusted manually and the temperature resolution is 0.1°C. The temperature is kept at a certain degree (error 1 °C) by manually switching on/off the heater.

Chapter 6

Summary, conclusions and outlook

Functionalization of individual MCS is achieved simply by flowing individual fluids or gases through separate wells. For the detection of molecules adsorbed on surfaces we found that the absolute bending of MCS must be considered in experiments involving fluid flow. This issue is solved by calculation of the absolute bending relative to a fixed mirror. The absolute bending of MCS can be measured with accuracy of 0.1 nm. A reversible, linear dependence of MCS bending with fluid flow rate was observed. The difference in MCS bending induced by hydrodynamic flow was found to be negligible. MCS were functionalized in four different wells and upon considering the delay time of the fluid entering each well, differential deflections can be calculated. The signal recorded from the reference mirror was proved to be useful to monitor the concentration changes owing to mixing effects during the flow. The MCS deflection of 200 nm, 600 nm and 15 nm was detected for thiolated DNA probe immobilization, MCH adsorption and DNA hybridization, respectively. Thus, single base mismatch detection based on MCS is feasible. The MCS deflection increases with increasing MCH concentration, which shows a good performance of the MCS array. In particular, the functionalization of MCS situated in each well is simplified and cross contamination is avoided. Therefore standard protocols for surface functionalization can be applied and no further equipment is required. The latter compatibility to standard protocols is highly required in the field of biotechnology. The recognition independently but simultaneously in separate wells offers the potential advantages to measure multiple analytes in a single step. The prize for this advantage is that the chip size becomes larger and therefore more expensive. However, mass production of Si chips is possible and price < 10 cents per chip would be realistic in the future.

A mass sensitivity of pg can be achieved by end loading of MCS. Thus, the swelling behavior of individual micron-sized PS spheres in toluene vapor was studied by a sensor system based on MCS. For 4-8% chemically cross-linked PS a relative mass

increase of 180% in saturated toluene vapor was measured. Those PS particles were found to be completely swollen after 10 s of exposure to toluene vapor. Optical microscopy with higher magnification and fast recording rate was taken to measure the diameter change of PS spheres during swelling. From optical images a relative volume increase of 200% in saturated toluene vapor was calculated. From the data of mass or volume change, the diffusion coefficient of toluene in PS is modeled (in cooperation with Torsten et al. from university of Siegen). The mass of the swollen PS sphere decreases with increasing exposure to UV light. It shows that UV light irradiation can be used for controlling the solvent uptake and release on PS spheres by a factor of 2. In addition, the swelling response is significantly slowed down (6 times slower) upon the first exposure to toluene vapor than the second one. This is attributed to the formation of a cross-linked shell at the surface of the PS spheres. We found that chemically and additional UV cross-linked PS spheres keep the shape even after numerous swelling cycles in saturated toluene vapor. Local UV exposure of selected areas could allow fine-tuning of the shape of polymer components. Such elements might be used in biotechnology as microreactors.[102] UV cross-linked PS particle was found to be fluorescent and cracks were observed after exposure in toluene liquid. FCS measurements have revealed that the diffusion coefficient of dye molecules decreases with increasing cross-linking density. One of the next steps would be to immobilize polymers on MCS and study mass uptake and release in solvent liquids depending on the solvent quality. The detachment of physically adsorbed PS sphere from MCS surface allows to study the adhesion between polymer and the substrate.[103] In this case, the oscillation amplitude of MCS with attached PS sphere was increased by sequentially increasing the drive amplitude. At a certain oscillation amplitude, the PS sphere was detached from the MCS surface [Fig. 68]. Using PS spheres with different sizes and different functionalized MCS surface, the adhesion of polymer and substrate can be studied by analyzing the detachment situations.

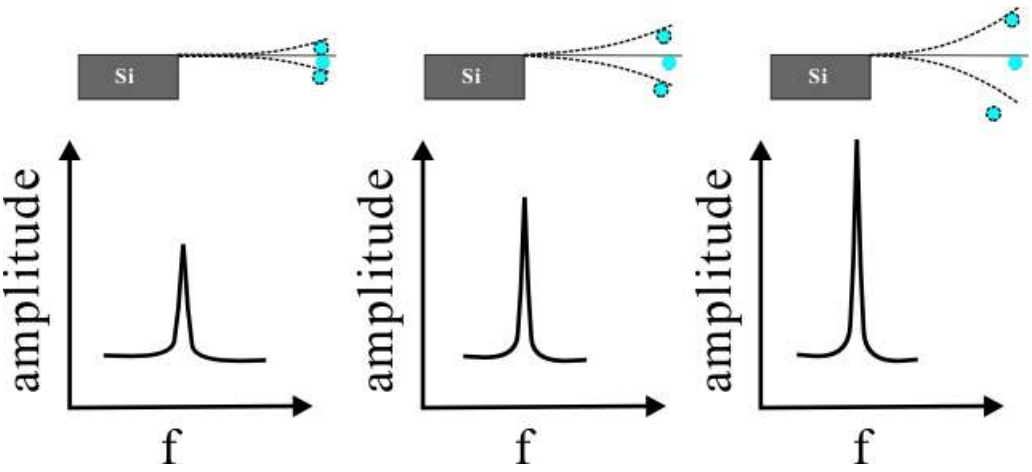

Fig. 68. Schematic illustration of detachment of PS sphere from the MCS surface.

Donut PS structures were fabricated by exposing hexagonally close-packed PS spheres to toluene liquid. The stabilizer poly (styrene sulfonate) (PSS) or poly (acrylic acid) (PAA) was suggested to play a role in structure formation. Additional longer UV irradiation leads to the complete cross-linking of PS spheres. The experiments showed that the donut structure is stable after liquid solvent rinsing. Thus, a free standing film removed from the substrate is expected to be possible. Based on this expectation, a film of donut structure with variant sizes can be fabricated simply by varying the diameter of PS spheres. Furthermore, similar than before washing with toluene, the adsorption of different stabilizers might allow to control the structure of donut meshes. The potential application is nanocontainers such as confined reaction vessels in biotechnology.

List of publications

R. Zhang, K. Graf, and R. Berger, Swelling of cross-linked polystyrene spheres in toluene vapor, *Applied Physics Letters* **89**, 223114 (2006)

R. Zhang, S. Cherian, R. Cain, S. Lorenzoni, A. Best, E. Macis, R. Raiteri, R. Berger, A multiwell micromechanical cantilever array reader for biotechnology, *accepted for publication in Review of Scientific Instruments*, July 2007

Abbreviations

2D	two-dimensional
3D	three-dimensional
AFM	atomic force microscopy
CCD	charge coupled device
CLSM	confocal laser scanning microscopy
DI	deionised
DIC	differential interference contrast
DNA	deoxyribonucleic acid
ds	double-stranded
DTT	dithiothreitol
FC	fluid cell
FCS	fluorescence correlation spectroscopy
FEM	Finite element method
FEP	fluorinated ethylene propylene
FM	flow meter
LED	light emitting diode
MCH	6-mercapto-1-hexanol
MCS	micromechanical cantilever sensor
OTS	octadecyltrichlorosilane
PAA	poly (acrylic acid)
PDI	Perylene dye
PEEK	polyethylether ketone
ppm	parts per million
PS	polystyrene
PSD	position sensitive photodetector
PSS	poly (styrene sulfonate)
QCM	quartz crystal microbalances
SAW	surface acoustic wave
SEM	scanning electron microscopy

SPR	Surface Plasma Resonance
ss	single-stranded
T_g	glass transition temperature
TCEP	tris 2-carboxyethyl phosphine
Teflon	polytetrafluoroethylene
TNT	trinitrotoluene
UV	ultra violet
VCSELs	vertical cavity surface emitting lasers

References

(1) Fritz, J.; Baller, M. K.; Lang, H. P.; Rothuizen, H.; Vettiger, P.; Meyer, E.; Guntherodt, H. J.; Gerber, C.; Gimzewski, J. K. *Science* **2000**, *288*, 316.

(2) Lin, C. T.; Wang, S. M. *Frontiers in Bioscience* **2005**, *10*, 99.

(3) Collings, A. F.; Caruso, F. *Reports on Progress in Physics* **1997**, *60*, 1397.

(4) Pinnaduwage, L. A.; Ji, H. F.; Thundat, T. *Ieee Sensors Journal* **2005**, *5*, 774.

(5) Rodriguez-Mozaz, S.; Marco, M. P.; de Alda, M. J. L.; Barcelo, D. *Pure and Applied Chemistry* **2004**, *76*, 723.

(6) Farre, M.; Barcelo, D. *Trac-Trends in Analytical Chemistry* **2003**, *22*, 299.

(7) Pividori, M. I.; Lermo, A.; Hernandez, S.; Barbe, J.; Alegret, S.; Campoy, S. *Afinidad* **2006**, *62*, 13.

(8) Dewar, R. J.; Ash, D. C.; German, M. J.; Joyce, M. J. *Journal of Food Engineering* **2006**, *75*, 461.

(9) Sapsford, K. E.; Ngundi, M. M.; Moore, M. H.; Lassman, M. E.; Shriver-Lake, L. C.; Taitt, C. R.; Ligler, F. S. *Sensors and Actuators B-Chemical* **2006**, *113*, 599.

(10) Patel, P. D. *Trac-Trends in Analytical Chemistry* **2002**, *21*, 96.

(11) Meadows, D. *Advanced Drug Delivery Reviews* **1996**, *21*, 179.

(12) Soper, S. A.; Brown, K.; Ellington, A.; Frazier, B.; Garcia-Manero, G.; Gau, V.; Gutman, S. I.; Hayes, D. F.; Korte, B.; Landers, J. L.; Larson, D.; Ligler, F.; Majumdar, A.; Mascini, M.; Nolte, D.; Rosenzweig, Z.; Wang, J.; Wilson, D. *Biosensors & Bioelectronics* **2006**, *21*, 1932.

(13) Yu, D. H.; Blankert, B.; Vire, J. C.; Kauffmann, J. M. *Analytical Letters* **2005**, *38*, 1687.

(14) Mikkilineni, S. P. V. N.; Tree, D. A.; High, M. S. *Journal of Chemical and Engineering Data* **1995**, *40*, 750.

(15) Crooks, R. M.; Yang, H. C.; McEllistrem, L. J.; Thomas, R. C.; Ricco, A. J. *Faraday Discussions* **1997**, 285.

(16) Gimzewski, J. K.; Gerber, C.; Meyer, E.; Schlittler, R. R. *Chemical Physics Letters* **1994**, *217*, 589.

(17) Raiteri, R.; Nelles, G.; Butt, H. J.; Knoll, W.; Skladal, P. *Sensors and Actuators B-Chemical* **1999**, *61*, 213.

(18) McKendry, R.; Zhang, J. Y.; Arntz, Y.; Strunz, T.; Hegner, M.; Lang, H. P.; Baller, M. K.; Certa, U.; Meyer, E.; Guntherodt, H. J.; Gerber, C. *Proceedings of the National Academy of Sciences of the United States of America* **2002**, *99*, 9783.

(19) Cherian, S.; Gupta, R. K.; Mullin, B. C.; Thundat, T. *Biosensors & Bioelectronics* **2003**, *19*, 411.

(20) Johansson, A.; Blagoi, G.; Boisen, A. *Applied Physics Letters* **2006**, *89*, 173505.

(21) Sepaniak, M.; Datskos, P.; Lavrik, N.; Tipple, C. *Analytical Chemistry* **2002**, *74*, 568a.

(22) Lavrik, N. V.; Sepaniak, M. J.; Datskos, P. G. *Review of Scientific Instruments* **2004**, *75*, 2229.

(23) Lim, S. H.; Raorane, D.; Satyanarayana, S.; Majumdar, A. *Sensors and Actuators B-Chemical* **2006**, *119*, 466.

(24) Huber, F.; Hegner, M.; Gerber, C.; Guntherodt, H. J.; Lang, H. P. *Biosensors & Bioelectronics* **2006**, *21*, 1599.

(25) Betts, T. A.; Tipple, C. A.; Sepaniak, M. J.; Datskos, P. G. *Analytica Chimica Acta* **2000**, *422*, 89.

(26) Berger, R.; Lang, H. P.; Gerber, C.; Gimzewski, J. K.; Fabian, J. H.; Scandella, L.; Meyer, E.; Guntherodt, H. J. *Chemical Physics Letters* **1998**, *294*, 363.

(27) Thundat, T.; Chen, G. Y.; Warmack, R. J.; Allison, D. P.; Wachter, E. A. *Analytical Chemistry* **1995**, *67*, 519.

(28) Thundat, T.; Maya, L. *Surface Science* **1999**, *430*, L546.

(29) Hansen, K. M.; Thundat, T. *Methods* **2005**, *37*, 57.

(30) Raiteri, R.; Grattarola, M.; Butt, H. J.; Skladal, P. *Sensors and Actuators B-Chemical* **2001**, *79*, 115.

(31) Ziegler, C. *Analytical and Bioanalytical Chemistry* **2004**, *379*, 946.

(32) Pinnaduwage, L. A.; Wig, A.; Hedden, D. L.; Gehl, A.; Yi, D.; Thundat, T.; Lareau, R. T. *Journal of Applied Physics* **2004**, *95*, 5871.

(33) Butt, H. J. *Journal of Colloid and Interface Science* **1996**, *180*, 251.

(34) Tamayo, J.; Humphris, A. D. L.; Malloy, A. M.; Miles, M. J. *Ultramicroscopy* **2001**, *86*, 167.

(35) Lang, H. P.; Berger, R.; Andreoli, C.; Brugger, J.; Despont, M.; Vettiger, P.; Gerber, C.; Gimzewski, J. K.; Ramseyer, J. P.; Meyer, E.; Guntherodt, H. J. *Applied Physics Letters* **1998**, *72*, 383.

(36) Boisen, A.; Thaysen, J.; Jensenius, H.; Hansen, O. *Ultramicroscopy* **2000**, *82*, 11.

(37) Kim, B. H.; Prins, F. E.; Kern, D. P.; Raible, S.; Weimar, U. *Sensors and Actuators B-Chemical* **2001**, *78*, 12.

(38) Lang, H. P.; Baller, M. K.; Berger, R.; Gerber, C.; Gimzewski, J. K.; Battiston, F. M.; Fornaro, P.; Ramseyer, J. P.; Meyer, E.; Guntherodt, H. J. *Analytica Chimica Acta* **1999**, *393*, 59.

(39) Knoll, A.; Bachtold, P.; Bonan, J.; Cherubini, G.; Despont, M.; Drechsler, U.; Durig, U.; Gotsmann, B.; Haberle, W.; Hagleitner, C.; Jubin, D.; Lantz, M. A.; Pantazi, A.; Pozidis, H.; Rothuizen, H.; Sebastian, A.; Stutz, R.; Vettiger, P.; Wiesmann, D.; Eleftheriou, E. S. *Microelectronic Engineering* **2006**, *83*, 1692.

(40) http://www.chem.ucla.edu/dept/Faculty/gimzewski/id11.htm.

(41) Beam, E. A.; Kao, Y. C.; Yang, J. Y. *Applied Physics Letters* **1991**, *58*, 152.

(42) Bietsch, A.; Zhang, J. Y.; Hegner, M.; Lang, H. P.; Gerber, C. *Nanotechnology* **2004**, *15*, 873.

(43) http://mrsec.uchicago.edu/research/nuggets/coffee/.

(44) Bain, C. D.; Evall, J.; Whitesides, G. M. *Journal of the American Chemical Society* **1989**, *111*, 7155.

(45) Bumbu, G. G.; Kircher, G.; Wolkenhauer, M.; Berger, R.; Gutmann, J. S. *Macromolecular Chemistry and Physics* **2004**, *205*, 1713.

(46) Raiteri, R.; Grattarola, M.; Berger, R. *Materialstoday* **2002**, *5*, 22.

(47) Burg, T. P.; Godin, M.; Knudsen, S. M.; Shen, W.; Carlson, G.; Foster, J. S.; Babcock, K.; Manalis, S. R. *Nature* **2007**, *446*, 1066.

(48) Juliano, R. L.; Mccullough, H. N. *Journal of Pharmacology and Experimental Therapeutics* **1980**, *214*, 381.

(49) Yatvin, M. B.; Muhlensiepen, H.; Porschen, W.; Weinstein, J. N.; Feinendegen, L. E. *Cancer Research* **1981**, *41*, 1602.

(50) Langer, R. *Nature* **1998**, *392*, 5.

(51) Discher, D. E.; Eisenberg, A. *Science* **2002**, *297*, 967.

(52) Duncan, R. *Nature Reviews Drug Discovery* **2003**, *2*, 347.

(53) Sauer, M.; Meier, W. *Chemical Communications* **2001**, 55.

(54) Chen, G. H.; Hoffman, A. S. *Nature* **1995**, *373*, 49.

(55) Bonaccurso, E.; Butt, H. J.; Graf, K. *European Polymer Journal* **2004**, *40*, 975.

(56) Svorcik, V.; Rybka, V.; Hnatowicz, V.; Novotna, M.; Vognar, M. *Journal of Applied Polymer Science* **1997**, *64*, 2529.

(57) Nardin, C.; Meier, W. G. *Chimia* **2001**, *55*, 142.

(58) Caruso, F.; Shi, X. Y.; Caruso, R. A.; Susha, A. *Advanced Materials* **2001**, *13*, 740.

(59) Kabanov, A. V.; Alakhov, V. Y. *Critical Reviews in Therapeutic Drug Carrier Systems* **2002**, *19*, 1.

(60) Ibarz, G.; Dahne, L.; Donath, E.; Mohwald, H. *Advanced Materials* **2001**, *13*, 1324.

(61) Beaulieu, L. Y.; Godin, M.; Laroche, O.; Tabard-Cossa, V.; Grutter, P. *Applied Physics Letters* **2006**, *88*.

(62) Berger, R.; Gerber, C.; Lang, H. P.; Gimzewski, J. K. *Microelectronic Engineering* **1997**, *35*, 373.

(63) Yue, M.; Lin, H.; Dedrick, D. E.; Satyanarayana, S.; Majumdar, A.; Bedekar, A. S.; Jenkins, J. W.; Sundaram, S. *Journal of Microelectromechanical Systems* **2004**, *13*, 290.

(64) Helm, M.; Servant, J. J.; Saurenbach, F.; Berger, R. *Applied Physics Letters* **2005**, *87*.

(65) Zhao, J.; Berger, R.; Gutmann, J. S. *Applied Physics Letters* **2006**, *89*.

(66) Salvadori, M. C.; Brown, I. G.; Vaz, A. R.; Melo, L. L.; Cattani, M. *Physical Review B* **2003**, *67*.

(67) Brandrup, J. a. I., E. H. *Polymer Handbook*, 3rd ed.; John Wiley: New York, 1989.

(68) Levy, R.; Maaloum, M. *Nanotechnology* **2002**, *13*, 33.

(69) Zhang, X. R.; Xu, X. F. *Applied Physics Letters* **2004**, *85*, 2423.

(70) Mertens, J.; Calleja, M.; Ramos, D.; Taryn, A.; Tamayo, J. *Journal of Applied Physics* **2007**, *101*, 034904.

(71) Zhou, F.; Shu, W. M.; Welland, M. E.; Huck, W. T. S. *Journal of the American Chemical Society* **2006**, *128*, 5326.

(72) Yaws, C. L. *Chemical properties Handbook*; McGraw-Hill, 1999.

(73) Andersen, M.; Painter, L. R.; Nir, S. *Biopolymers* **1974**, *13*, 1261.

(74) Barer, R.; Tkaczyk, S. *Nature* **1954**, *173*, 821.

(75) Tsargorodskaya, A.; Nabok, A. V.; Ray, A. K. *Nanotechnology* **2004**, *15*, 703.

(76) Chambers, D. A. *DNA*; Robert A. Welch Foundation: Houston, 1993.

(77) Wittmann, C. *Immobilisation of DNA on Chips I*; Springer: Berlin, 2005.

(78) Wittmann, C.; Bier, F. F. *Immobilisation of DNA on Chips II*; Springer: Berlin, 2005.

(79) Berger, R.; Delamarche, E.; Lang, H. P.; Gerber, C.; Gimzewski, J. K.; Meyer, E.; Guntherodt, H. J. *Science* **1997**, *276*, 2021.

(80) Raiteri, R.; Butt, H. J.; Grattarola, M. *Electrochimica Acta* **2000**, *46*, 157.

(81) Fritz, J.; Baller, M. K.; Lang, H. P.; Strunz, T.; Meyer, E.; Guntherodt, H. J.; Delamarche, E.; Gerber, C.; Gimzewski, J. K. *Langmuir* **2000**, *16*, 9694.

(82) Thundat, T.; Warmack, R. J.; Chen, G. Y.; Allison, D. P. *Applied Physics Letters* **1994**, *64*, 2894.

(83) Alvarez, M.; Carrascosa, L. G.; Moreno, M.; Calle, A.; Zaballos, A.; Lechuga, L. M.; Martinez-A, C.; Tamayo, J. *Langmuir* **2004**, *20*, 9663.

(84) Lechuga, L. M.; Tamayo, J.; Alvarez, M.; Carrascosa, L. G.; Yufera, A.; Doldan, R.; Peralias, E.; Rueda, A.; Plaza, J. A.; Zinoviev, K.; Dominguez, C.; Zaballos, A.; Moreno, M.; Martinez, C.; Wenn, D.; Harris, N.; Bringer, C.; Bardinal, V.; Camps, T.; Vergnenegre, C.; Fontaine, C.; Diaz, V.; Bernad, A. *Sensors and Actuators B-Chemical* **2006**, *118*, 2.

(85) Mertens, J.; Alvarez, M.; Tamayo, J. *Applied Physics Letters* **2005**, *87*.

(86) Wu, G. H.; Ji, H. F.; Hansen, K.; Thundat, T.; Datar, R.; Cote, R.; Hagan, M. F.; Chakraborty, A. K.; Majumdar, A. *Proceedings of the National Academy of Sciences of the United States of America* **2001**, *98*, 1560.

(87) Tamai, T.; Hashida, I.; Ichinose, N.; Kawanishi, S.; Inoue, H.; Mizuno, K. *Polymer* **1996**, *37*, 5525.

(88) Maenosono, S.; Okubo, T.; Yamaguchi, Y. *Journal of Nanoparticle Research* **2003**, *5*, 5.

(89) Schubert, D. W.; Dunkel, T. *Materials Research Innovations* **2003**, *7*, 314.

(90) Dimitrov, A. S.; Nagayama, K. *Langmuir* **1996**, *12*, 1303.

(91) Li, T.; Zhou, C. L.; Jiang, M. *Polymer Bulletin* **1991**, *25*, 211.

(92) Stoney, G. G. *Proceedings of the Royal Society of London Series a-Containing Papers of a Mathematical and Physical Character* **1909**, *82*, 172.

(93) Vig, J. R. *Journal of Vacuum Science & Technology a-Vacuum Surfaces and Films* **1985**, *3*, 1027.

(94) Godin, M.; Williams, P. J.; Tabard-Cossa, V.; Laroche, O.; Beaulieu, L. Y.; Lennox, R. B.; Grutter, P. *Langmuir* **2004**, *20*, 7090.

(95) http://probe.olympus-global.com/en/en/specsiliconE.html.

(96) Antoine, C. *Comptes rendus de l'Academie des sciences* **1888**, *107*, 681.

(97) Rodgers, R. C.; Hill, G. E. *British Journal of Anaesthesia* **1978**, *50*, 415.

(98) http://webbook.nist.gov/cgi/cbook.cgi?ID=C108883&Units=SI&Mask=4.

(99) Besley, L. M.; Bottomle.Ga. *Journal of Chemical Thermodynamics* **1974**, *6*, 577.

(100) Wunderlich, B. *Thermal Analysis*; Academic Press: NY, 1990.

(101) Rieger, J. *Journal of Thermal Analysis* **1996**, *46*, 965.

(102) Luchnikov, V.; Stamm, M.; Akhmadaliev, C.; Bischoff, L.; Schmidt, B. *Journal of Micromechanics and Microengineering* **2006**, *16*, 1602.

(103) Llic, B.; Krylov, S.; Kondratovich, M.; Craighead, H. G. *Nano Letters* **2007**, *7*, 2171.